
**Membrane-mimetic systems for the structural
characterization of membrane proteins by cryo-electron
microscopy**

Dissertation
zur Erlangung
des Doktorgrades der Naturwissenschaften (Dr. rer. nat.)
der
Naturwissenschaftlichen Fakultät I – Biowissenschaften –
der Martin-Luther-Universität
Halle-Wittenberg,

vorgelegt
von Herrn **Kevin Janson**
geboren am 26.05.1994 in Landstuhl

eingereicht am: 14.02.2023

Gutachter*innen

1 Jun.-Prof. Dr. Panagiotis L. Kastiris

2 PD. Dr. Annette Meister

3 Prof. Dr. Arne Gericke

Datum der Verteidigung: 22.05.2023

*To my family and in loving
memory of my grandmother*

Table of contents

Table of contents	I
List of abbreviations	V
Summary	VII
Zusammenfassung	IX
1. Introduction	1
1.1 Biological membranes	1
1.1.1 Membrane lipids	2
1.1.2 Membrane proteins	5
1.2 Membrane-mimetic systems	6
1.2.1 Detergent-mediated membrane mimetic systems	7
1.2.1.1 Detergent micelles	7
1.2.1.2 Vesicles	8
1.2.1.3 Bilayered micelles	9
1.2.1.4 Short amphiphilic polymers (amphipols)	10
1.2.1.5 Protein-bounded nanodiscs	10
1.2.2 Detergent-free polymer-bound nanodiscs	11
1.3 Biophysical analysis methods of vesicles and nanodiscs	14
1.3.1 Dynamic light scattering	14
1.3.2 Transmission electron microscopy	15
1.4 Cryo-electron microscopy (cryo-EM)	19
1.4.1 High-resolution cryo-EM of membrane proteins	19
1.4.2 Single particle analysis workflow	20
1.5 Model proteins	22
1.5.1 Formate channel A – FocA	22
1.5.1 1L-myoinositol-1-phosphate synthase – MIPS	23

2	Aim of this thesis	24
3	Materials and methods	25
3.1	Materials	25
3.1.1	Chemicals.....	25
3.1.2	Buffers	27
3.1.3	Cellular sources.....	27
3.1.4	Lipids, polymers, and proteins	27
3.1.5	Instruments, consumables, and software	28
3.2	Methods	31
3.2.1	Molecular biology methods	31
3.2.1.1	Cell culture.....	31
3.2.1.2	Cell lysis and membrane preparation.....	31
3.2.2	Biochemical methods	32
3.2.2.1	Preparation of polymer stock solutions	32
3.2.2.2	Protein precipitation.....	32
3.2.2.3	Bichonic acid assay	33
3.2.2.4	Gel electrophoresis – SDS-PAGE.....	33
3.2.2.5	Size exclusion chromatography	33
3.2.2.6	In-solution digestion in the presence of RapiGest.....	34
3.2.2.7	Liquid chromatography-coupled mass spectrometry	34
3.2.2.8	Data analysis of mass spectrometry data	35
3.2.3	Biophysical methods	36
3.2.3.1	Preparation of vesicles	36
3.2.3.2	Preparation of protein-free polymer-bound nanodiscs	36
3.2.3.3	Preparation of protein-containing polymer-bound nanodiscs.....	36
3.2.3.4	Dynamic light scattering	37
3.2.3.5	Proteome wide blastp and membrane protein identification	37
3.2.3.6	Negative stain EM sample preparation	38
3.2.3.7	Image processing of negative-stain data and size calculations	38
3.2.3.8	Cryo-EM sample preparation	38

3.2.3.9	Size analysis of native nanodiscs in cryo-EM	39
3.2.3.10	Image analysis and modelling of cryo-EM Data.....	39
4	Results and Discussion	42
4.1	Detergent-mediated membrane mimetic system: The membrane protein FocA in detergent micelles.....	42
4.1.1	Structural analysis of FocA by single-particle cryo-EM.....	42
4.2	Detergent-free membrane mimetic systems: Protein-free and protein-containing polymer-bound nanodiscs	49
4.2.1	Protein-free polymer-bound nanodiscs	50
4.2.1.1	Multi-component lipid vesicles.....	50
4.2.1.2	Solubilization and characterization of multi-component lipid vesicles.....	55
4.2.1.2.1	Solubilization of vesicles mimicking pig heart inner mitochondrial membranes by diisobutylene/maleic acid	55
4.2.1.2.2	Solubilization of pig heart IMLM _{CL} vesicles by polymers of different charge	59
4.2.1.2.3	Solubilization of IMLM _{yeast} vesicles by DIBMA and SMA(2:1).....	66
4.2.1.2.4	Solubilization of thermophilic fungus lipid mixture by Sulfo-DIBMA	68
4.2.2	Protein-containing polymer-bound nanodiscs.....	70
4.2.2.1	Isolation and solubilization of cellular membranes from <i>Chaetomium thermophilum</i> . 70	
4.2.2.2	Biochemical analysis of protein-containing polymer-bound nanodiscs.....	71
4.2.2.3	Cryo-EM and mass spectrometry of protein-containing polymer-bound nanodisc	75
4.2.2.4	Structural analysis of protein-containing polymer-bound nanodiscs.....	79
5	Conclusion and outlook.....	82
6	References.....	85
7	Appendix.....	i
8	Acknowledgment	xi
9	Curriculum vitae.....	xiii
10	List of Publications.....	xiv

11	Oral presentations	xv
12	Poster presentations	xvi
13	Affidavit.....	xvii
14	Eidesstattliche Erklärung.....	xviii

List of abbreviations

2D	Two dimensional
3D	Three dimensional
λ	Wavelength
a_0	Headgroup area
Å	Angström
A_{280}	Absorption at 280 nm
Amphipols	Short amphiphilic polymers
BCA	Bichonic acid
Bicelles	Bilayered micelles
C_s	Spherical aberration
CCD	Charge-coupled detector
<i>C. thermophilum</i>	<i>Chaetomium thermophilum</i>
CL	Cardiolipin
CMC	Critical micellar concentration
ddH ₂ O	Double distilled water
DED	Direct electron detectors
DTT	Dithiothreitol
d_z	Size distribution
EDTA	Ethylenediaminetetraacetic acid
ERG	Ergosterol
TFLM	Thermophilic fungus lipid mixture
Cryo-EM	Cryo-electron microscopy
CTF	Contrast transfer function
DIBMA	Diisobutylene-maleic acid
DDM	n-Dodecyl- β -D-maltoside
DLS	Dynamic light scattering
<i>E. coli</i>	<i>Escherichia coli</i>
f	spatial frequency
FEG	Field emission gun
FocA	Formate channel A
FNT	Formate nitrate transporter
FSC	Fourier shell correlation
Glu6-P	Glucose-6-phosphate
Glyco-DIBMA	Glycosylated diisobutylene/maleic acid
GPI	glycosylphosphatidylinositol
Heart-CL	Bovine heart cardiolipin, sodium salt
Heart-PC	Bovine heart L- α -Phosphatidylcholin
Heart-PE	Bovine heart L- α -Phosphatidylethanolamin
Heart-PG	Soy L- α -phosphatidylglycerol sodium salt
His209	Histidine residue at the amino acid chain position 209
hMW	High molecular weight
IDR	Intrinsic disordered region
IMLM _{CL}	Inner mitochondrial lipid mixture
IMLM _{neut.}	Inner mitochondrial lipid mixture with a neutral charge
IMLM _{PG}	Inner mitochondrial lipid mixture with PG
IMLM	Inner mitochondrial lipid mixture without CL
IMLM _{yeast}	Inner mitochondrial lipid mixture of <i>Saccharomyces cerevisiae</i>
kDA	kilo daltons
L_α	Liquid crystalline state
L_β	Gel phase
l_c	Length of acyl chains
Liver-PI	Bovine liver L- α -Phosphatidylinositol, sodium salt
IMW	Low molecular weight
LUV	Large unilamellar vesicle

<i>M. thermophila</i>	<i>Myceliophthora thermophila</i>
microED	Micro electron diffraction
MIPS	Myo-inositol-1-phosphate synthase
MLV	Multi-lamellar vesicle
mMW	Medium molecular weight
m_P/m_L	Polymer to lipid mass ratio
MS	Mass spectrometry
MSP	Membrane scaffold protein
$MW_{app.}$	Apparent molecular weight
MW	Molecular weight
NS-EM	Negative stain electron microscopy
P	Packing parameter
P-NMR	Phosphate nuclear magnetic resonance spectroscopy
PA	1-Palmitoyl-2-linoleoyl- <i>sn</i> -glycero-3-phosphate
PC	1-Palmitoyl-2-linoleoyl- <i>sn</i> -glycero-3-phosphocholine
PDI	Polydispersity index
PE	1-Palmitoyl-2-oleoyl- <i>sn</i> -glycero-3-phosphoethanolamine
PI	1-Palmitoyl-2-oleoyl- <i>sn</i> -glycero-3-phosphoinositol
PS	1-Palmi- toyl-2-oleoyl- <i>sn</i> -glycero-3-phospho-L-serine
QA1-SMA	Styrene-maleimide quaternary ammonium
QA2-SMA	Styrene-maleimide quaternary ammonium
rpm	rounds per minute
SDS	Sodium dodecyl sulfate
<i>S. cerevisiae</i>	<i>Saccharomyces cerevisiae</i>
SDS-PAGE	Sodium dodecyl sulfate poly acrylamide gel electrophoresis
SEC	Size exclusion chromatography
SEM	Scanning electron microscopy
SMA(2:1)	Styrene/maleic acid
SMA-SH	Styrene/maleic acid sulfohydriols
Sulfo-DIBMA	Sulfobetaine diisobutylene/maleic acid
TEM	Transmission electron microscopy
T_m	Melting temperature
v	Acyl chain volume
V_e	Elution volume
zSMA	Styrene/maleic acid phosphocholine
z	Defocus

One and three letter code of amino acids

A	Ala	Alanine
R	Arg	Arginine
N	Asn	Asparagine
D	Asp	Aspartic acid
C	Cys	Cysteine
E	Glu	Glutamic acid
Q	Gln	Glutamine
G	Gly	Glycine
H	His	Histidine
I	Ile	Isoleucine
L	Leu	Leucine
K	Lys	Lysine
M	Met	Methionine
F	Phe	Phenylalanine
P	Pro	Proline
S	Ser	Serine
T	Thr	Threonine
W	Try	Tryptophan
Y	Tyr	Tyrosine
V	Val	Valine

Summary

Membrane proteins possess numerous vital roles in cell, pose as the gateway to their intracellular milieu, and therefore, are of high pharmacological interest. Structural studies have proven to be of tremendous aid to the field of pharmaceutical research, as high-resolution protein structures can help identify new targets and serve as a starting point for the development and screening of pharmacological substances. Since the resolution revolution, cryo-electron microscopy (cryo-EM) has drastically aided in advancing the elucidation of membrane proteins, which is reflected in a considerable increase of deposited structures of membrane proteins in the protein data base utilizing cryo-EM. However, it was not only the advancements in the field of cryo-EM, but also the improvements made on membrane mimetic systems: Among the membrane mimetic systems, amphiphilic copolymers such as styrene/maleic acid (SMA) and diisobutylene/maleic acid (DIBMA) received great attention over the last decade, as they solubilize membrane proteins along with their surrounding lipids providing an environment close to the native membrane. The so formed particles are called nanodiscs and consist of a membrane patch, in which the protein is embedded, that is surrounded by a belt of amphiphilic copolymer.

Herein, the structure of the formate channel A (FocA), stabilized in n-dodecyl- β -D-maltoside (DDM) micelles, was resolved to 3.1 Å with the aid of cryo-EM. This allowed for the unambiguous modelling of the full-length pentameric assembly. The modelled structure enabled the characterization of its pore, revealing a compartmentalized polarity distribution across which is mirrored against a two-fold axis of the important histidine residue 209 (H209). Additionally, detergent densities were identified inside the pentameric assembly that are hypothesized to be a substitute to phospholipids in a cellular context. The revealed detergent densities highlight the drawbacks of detergents as a membrane mimetic system, namely being potentially detrimental interactions of detergents with the hydrophobic moieties of membrane proteins. Although the FocA structure provided insights into its function as a formate transporter, usage of detergent as membrane mimetic systems, in other cases, can lead to the loss of molecular structure and thus function.

In a pharmacological context, an incorrectly folded protein could give a wrong estimation for the initial steps of the drug development process. Therefore, a membrane mimetic system that provides a closer-to-native environment would be of

big advantage in the research field of membrane proteins. To this extent, recently developed amphiphilic copolymers were tested for their ability to solubilize artificial multi-component vesicles that mimic the lipid composition of inner mitochondrial membranes. Subsequently, the formed nanodiscs were characterized for their morphology and size by dynamic light scattering and negative stain electron microscopy (NS-EM). This solubilization revealed a high polydispersity which was reflected in the high heterogeneity that was observed in NS-EM. All polymers were able to solubilize the membranes, with sulfobetaine diisobutylene/maleic acid (Sulfo-DIBMA) showing the best overall performance.

As Sulfo-DIBMA revealed the best performance, it was tested to solubilize artificial vesicles that mimic the lipid composition of a thermophilic fungus. After it was shown that Sulfo-DIBMA successfully solubilizes the artificial thermophilic membranes, native membranes from the thermophilic fungus *Chaetomium thermophilum* were used for membrane protein extraction. The isolated membrane proteins were then purified by size exclusion chromatography and subsequently used for the 3D reconstruction and identification by cryo-EM and mass spectrometry. Among the identified proteins, a soluble protein, which is known to transiently associate with membranes, myo-inositol-1-phosphate (MIPS), was reconstructed at 4.73 Å. The reconstruction allowed for fitting the molecular model of MIPS and revealed previously un-observed densities. Additionally, an unidentified nanodisc-embedded protein was reconstructed at ~18 Å. Mass spectrometry, cryo-EM, and the homology-based identification algorithm gave rise to a promising candidate (UniProt-ID: G0SI00), an uncharacterized protein in *Chaetomium thermophilum*. Based on homologous annotated proteins this protein could represent a potassium channel. Subsequent fitting of multiple downloaded voltage gated potassium channel structures revealed a reasonable overall fit to the map. However, due to the low resolution it was not possible to unambiguously identify the endogenous and native, nanodisc-embedded protein complex.

As a concluding remark, this thesis reveals the efficient solubilization of artificial multi-component as well as natural membranes with functionalized amphiphilic copolymers and their effective usage in structural biology. The so-resolved structures could hold further insights into native structures of membrane protein complexes that could further be used for the structure-based drug development.

Zusammenfassung

Membranproteine haben zahlreiche lebenswichtige Funktionen in der Zelle und stellen das Tor zum intrazellulären und interorganellen Milieu dar. Deshalb sind sie von großem pharmakologischem Interesse. Strukturbioologische Studien haben sich für die pharmazeutische Forschung als äußerst hilfreich erwiesen, da hochaufgelöste Proteinstrukturen die Grundlage des rationalen Wirkstoffentwurfs darstellen und daher den Ausgangspunkt für die Entwicklung und das Screening pharmakologischer Substanzen darstellen. Seit der „*resolution revolution*“ hat die Kryoelektronenmikroskopie (Kryo-EM) die Aufklärung von Membranproteinen drastisch vorangebracht was deutlich an der Zunahme der hinterlegten kryo-EM Strukturen von Membranproteinen in der Proteindatenbank zu erkennen ist. Es waren jedoch nicht nur die Fortschritte auf dem Gebiet der Kryo-EM, sondern auch die Verbesserungen, die an membranmimetischen Systemen vorgenommen wurden. Unter diesen Systemen haben amphiphile Copolymere wie Styrol/Maleinsäure (SMA) und diisobutylen/Maleinsäure (DIBMA) in den letzten zehn Jahren große Aufmerksamkeit erregt, da sie Membranproteine zusammen mit den sie umgebenden Lipiden solubilisieren und so eine Umgebung schaffen, die der natürlichen Membran nahekommt. Die resultierenden Partikel werden als *Nanodiscs* beschrieben und bestehen aus einer Membranscheibe, in der das Protein integriert ist, und die umgeben ist von einem Gürtel aus Polymer.

In dieser Arbeit wurde die Struktur des Formiat-Kanals A (FocA), der in n-Dodecyl- β -D-maltosid (DDM)-Mizellen stabilisiert ist, mit Hilfe von Kryo-EM mit einer Auflösung von 3.1 Å aufgeklärt. Dies ermöglichte die eindeutige Modellierung der nativen Quartärstruktur eines Homopentamers. Diese Struktur ermöglichte die Charakterisierung der Membranpore und zeigte eine kompartimentierte Polaritätsverteilung, die sich an einer zweifachen Achse der wichtigen Histidinseitenkette 209 (H209) spiegelt. Darüber hinaus wurden Detergenzdichten innerhalb der pentameren Struktur identifiziert, von denen angenommen wird, dass sie im zellulären Kontext durch Phospholipide ersetzt werden. Die aufgelösten Detergenzien-Dichten verdeutlichen die Nachteile von Detergenzien als membranmimetisches System, nämlich potentiell schädliche Wechselwirkung der Detergenzien mit den hydrophoben Anteilen von Membranproteinen. Obwohl die FocA-Struktur Einblicke in seine Funktion als Formiat-Transporter lieferte, kann die

Verwendung von Detergenzien als membranmimetische Systeme in anderen Fällen zum Verlust der nativen Struktur und damit der Funktion führen.

In einem pharmakologischen Kontext stellt ein artifizielle Proteinstruktur eine potentiell fehlerhafte Grundvoraussetzung für die ersten Schritte der Arzneimittelentwicklung dar. Daher ist ein membranmimetisches System, das die native Umgebung erhält, für die Erforschung von Membranproteinen von großem Vorteil. Zu diesem Zweck wurden kürzlich entwickelte amphiphile Copolymere im Rahmen dieser Arbeit auf ihre Fähigkeit getestet, künstliche Mehrkomponenten-Vesikel zu solubilisieren, die die Lipidzusammensetzung innerer mitochondrialer Membranen nachahmen. Anschließend wurden die gebildeten *Nanodiscs* mittels dynamischer Lichtstreuung und Elektronenmikroskopie an negativ kontrastierten Proben (NS-EM) hinsichtlich ihrer Morphologie und Größe charakterisiert. Die Solubilisierung ergab eine hohe Polydispersität, die sich in der hohen strukturellen Heterogenität widerspiegelte. Alle Polymere waren in der Lage, die Membranen zu solubilisieren, wobei Sulfobetain-Diisobutylen/Maleinsäure (Sulfo-DIBMA) die beste Gesamtleistung zeigte.

Da Sulfo-DIBMA die beste Solubilisierungsrate zeigte, wurde es verwendet um künstliche Vesikel zu solubilisieren, welche die Lipidzusammensetzung eines thermophilen Pilzes nachahmen. Nachdem gezeigt wurde, dass Sulfo-DIBMA die künstlichen thermophilen Membranen erfolgreich löst, wurden native Membranen aus dem thermophilen Pilz *Chaetomium thermophilum* für die Membranproteinextraktion verwendet. Die isolierten Membranproteine wurden dann durch Größenausschlusschromatographie angereichert und anschließend mittels Kryo-EM und Massenspektrometrie analysiert. Unter den detektierten Proteinen wurde Myo-Inositol-1-Phosphat (MIPS), ein lösliches Protein von dem bekannt ist, dass es vorübergehend mit Membranen assoziiert, identifiziert und die Proteinstruktur mit einer Auflösung von 4.73 Å rekonstruiert. Diese Rekonstruktion ermöglichte die Optimierung des molekularen Modells von MIPS und offenbarte zuvor strukturell unbekannte Proteinstrukturen. Darüber hinaus wurde ein nicht identifiziertes, in eine *Nanodisc* eingebettetes Protein mit einer Auflösung von ~18 Å rekonstruiert. Massenspektrometrie, Kryo-EM und der auf Homologie basierende Identifizierungsalgorithmus ergaben einen vielversprechenden Kandidaten (UniProt-ID: G0SI00), ein bisher uncharakterisiertes Protein aus *Chaetomium thermophilum*. Auf der Grundlage annotierter homologer Proteine könnte dieses Protein einen Kaliumkanal darstellen. Die anschließende Anpassung mehrerer publizierter

spannungsgesteuerter Kaliumkanalstrukturen ergab eine rationale Gesamtanpassung an die Kryo-EM Dichtekarte. Aufgrund der geringen Auflösung war es jedoch nicht möglich, den endogenen und nativen, in die *Nanodisc* eingebetteten Proteinkomplex zweifelsfrei zu identifizieren.

Zusammenfassend lässt sich feststellen, dass diese Studie die wirksame Solubilisierung künstlicher Mehrkomponenten- und natürlicher Membranen mittels funktionalisierten amphiphilen Copolymeren sowie deren erfolgreiche Anwendung in der Strukturbiologie demonstriert. Die so aufgelösten Membranproteinkomplexstrukturen können dann Erkenntnisse über deren native Strukturen liefern. Dieses Wissen könnte dann, z.B., in der strukturbasierten Entwicklung von Wirkstoffen einen erheblichen Beitrag leisten.

1. Introduction

1.1 Biological membranes

All living cells are separated by biological membranes, shielding their interior from the environment and aid as a mechanical support in the cellular assembly and its organelles.¹ Biological membranes are intricate complex assemblies that consist of different lipids, proteins, and sugars (Figure 1).^{2,3} This complex assembly participates in a multitude of cellular processes, such as controlled differentiation of new cells, build-up of concentration gradients, serving as a diffusion barrier, cell-cell recognition, regulation of metabolite transport, and even cell death.⁴⁻⁷

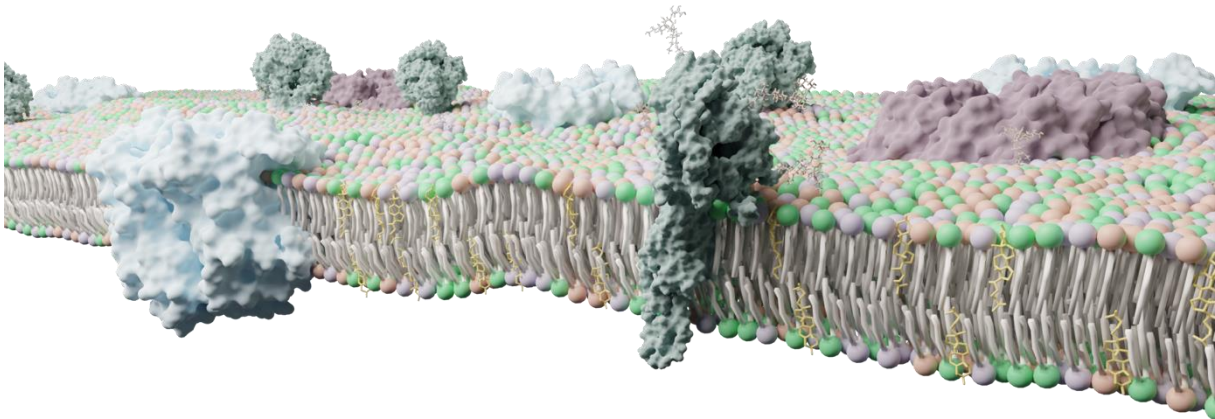


Figure 1: Schematic depiction of the cross section of a eukaryotic biological membrane. Depicted is a biological membrane that consists of a lipid bilayer in which various proteins are embedded or associated to. The lipid bilayers are made of various different lipids, indicated by a colored headgroup, and sterols in their stick representation.

Each component of any biological membrane, contributes to its physico-chemical properties in a non-linear and non-additive manner, allowing for highly-specialized individualizations of the various membranes in a cell.⁸⁻¹⁴ Additionally, these properties are carefully regulated and maintained for by various proteins, adjusting the cellular metabolism if needed.^{2,3,15} The current biological model, the fluid mosaic model,¹ describes the biological membrane as a crowded, intricate, two-dimensional, fluid bilayer that interacts, via membrane proteins, with the cytoskeleton as well as the extracellular matrix and is composed of two asymmetric layers of lipids with different domains in which membrane proteins are embedded or associated to.^{1,3} Under physiological conditions, biological membranes are in the liquid-crystalline state.² In this state lipids and membrane proteins are relatively free to laterally diffuse, given the restraints of the membrane. Furthermore, lipids are able to translocate from the inner

to the outer leaflet and vice-versa; however, this process is thermodynamically rather unfavorable and requires the action of special transport proteins, so-called flippases, and floppases.¹⁶

1.1.1 Membrane lipids

Lipids that are involved in the formation of a biological membrane, are amphiphilic molecules that consist of a hydrophilic head and a hydrophobic tail. Their physico-chemical properties depend on the length and the degree of saturation of the aliphatic hydrocarbon chain, which makes up the hydrophobic tail of the lipids, and the neutral, zwitterionic or negatively charged hydrophilic headgroup.^{17,18}

The biological membranes of many bacteria, animals, and fungi consist mainly of three different classes of lipids: phospholipids, glycolipids, and sterols.¹⁹ In detail, the group of phospholipids can be separated into the class of glycerophospholipids and the phosphosphingolipids. The glycerophospholipids consist of a glycerol backbone which is connected by ester linkage to a phosphate group and two fatty-acid chains (Figure 2), whereas the class of phosphosphingolipids consists of a sphingoid backbone which is connected by an amide-bond to a fatty-acid chain and a phosphate group.²⁰ In general, glycerophospholipids typically make up the bulk of the lipids in biological membranes.²¹ A common example of a glycerophospholipid is phosphatidylcholine which has an additional choline group attached to its phosphate group.²²

Glycolipids are a group of lipids that carry, instead of a phosphate headgroup, a mono- or oligosaccharide headgroup. They mainly reside in the outer leaflet of the biological membranes and are involved in multiple processes such as membrane stabilization, cell–cell interactions,²³ or immune response.²⁴

Sterols, such as cholesterol and ergosterol, are a subgroup of steroids and are derived from gonane, but instead of a hydrogen have a hydroxyl group at the C₃ position. Naturally, sterols occur in most of the eukaryotes and in some bacteria. Functionally, sterols are involved in cell signalling,²⁵ substrate presentation,²⁶ in the modulation of the membrane properties,²⁷ and serve as a chemical precursor.^{28,29}

These lipids can further be split into three groups namely bulk-, annular, and structural lipids.²¹ Bulk lipids are lipids that make up the majority of the lipids in a membrane

without interacting specifically with proteins.³⁰ Annular lipids are lipids that surround the proteins that are embedded or anchored in the membrane and interact, generally, non-specifically with them.³¹ Structural lipids are lipids that are specifically bound or buried inside the proteins and are relevant for their proper structure and function.³²

In an aqueous solution these amphiphilic molecules, mainly driven by the hydrophobic effect, form aggregates minimizing unfavorable interactions between the hydrophobic acyl chains and the aqueous solvent.³³ The form of the aggregates that are assembled is dictated by the shape of the lipids that are involved and is known as lipid polymorphism. The shape of the lipids is defined by their geometry which is described by the so-called packing parameter (P) and can be calculated as:³⁴

$$P = \frac{v}{a_0 \cdot l_c}$$

where v is the volume occupied by the acyl chains, a_0 is the cross-sectional area of the headgroup, and l_c is the critical length (Figure 2A).

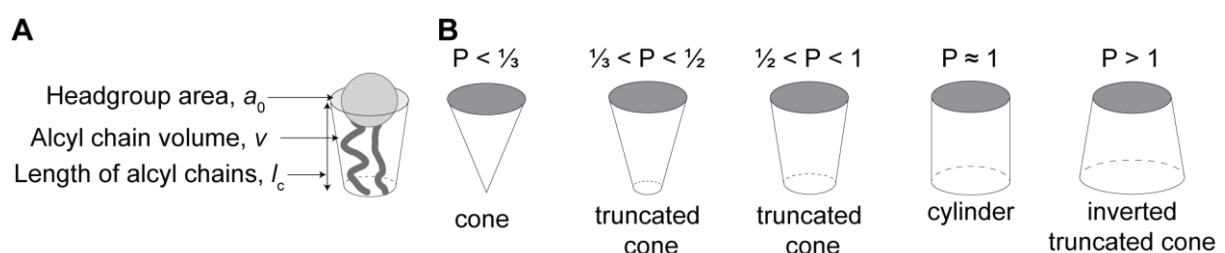


Figure 2 Graphical depiction of a lipid and its packing parameter. (A) Schematic representation of a lipid with the headgroup area (a_0), acyl chain volume (v), and length of the acyl chains l_c indicated. **(B)** Geometrical shapes that are used to describe the lipid shape according to their packing parameter.

Their shape can further be influenced by pH, temperature, salt concentrations, and hydration.³⁵ Glycerophospholipids such as phosphatidylcholine (PC), phosphatidylinositol (PI), and phosphatidylglycerol (PG) resemble a more or less cylindrical shape and a $P \approx 1$. Whereas glycerophospholipids, such as cardiolipin (CL) or phosphatidylethanolamine (PE), have a small headgroup area and a large tail volume resembling the structure of an inverted truncated cone with a $P > 1$.³⁶ On the contrary, lyso lipids or detergents resemble the structure of a cone with $P < 1/3$. Depending on their shape, lipids can form various aggregates, such as micelles, bilayers, or hexagonal phases.³⁵

The cellular membranes are complex mixtures of proteins, sugars, and lipids which are organized in the form of lipid bilayers. Furthermore, each of the various lipid bilayers in a cell has a different composition, resulting in various membranes with different

physico-chemical properties regarding their fluidity, charge, asymmetry, and curvature.²

The fluidity of a lipid bilayer refers to its viscosity and determines the degree to which proteins and lipids diffuse laterally in the lipid bilayer. The fluidity of a membrane is influenced by all of its components and their interactions.^{37,38} On a lipid basis, the fluidity is affected by the length and degree of saturation of the acyl chains, lipid composition, and temperature.^{39,40} Lipids with shorter acyl chains occupy a smaller area, resulting in fewer hydrocarbon atoms that participate in stabilizing van der Waals interactions with the adjacent hydrophobic acyl chains, thus increasing the fluidity of the lipid bilayer.⁴¹ Fully saturated carbon chains affect the fluidity by increasing the van der Waals interactions with the adjacent hydrophobic acyl chains, thus making the membrane more rigid.⁴⁰ On the other hand, unsaturated carbon-carbon bonds in the acyl chains of the lipids create a “kink”, making the lipid itself more rigid but increasing in the same turn, the fluidity of the membrane as it impairs the packing-ability of the surrounding lipids, causing a decrease in stabilizing van der Waals interactions.^{42,43} An increase or decrease in the temperature allows for an increase or decrease in the fluidity of the lipid bilayer, respectively. Furthermore, changing the temperature above or below a lipid mixture specific temperature, the so-called melting temperature (T_m), membranes undergo a phase transition from the liquid crystalline phase (L_α) to the gel phase (L_β).^{44,45} In the liquid crystalline phase, lipids are “loosely” packed inside the lipid bilayer. In this phase many of the lipids are in gauche conformation, allowing for a greater area per molecule and greater rotational freedom of the lipids. On the contrary, in the gel phase, lipids are in the all-*trans* conformation, therefore, are packed tightly, resulting in a more rigid membrane that has a lower area per molecule, greatly impairing rotational and lateral movement.³⁸ In terms of lipid composition, certain lipids, such as sterols, can have drastic effects on the membrane properties. Sterols can alter the lipid phase behavior, or the fluidity, rigidity, and permeability of the lipid bilayer.^{27,41,43}

Biological membranes in a cell are not uniform but asymmetric, meaning that the composition of the inner leaflet differs from the composition of the outer leaflet, even showing specific domains inside the lipid bilayer (e.g., annular lipids and structural lipids around a membrane protein).^{3,21,30-32,38} This results in two completely different leaflets with different physico-chemical properties.^{3,46} The asymmetry of the lipid bilayer is maintained by various proteins, and a loss of asymmetry often results in cell

death.⁴⁶ The asymmetry and the thereby caused non-uniform distribution of lipids induces global and local curvatures creating this way various forms of membranes inside a cell. Prominent examples are the cristae of mitochondria, the endoplasmic reticulum, or the Golgi apparatus which have dramatically distinct structure and curvatures to serve their corresponding functions. Additionally, the curvature of the membrane can also be altered through different proteins, creating local curvature shifts or even form completely different structures.⁴⁷⁻⁵⁰

1.1.2 Membrane proteins

Membrane proteins make up ~25% of the cellular proteome and are crucial for all living cells, as being involved in processes such as cell-cell signaling,⁵¹ signal transduction,⁵² transport of ions and metabolites,^{53,54} enzymatic reactions,⁵⁵ and cell motility.⁵⁶ Therefore, without membrane proteins, biological membranes would, solely, be a diffusional barrier separating the cell from its environment.⁵⁷ Additionally, ~60% of the current drug targets are membrane proteins.⁵⁸ The new discovery and development of drugs to treat any disease is a tedious process, often involving high-throughput screening of chemical compound libraries that could inhibit or modulate the target's function in order to find potential lead compounds.⁵⁹ During the last two decades, structure-based approaches paired with computational methods to identify potential new drug targets have become a tremendous help in identifying new potential drug targets.^{60,61} Thus, a precise structural elucidation of membrane proteins would immensely aid the drug discovery against membrane protein target.⁶²

Membrane proteins can be separated into two categories: peripheral membrane proteins and integral membrane proteins, with further subgroups among them.⁶³ The first category consists of proteins close to the membrane that interact mostly with the lipid headgroups or are either anchored in the cellular membrane by, e.g., an amphipathic helix or an hydrophobic loop. The latter category are membrane proteins that are fully- or partly embedded into the membrane, burying their hydrophilic sidechains into the hydrophobic region of the membrane. Specific protein–lipid interactions are essential for membrane proteins, governing their organization in the membrane, as well as their structure, and function.^{31,64} In terms of their structure, the majority of transmembrane proteins are alpha-helical proteins– 27% of all human proteins are estimated to be alpha-helical membrane proteins.⁵⁶ Beta-barrels, so-far,

have only been found in the outer membranes of bacteria, chloroplasts and mitochondria.⁶⁵

Despite their biological and pharmacological importance, membrane proteins are still underrepresented in functional and structural studies.⁶⁶ Currently, there are ~1550 unique membrane-protein structures and ~61000 total protein structure entries in the PDB (from a total redundant set of ~10000 membrane proteins out of 195000 in total), making up to ~2.5% of membrane proteins out of all structures deposited in the PDB, highlighting how much membrane protein structure research is lagging behind. (<https://blanco.biomol.uci.edu/mpstruc/> accessed on 28.01.2023). This is mainly due to the inherent challenge membrane proteins bring with them. The study of membrane proteins requires their extraction from their complex hydrophobic membrane environment. Due to their amphiphilic nature, they need to be stabilized outside of the membrane in the aqueous solution.⁶⁷ The exposure to the aqueous solution, without a suitable system to harbor membrane proteins, would be detrimental to them, as their hydrophobic domains would be exposed to the aqueous environment, leading, in most cases, to loss of their structure and function.⁶⁷ To prevent the exposure of the hydrophobic domains of membrane proteins to the aqueous solvent, they are harbored, after their extraction from the membranes, in membrane-mimetic systems.⁶⁸ These systems imitate the hydrophobic environment that the lipid bilayer was providing, thus stabilizing them in the aqueous solution.⁶⁹ However, as mentioned above, biological membranes are complex, heterogeneous structures providing a unique environment for membrane proteins, enabling crucial protein–protein, protein–lipid, and in general, macromolecular interactions.^{32,70} Thus, stripping away the lipid bilayer and harboring membrane proteins in any membrane-mimetic system is a delicate matter, as it potentially removes interaction partners that may be decisive for the structure and function of membrane proteins and are not sufficiently compensated for by the membrane-mimetic system.^{47,70} Thus, it is crucial to provide a membrane-mimetic system that offers similar physicochemical properties of the membrane to the protein of interest.

1.2 Membrane-mimetic systems

Some amphiphilic molecules can provide a suitable hydrophobic environment for membrane proteins, while shielding them from the aqueous solution, after the

extraction from the membrane. Over the last decades, a multitude of different membrane-mimetic systems have been developed, to be compatible with the methodological approach, while preserving the structural properties of the membrane proteins.⁶⁸

1.2.1 Detergent-mediated membrane mimetic systems

In the following chapter the most prominent detergent-mediated membrane mimetic systems are presented. However, a more comprehensive list of all membrane-mimetic systems are available in the literature.⁶⁸

1.2.1.1 Detergent micelles

Detergents are a class of amphiphilic, surface-active agents, so-called surfactants, that structurally consist of a hydrophilic headgroup and a hydrophobic tail group. Generally, most detergents exhibit a conical shape, where the flexible hydrophobic tail chain occupies a smaller cross-sectional area than the hydrophilic group (Figure 2B).⁷¹ Driven by the hydrophobic effect, and given their geometrical structure, detergents self-assemble into detergent micelles in an aqueous solution.³³ There the hydrophilic headgroups are exposed to the aqueous environment, thus shielding the hydrophobic carbon chains that are buried inside the micelles. The self-assembly process of detergents is termed micellization and happens above a detergent-specific concentration threshold, the so-called critical micellization concentration (CMC).⁷² In detail, addition of detergents to the solution linearly increases the detergent monomer concentration. Upon reaching the CMC, the number of monomers stays constant and the formation of micelles begins. Further addition of detergent only increases the number of micelles in the solution. The CMC is one of the key properties of a detergent and should be accounted for when working with detergents.⁷³

When mixed with a lipid bilayer, detergents can disrupt the lipid bilayer and extract the membrane proteins within, thereby stabilizing them in small protein/detergent complexes in the aqueous solution (Figure 3).^{72,73} This allows for the biochemical and biophysical investigation of membrane proteins that would not have been possible in their native environment.^{71,74} The stability of those detergent/protein complexes is

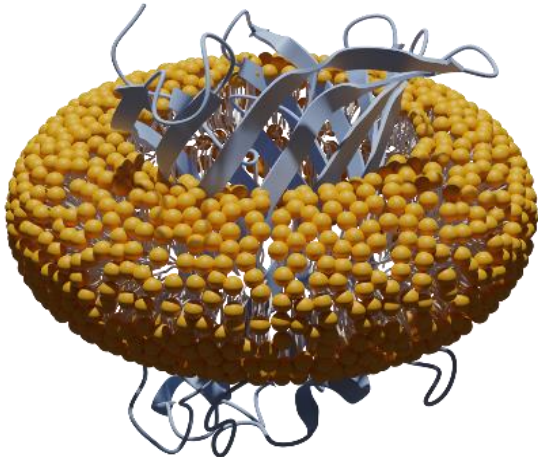


Figure 3: Illustration of a conventional head-and-tail detergent-stabilized membrane protein. The membrane protein is harbored inside the detergent micelle (yellow molecules). PDB:1QD6

formation behavior happen in an unselective manner, thus sometimes disrupting the higher-order structure of membrane-protein complexes.⁷⁶

However, the majority of structural studies on membrane proteins are still done with the aid of detergents.⁶⁶ More specifically in the last decade, maltosides have proven to be the detergents of choice for structural investigations. Within this group, the most prominent one was DDM, which is considered to be the gold standard due to its low CMC and its mild solubilization properties. Nevertheless, more options of different detergents are being investigated in the last decade such as fluorinated surfactants and branched detergents broadening the toolbox of solubilization agents that researchers can choose from.^{77,78}

1.2.1.2 Vesicles

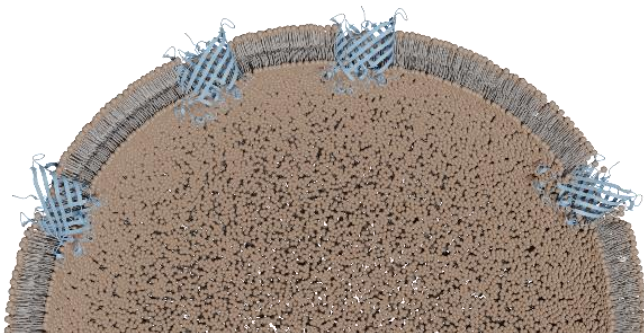


Figure 4 Illustration of a vesicle-embedded outer membrane protein. Cross section of membrane proteins embedded into a LUV. PDB:1QD6

Vesicles or liposomes are spherical lipid bilayer systems that enclose an inner aqueous environment. These systems are often consisting out of synthetic phospholipids, thus representing a simplified model system that allows *in vitro* studies of membrane proteins in a native-like

environment (Figure 4).⁷⁹ When formed in an aqueous environment these systems spontaneously form multilamellar vesicles (MLVs) of various sizes. However, there are various preparation methods, for instance, extrusion⁸⁰ or sonication⁸¹ that alter their size. Furthermore, when working with these systems, it is important to be aware of the thermotropic phase transition from the physiological relevant fluid liquid phase to the solid gel phase.⁸² In general, the physical bilayer properties can be tuned by the choice of headgroup chemistry, degree of acyl chain saturation, and length of the acyl chains, making them a sophisticated membrane-mimetic system in the research field of membrane proteins.⁸³

1.2.1.3 Bilayered micelles

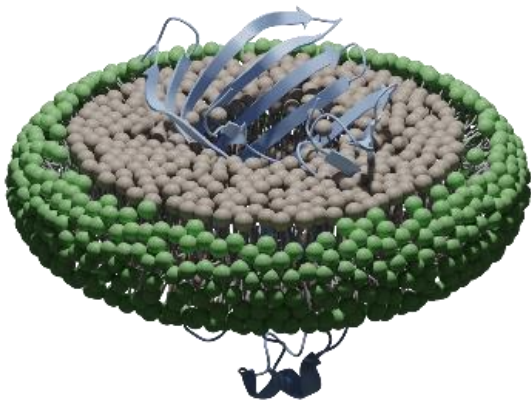


Figure 5 Illustration of a bicelle-embedded membrane protein. Short chained detergents, such as DHPC (green), stabilize a lipid patch (grey) in which a membrane protein is incorporated. PDB:1QD6

Bilayered micelles (bicelles) are nanosized lipid bilayers that are stabilized by a rim of short-chained lipids, such as 1,2-dihexanoyl-*sn*-glycero-3-phosphocholine (DHPC) (Figure 5). Noteworthy, these short-chained lipids are unable to extract membrane proteins from the membranes by themselves.⁸⁴ Therefore, bicelles have to be assembled by mixing lipids, membrane proteins, and the rim-forming agent. However, bicelle formation is only feasible under specific conditions and requires certain lipid

combinations, rendering bicelles a challenging mimetic system to work with.⁸⁵

1.2.1.4 Short amphiphilic polymers (amphipols)

Amphipols, are short amphiphilic polymers that are designed to bind to membrane proteins, thus, stabilizing them in a detergent-free aqueous solution (Figure 6).^{86,87} An

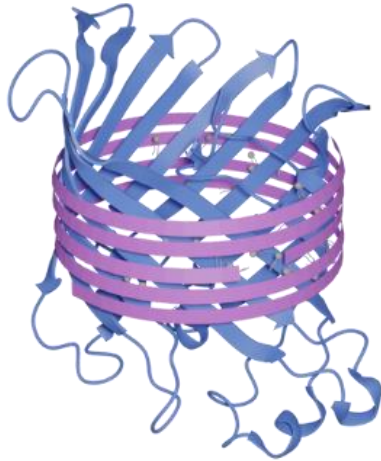


Figure 6: Illustration of an amphipol stabilized membrane protein. The amphipol (purple) wraps tightly around the hydrophobic moieties of the membrane protein. PDB:1QD6

molecules.⁸⁸ However, amphipols display a poor solubilization and extraction efficiency; therefore the conventional practice is to solubilize membrane proteins with the aid of detergents and, subsequently, exchange the detergents with amphipols.⁸⁷ This poses an issue for fragile membrane proteins, as their exposure to detergents can be detrimental to the stability and architecture of their native structure.

advantage of amphipols is the improved stabilization of fragile membrane proteins, caused by their high hydrophobicity and slow dynamic allowing them to wrap tightly around the hydrophobic cores of membrane proteins.⁸⁶ Furthermore, amphipols pose an attractive option for the study of membrane proteins in cryo-electron microscopy (cryo-EM) as they allow for the removal of excessive detergent monomers and micelles in the sample, thus decreasing the background noise imposed by such

1.2.1.5 Protein-bounded nanodiscs

Protein-bounded nanodiscs are lipid bilayer patches that are surrounded by amphipathic α -helical proteins, so-called membrane scaffold proteins (MSP), and are based on the class of apolipoprotein A1 proteins (Figure 7).⁸⁹ Generally, MSP-based nanodiscs show a narrow size distribution of around 10 nm but can be altered by adjusting their protein sequence, resulting in MSP nanodiscs of up to 90 nm.⁹⁰ To assemble these nanodiscs, MSPs are incubated in the presence of a detergent/phospholipid mixture. Upon removal of the detergent, the MSPs self-

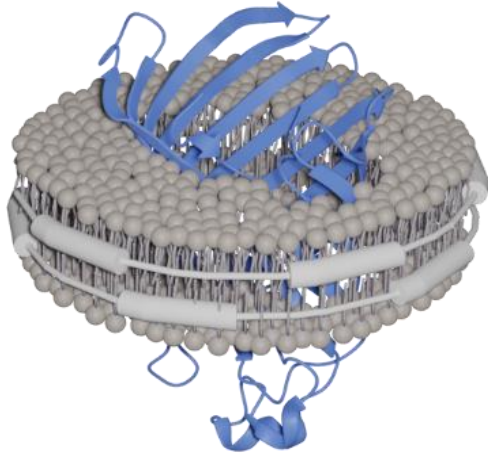


Figure 7: Illustration of a protein-bounded MSP nanodisc. The MSP (grey-white) wraps around a lipid patch in which a membrane protein is incorporated. PDB:1QD6

membrane proteins, thus disrupting the biological membrane, often leading to the destabilization of the targeted membrane protein.

assemble with the phospholipids into discoidal lipid bilayers. The so-formed nanodiscs allow for the incorporation of a broad range of membrane proteins and have proven in the past as an effective tool for the investigation of membrane proteins.^{91,92} However, these nanodiscs bear a specific disadvantage as the MSPs that encircle lipid bilayer impede with the UV detection of the encapsulated proteins. Additionally, these nanodiscs still require the usage of detergents to solubilize the

1.2.2 Detergent-free polymer-bound nanodiscs

In the following chapter a promising detergent-free membrane mimetic system, polymer-bound nanodiscs is presented.⁹³

Polymer-bound nanodiscs are lipid bilayer patches that are stabilized in solution with a belt of amphiphilic copolymers (Figure 8). Generally, amphiphilic copolymers consist of alternating hydrophobic and hydrophilic moieties. The most prominent

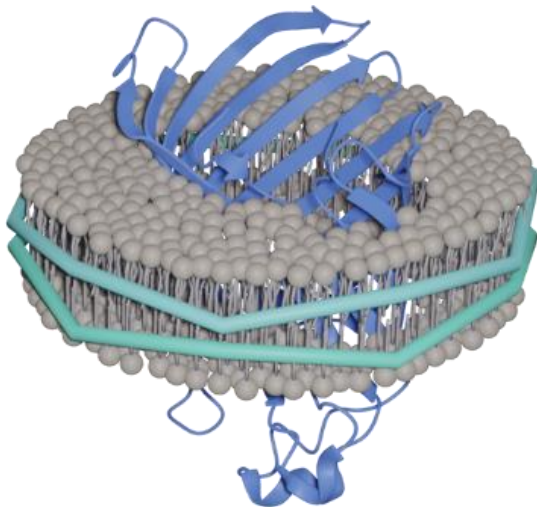


Figure 8: Illustration of a protein-embedded polymer-bound nanodisc. The polymer (cyan) wraps around a lipid patch in which the membrane protein is embedded. PDB:1QD6

representatives are styrene/maleic acid (SMA) and diisobutylene/maleic acid (DIBMA).^{94,95} SMA(2:1) is a randomly distributed amphiphilic copolymer, available at different styrene to maleic acid molar ratios, whereas DIBMA is a 1:1 alternating polymer consisting of diisobutylene and maleic acid. Of all the different blends of SMA(2:1), only two of those, SMA(2:1) and SMA(3:1) are widely used.⁹⁶ Although their structural difference, aromatic styrene for SMA(2:1)

and aliphatic diisobutylene for DIBMA, both are able to solubilize lipid bilayers and form stable discoidal aggregates so-called nanodiscs.^{94,95} The current nanodisc formation model suggests the binding and insertion of the hydrophobic group of the polymer to the membrane, mainly driven by the hydrophobic effect. By this insertion the polymer disrupts and bends the lipid bilayer, leading to the formation of a transmembrane pore and finally to the assembly of nanodiscs.^{97,98} The efficiency of the nanodisc assembly can be monitored and thermodynamically characterized by DLS and ³¹P-NMR.⁹⁹

Over the last decade, SMA(2:1) and DIBMA have obtained increased attention which originates from their ability to directly solubilize lipid bilayers. By applying these onto cellular membranes, amphiphilic polymers are able to extract and stabilize membrane proteins together with a patch of their annular lipids, in so-called nanodiscs.¹⁰⁰ This solubilization approach is independent of detergents, thus, vital protein–protein or protein–lipid interactions are preserved, allowing in this manner for the investigation of the membrane proteins in a native-like environment.⁹⁴ This is an unrivaled advantage when compared to other purification methods, which can be seen in the superior stability,^{94,101-105} the preservation of bound ligands, and a more native-like activity of membrane proteins.¹⁰⁶⁻¹⁰⁹ Moreover, polymer nanodiscs were able to extract and retain the structure of membrane protein oligomers and higher-ordered complexes, so-called metabolons, with their bound co-factors.^{94,110-114} This was a remarkable achievement as previous experiments with detergents could disrupt their higher-order structure.⁷⁶ Furthermore, polymer-encapsulated nanodiscs are subjectable to subsequent purification methods^{16,101} that usually follow after the solubilization. The purified protein-embedded nanodiscs are then amenable to an array of biochemical, structural, and biophysical techniques, allowing a thorough investigation directly in the nanodisc.^{100,102,115} Taken such investigations, in a near-native environment, stoichiometries of complete enzymatic complexes,¹¹⁴ full oligomerization states,¹¹⁶ as well as high-resolution structures¹⁰² were resolved. Additionally, this allowed for the investigation of vital protein–lipid interactions that could be identified and quantified.^{94,108}

Moreover, the investigation of membrane proteins in a near-native state is not just beneficial for academic but also for pharmaceutical research.⁶¹ This is highlighted by the binding of antibodies *in vivo* and *in vitro*, making the protein-embedded nanodisc amenable to investigations of surface plasmon resonance and fluorescence-activated cell sorting.¹⁰³ These approaches combined with structural biology allows for optimized development of new potential drugs.^{117,118}

Nevertheless, amphiphilic polymers, like SMA(2:1) and DIBMA, are not ideal tools and as all the other available membrane mimetic systems they have few drawbacks as well. Given their high content of maleic acid, SMA(2:1) and DIBMA carry a high charge density with them. This can result in a strong Coulombic repulsion between the polymer–polymer or polymer–membranes.^{95,119-121} Furthermore, it was reported that this high charge density can possibly lead to unwanted and unspecific interactions between the polymer and the protein hindering such a way the functional study of the protein.¹²² Another issue that arises with the high charge state is the interference with certain experimental techniques, e.g., cell-free protein translation or sodium dodecyl sulfate polyacrylamide gel electrophoresis (SDS-PAGE).^{16,103} Additionally, SMA(2:1) and DIBMA display a weak compatibility with divalent cations, which can lead to their precipitation and thus to the aggregation of the embedded membrane proteins.^{121,123} Furthermore, an increasing number of studies report on how lipid composition, lipid charge as well as phase state, affect the solubilization.^{95,96,124,125} To overcome these pitfalls and improve the solubilization efficiency of amphiphilic polymers towards specific lipid compositions, tremendous efforts have been undertaken by many groups to functionalize those polymers.¹²⁶⁻¹³⁰

One of the approaches to functionalize SMA was performed by the addition of a thiol group (SMA-SH). This allowed the purification of the nanodiscs through an affinity chromatography.¹²⁹ Another approach was to incorporate phosphocholine pendant groups to SMA (zSMA) and by this create a zwitterionic polymer that does not cause unspecific, charge-related, interactions between polymers and proteins.¹²⁶ It is worth mentioning that zSMA was synthesized completely *de novo*, hindering the broader application throughout the field. However, due to the research presented in this thesis paired with an increased demand for zwitterionic alternatives from other groups, the group of Prof. Dr. Sandro Keller, in collaboration with Glycon chemicals, made the zwitterionic polymer alternatives Sulfo-DIBMA and Sulfo-SMA more accessible to the scientific community by making them commercially available.¹³¹

As a concluding remark, besides their short presence in the field of membrane-protein research, amphiphilic polymers have been proven as versatile tools that aid in the understanding of the membrane proteome.

1.3 Biophysical analysis methods of vesicles and nanodiscs

1.3.1 Dynamic light scattering

Dynamic light scattering (DLS), also known as quasi-electron light scattering or photon correlation spectroscopy, is a non-invasive technique used to derive the size distribution of particles in a solvent.¹³²

To this extent, DLS measures the rate at which the intensity of the scattered light fluctuates in a time-dependent manner with the aid of a single-photon counting module. The fluctuations of the scattered light are directly related to the Brownian motion of particles which is affected by the temperature and viscosity of the solvent.¹³³ There, larger particles that diffuse slower show less fluctuations in the intensity trace, thus showing broader amplitudes, whereas smaller particles diffuse faster and show higher fluctuations, therefore sharper peaks.¹³⁴ This intensity trace is then used to calculate the correlation function of the second order. In simple terms, the correlation function is a mathematical description of the scattered light fluctuations that is plotted against the time and yields information about the diffusional behavior of the particles.^{134,135} Thus, given a particle's diffusional coefficient, DT , the hydrodynamic diameter can be calculated with the aid of the Stokes-Einstein equation.¹³⁶

Primarily two approaches are being used to analyze the correlation function, which yields the distribution of the diffusion coefficients. The first approach is the cumulant analysis, a monomodal distribution method.¹³⁷ This analysis is an ISO-standardized procedure (ISO13321) that fits a mono-exponential fit to the correlation function, providing the mean values and a hypothetical gaussian distribution and not a distribution of the diffusion coefficient.¹³⁸ This mean and the distribution allow the calculation of the mean size of the particles in solution and give an estimate for the distribution width as polydispersity index (PDI).¹³⁹ The second approach is the non-negative least squares (NNLS) method or CONTIN algorithm, which are non-monomodal distribution methods.^{134,140} These try to calculate a multi-exponential function to the correlation function, obtaining a distribution of the particle diffusion coefficients in this manner. The difference between the two approaches is that the cumulant analysis considers a single population of particles, and the output is the mean value of the distribution (z-average) with a hypothetical gaussian distribution where the polydispersity index (PDI) is the assumed variance assumed of the distribution. In

contrast to the cumulant analysis, the NNLS method does not assume any diffusion or distribution properties and is adequate for poly-disperse samples.^{132,133}

The so-obtained diffusion coefficient distributions are then calculated, assuming spherical molecules, into intensity-weighted particle size distributions. In accordance with the Rayleigh approximation, the scattering intensity distribution is proportional to the particle size to the power of six (d^6), therefore bigger particles contribute to a greater extent to the intensity-weighted size distribution.¹⁴¹ In a multimodal distribution or a distribution with a substantial tail, taking advantage of the Mie theory, the intensity-weighted distribution can be converted into a volume-weighted distribution.¹⁴² This distribution represents a relative proportion of multiple sizes based on their volume or size, reducing, according to the Rayleigh approximation, the contribution of the particle sizes to the distribution to d^3 instead of d^6 , which is for the intensity-weighted size distribution.^{135,143}

1.3.2 Transmission electron microscopy

Electron microscopy can be discerned in two main techniques, scanning electron microscopy (SEM) and transmission electron microscopy (TEM). While TEM allows the formation of a direct image by transmitting a beam of accelerated electrons through the sample, SEM is forming an image by scanning the sample using a focused electron beam.^{144,145} The optical path, even in modern electron microscopes, still resembles the setup of light microscopes. The first electron microscope was developed by Ernst Ruska and Max Knoll at the university in Berlin in 1931.¹⁴⁶ Subsequently, in 1986 Ruska was awarded the Nobel prize for his “*fundamental work in electron optics and the design of the first electron microscope*”. In the ongoing years, several specialized fields have developed, such as single particle analysis of cryo-TEM data, cryo-electron tomography, electron crystallography or micro electron diffraction. In cryo-TEM, single particles from different orientations in vitreous ice are being averaged to determine their structure.¹⁴⁷ In the case of cryo-electron tomography, a sample is tilted and imaged at different angles to produce a three-dimensional view, often accompanied with subtomogram averaging which employs analogous principles to single-particle averaging.¹⁴⁸⁻¹⁵⁰ Electron crystallography acquires diffraction data from 2D crystals at different tilt angles which are combined and used for the structural determination.¹⁵¹ Micro electron diffraction is a form of electron crystallography, using 3D crystals to

determine the structure of the crystallized particle through electron diffraction.¹⁵² However, electron microscopy, and especially TEM, has vastly influenced the scientific community, e.g., in biology with the first TEM image of a virus,¹⁵³ a sectioned eukaryotic cell,¹⁵⁴ or with images of the separation of the nervous system and the communication via neurotransmitter.^{155,156}

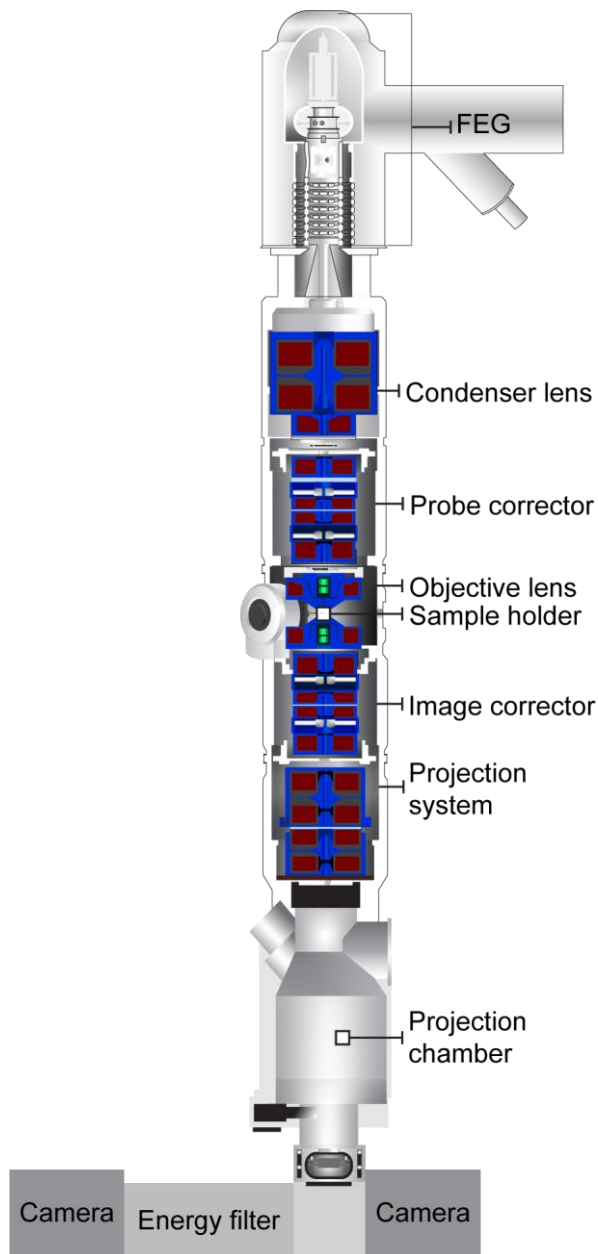


Figure 9: Schematic illustration of a transmission electron microscope. Annotated are the electron gun (FEG), the electromagnetic lenses (Condenser lens, Objective lens), the sample holder, an image corrector, the projection system, projection chamber, an energy filter, and the cameras.

The key components of a TEM are an electron gun, electromagnetic lenses, a specimen stage, and an imaging system (Figure 9). Briefly, the electron gun provides the electrons that are accelerated and guided through the column. Three types of electron guns are available in the commercially available electron microscopes namely being the LaB6 cathodes, the tungsten filaments, and the field emission guns (FEG).¹⁵⁷ Out of them, FEGs provide the most coherent electron beam.¹⁵⁸ This type of gun is connected to a high-voltage generator that applies an electrical field which accelerates the electrons. Once the kinetic energy of the electrons matches the energy of the applied field, electrons are emitted from the gun.¹⁵⁷ The wavelength of the emitted electrons depends on the applied acceleration voltage. The electromagnetic lenses are not physical lenses, but act in a matter of such for electrons. Electromagnetic lenses are strong electromagnets that create a magnetic field, thus exerting a force (Lorentz force) onto electrons, as they pass through the

electromagnetic lens system and are focused to a focal point.¹⁵⁹ However, it has to be noted that electromagnetic lenses are prone to suffer from aberrations such as

spherical aberration (C_s), chromatic aberration, astigmatism, and coma. These are caused by, e.g., physical imperfections of the coils or temperature fluctuations.^{160,161} The specimen stage is located at a focal point along the optical axis and holds the sample. For the detector or imaging system, different approaches were developed over the years such as sheet films, phosphor screens, charge-coupled device cameras (CCD), and direct electron devices (DED). The most advanced, and recent, detectors are DEDs, as they are able to directly detect electrons, and by this improve the recording speed and avoid blurring during detection.¹⁶² These key components are assisted by important support systems, such as a high-vacuum pump system. This system generates a high-vacuum inside the TEM, preventing the collision of electrons with other molecules, except the sample, on their way.

A TEM image is the result of the interactions of the electrons with the sample (and microscope parts) while passing through the sample. As electrons travel through the sample, they interact with the sample through Coulomb forces and are primarily scattered elastically or inelastically and are, subsequently, captured by the imaging system.¹⁶³ During the event of inelastic scattering, electrons interact with the nuclei of the sample atoms, transferring some of their kinetic energy and momentum and by this altering their direction and causing in organic specimens irreversible radiation damage.¹⁶³ In the event of elastic scattering electrons are electrostatically deflected by the nuclei of the atoms, introducing a phase shift and changing slightly their direction while conserving their kinetic energy. These electrons are preferred, as they do not cause damage to the sample and contain the “high-resolution” information.

Depending on the interactions with the sample, there can be distinguished two sources of contrast in TEM: amplitude and phase contrast. The amplitude contrast originates from the attenuation of the electron beam intensity, while travelling through the sample. This can be due to, e.g., the absorption of electron of the specimen or an energy filter. The phase contrast relies on the interference of the elastically and inelastically scattered electrons.¹⁶⁴ In the case of vitrified biological samples, the main source of contrast originates from the phase contrast, while the amplitude contrast has only a minor contribution. This is due to the composition of biological matter as it mainly consist of very light atoms, C, N, O, H, resulting in a density of $\sim 1.33 \text{ g/cm}^3$, compared to the density of vitreous ice $\sim 0.93 \text{ g/cm}^3$.¹⁶⁵ However, a phase contrast needs to be magnified, else in an focused and aberration free microscope nothing, besides noise, would be visible. By imposing an additional phase shift to the electrons, the difference

between the scattered and unscattered electrons is magnified. This phase shift is introduced by a manipulation of the Fourier pattern in the back focal plane and can be achieved either through a defocus or the introduction of a physical object (phase plate).^{164,166} The so-introduced phase shift in the back focal plane can be calculated by the (phase) contrast transfer function (CTF) (PhCTF):

$$PhCTF(f) = \sin\left(\frac{2\pi}{\lambda} \left(\frac{-C_s \lambda^4 f^4}{4} + \frac{z \lambda^2 f^2}{2} \right)\right)$$

With f as the spatial frequency, z as the defocus, λ as the wavelength of the electrons, C_s as the spherical aberration.¹⁶⁷ A closer investigation of the formula shows that the defocus affects the phase shift to a greater extent than the spherical aberration. Thus, imaging high-resolution data with a TEM is a compromise between contrast and high-resolution information.^{157,168}

TEM is widely used among the scientific communities and excels in imaging soft materials at higher magnifications. However, two aspects should be taken into consideration, especially when working with soft materials.¹⁶⁹ First, samples are imaged in vacuum and second, radiation damage from the electron beam. To prevent the sample from degradation and to protect it from the vacuum, preparation procedures, such as shadowing,¹⁷⁰ negative stain,¹⁷¹ and cryo-fixation (vitrification),¹⁴⁷ were developed and improved over time to allow for the imaging of materials that do not withstand the harsh conditions of the electron microscope. In the case of shadowing, a heavy metal source is placed at an inclining angle, towards the sample, and evaporated onto it, subsequently, covering the sample with heavy metal atoms creating a “shadow”, resembling the particle, on the grid.¹⁷² In the case of the negative stain preparation, samples are covered by a heavy atom salt, usually uranyl acetate, coating in this way the sample enhancing its contrast and protecting it from radiation damage. In another approach termed vitrification, a better preservation of a biological sample in its native state is attempted. In this case, an aqueous sample is plunge-frozen in liquid ethane, instantly immobilizing it in vitreous (glass-like) ice.¹⁴⁷ This freezing procedure is so fast that the water molecules are not able to form crystalline structures but rather retain their liquid amorphous nature, allowing the imaging of the particle in its native state. However, vitrified soft-matter does not offer enough amplitude contrast, thus the contrast, for such samples, relies on the above explained phase contrast.¹⁷³

1.4 Cryo-electron microscopy (cryo-EM)

Over the recent years cryo-electron microscopy (cryo-EM) is enjoying an increased popularity among the scientific community, especially in structural biology and material science but also other fields show increased interest in the technique. A main reason for this is the so-called resolution revolution in 2014 which is considered to be the start of a new era in the history of cryo-EM.^{174,175} The development of the new direct electron detector cameras combined with the availability of sophisticated and advanced computational routines, and the means to produce samples in vitreous ice allowed this major breakthrough.¹⁷⁶⁻¹⁷⁸ This presented cryo-EM as an extremely attractive technique for the whole scientific community, especially for soft matter samples, large complexes, and fragile or flexible proteins that are generally difficult to crystalize or to deal with in X-ray crystallography or nuclear magnetic resonance spectroscopy, such as membrane proteins.^{174,179} This breakthrough is reflected in the yearly increasing numbers of reported and deposited structures in the protein data bank (PDB) over the recent years for soluble complexes¹⁸⁰⁻¹⁸³ as well as membrane-bound complexes.^{184,185}

1.4.1 High-resolution cryo-EM of membrane proteins

The field of structural characterization of membrane proteins was accelerated, as over the last couple of years an increasing number of cryo-EM structures of membrane proteins were reported.⁶⁶ A statistical analysis in 2021, from Choy *et al.*, pointed out that cryo-EM is now rivaling X-ray crystallography and is on its way to be the method of choice to structurally investigate membrane proteins.⁶⁶ However, this increase in reported membrane-protein structures cannot solely be attributed to the advancements in cryo-EM but also to the increased development and improvements of membrane-mimetic systems, such as amphipol-nanodiscs, membrane scaffold protein nanodiscs, and polymer-nanodiscs.^{87,91,94} Pairing these developments with the cryo-EM advancements, for example the lower requirement in protein concentration, enabled this growth in reported membrane protein structures by cryo-EM. Moreover, these developments enabled the investigation of membrane proteins below <200 kDa.¹⁸⁶⁻¹⁸⁸

1.4.2 Single particle analysis workflow

The reconstruction of the 3D protein structures from 2D cryo-EM micrographs has come a long way since the first reconstructed structure in 1968 from De Rosier and Kluge.¹⁸⁹ Since then, image analysis algorithms were continuously improved over the years with the first major breakthrough being the cross-correlation algorithms that facilitated the grouping of single particles to 2D classes, thus increasing the signal to noise ratio.¹⁹⁰ Further improvements were then made by Sigworth and later Scheres advancing the alignment and classification of single particles by introducing the maximum likelihood algorithm.^{191,192} The maximum likelihood algorithm surmounted the problem of particle alignment, which previously existed in the principal component analysis of Van Heel & Frank, by aligning and grouping the particles through iterative calculations of model parameters. Later on, Scheres introduced then an expectation-maximization algorithm which optimized the probability of the model to properly represent the 2D data - in this manner, achieving optimally projected 2D images and 3D reconstructions.^{193,194}

Nowadays the single particle cryo-EM image analysis workflow became a more-or-less standardized pipeline, with certain specialized reconstruction methods, e.g. helical reconstruction.¹⁹⁵ However, the single-particle image analysis workflow is not the only way to reconstruct the 3D structure of a protein with the help of an electron microscope. Methods such as sub tomogram averaging and micro electron diffraction are other suitable ways to achieve the 3D structure of a protein and were mentioned above (cf. chapter 1.3.2). However, in this thesis only the single particle cryo-EM image analysis was utilized and will be the further focus of this chapter.

After image acquisition, acquired micrographs are corrected for any beam-induced motion that occurs while imaging. This beam-induced motion is due to the modern imaging technique of micrographs, or movies. There the electron dose is spread over multiple frames, rather than exposing the sample to the full dose at once, reducing, in this manner, the visible damage of the electron beam on the sample during acquisition. During this process the electron beam can drift, thus causing a slight displacement of the imaged location causing a blur over the single frames. This blur is corrected by averaging the movie's frames to a single micrograph.¹⁹⁶ Moreover, as the electron dose is spread over the frames, later frames will have a higher contrast but also a greater extent of beam damage. By simultaneously dose-weighting the frames, the areas with

the highest beam damage are excluded, while retaining the highest amount of high-resolution information.¹⁹⁷ Thereafter, the contrast transfer function (CTF) parameters of the micrographs are estimated, producing their power spectrum which is also known as Thon rings.¹⁹⁸ The CTF is an oscillatory function that describes how the contrast (information) is transferred to an image in terms of spatial frequencies. There, each frequency component, low or high, represents lower or higher resolution, reflected in brighter and darker areas, respectively, in the power spectrum. Depicted at the edges of the power spectrum is the Nyquist limit—based on the Nyquist-Shannon sampling theorem— which describes in the context of cryo-EM the maximum theoretical achievable resolution and is imposed by the pixel size and refers to a value that is 2x the recorded pixel size. Moreover, the CTF mathematically describes how the obtained image is modified through aberrations. Furthermore, the obtained power spectrum can be used to judge the quality of the micrograph, thus helping to curate the dataset of bad micrographs.¹⁹⁸

Thereafter, the micrographs are ready for the particle picking and their subsequent extraction. Particles can either be picked manually, or automatically through an algorithm which can rely on either a fed template or just picking any density found on the micrograph, given the diameter of the particle, or even newer functions employing artificial intelligence-based algorithms.¹⁹⁹ The step that follows is termed particle extraction, at which the picked particles are extracted. The box size that is used should be big enough to include part of the surrounding space around the particles. As a rule of thumb, the extraction box size should have roughly 150% of the size of the picked particles. The so included “background”, surrounding the particle, aids later in the distinction of signal-to-noise in the 2D classification.²⁰⁰

Once picked and extracted the particles are being classified based on their similarities through a maximum-likelihood algorithm into different 2D classes, based on the x,y-translation of their rotation and the CTF of the particle image. Due to the averaging of many similar particles into 2D classes, the signal to noise ratio improves, in comparison to single particles, revealing this way prominent structural features. The so classified 2D classes can then be inspected to filter out junk classes, such as classified noise or damaged particles, improving the dataset that is further used in the analysis. This is usually performed in an iterative manner, repeating the steps of 2D classification and the subsequent curation of the dataset until only good classes remain.

The so far cleaned dataset can then be used for a 3D reconstruction, as each particle is a projection of the 3D particle. One issue that arises here is the orientation of the 2D projected particle into the 3D space. Therefore, reference models can help to overcome this issue by matching the 2D projection to the reference model, but availability is still a limiting factor of such an approach. Careful utilization of reference models in any step of image processing, should, in general, be employed due to probable Einstein-from-noise effects.²⁰¹ In cases where there is no reference model available the iterative maximum-likelihood and expectation-maximization algorithms projects the 2D particle projections into an 3D *ab-initio* model. Thereafter this model is used for the next cycle, optimizing the projection assignment of the 2D projections to the 3D model and improve by this its resolution. Once the algorithm reaches a point where the next iteration is not resulting in a significant improvement of the resolution of the 3D reconstruction, the algorithm stops and produces a reconstructed 3D electron density map. The so-obtained 3D electron density map can then further be improved the by various operations such as, symmetry expansion, local particle motion correction, per-particle CTF refinement, etc., or through parameters that are specific towards the microscope such as the cameras modular transfer function. The final step of the workflow is the visual inspection of the reconstructed 3D electron density map and its Fourier Shell Correlation (FSC). The FSC is a well-established criterion in structural biology and has become the standard quality measure of the reconstructed model. It measures the cross-correlation coefficient between two 3D volumes, which were independently determined, over corresponding shells in the Fourier space.²⁰²

1.5 Model proteins

1.5.1 Formate channel A – FocA

Formate is a characteristic metabolite in the anaerobic metabolism of enterobacteria and can be used as an energy source. Moreover, formate is involved in a multitude of different metabolic processes, thus, being a major component of the cellular carbon flux in enterobacteria.²⁰³ One protein that is involved in the translocation of formate is the formate channel A (FocA). FocA is a homo-pentameric ion channel and belongs to the family of formate-nitrate transporters (FNT) which is widespread in bacteria, some archaea, and fungi.²⁰⁴⁻²⁰⁷ Each of the FNT protomers possesses a pore through which small monovalent anions, such as formate, hydrosulfide or nitrate are translocated

across biological membranes.²⁰⁶ The tertiary structure of the FocA protomer resembles that of the tetrameric aquaglyceroporin channels,^{205,206} with the central part of the approximately 20 Å wide pore connecting the cytoplasm and periplasm by funnel-like vestibules. The hydrophobic core of the pores is bound by two narrow constriction sites that restrict anion access from the vestibules. In the cell, FocA passively exports metabolized format out of the cytoplasm, however, once the pH of the surrounding changes to below 6.8, FocA is able to switch from exporting the formate to importing it back into the cell.²⁰⁸ In the past, several studies tried to elucidate the different mechanisms that control the direction of the flow throughout the pore, however, the precisely controlled mechanisms remain unclear and require further experimental validation.²⁰⁹

1.5.1 1L-myo-inositol-1-phosphate synthase – MIPS

The enzyme 1L-myo-inositol-1-phosphate synthase (MIPS) is a homo-tetramer and occupies a pivotal role in the inositol pathway. It catalyzes an internal cyclization of D-glucose-6-phosphate (Glu6-P) to the direct precursor of inositol, 1L-myo-inositol-1-phosphate.²¹⁰ This reaction consists of a tightly coupled reduction and oxidization and is the limiting step in the inositol pathway with MIPS being the only known enzyme catalyzing this specific reaction.²¹¹ Inositol and its precursor are essential in the development of many animals, microorganisms, and plants, where it is involved in a multitude of cellular processes, such as stress response, signal transduction, and membrane formation, including the biosynthesis of phosphatidylinositol (PIP) and glycosylphosphatidylinositol (GPI).²¹² Interestingly, MIPS can be found in procaryotic as well as eukaryotic organisms, where it is localized in the cytoplasm, organelles, and at cellular membranes.^{210,213,214} Furthermore, a sequence alignment across multiple different organisms, including *S. cerevisiae*, *Phaseolus vulgaris*, and *Entamoeba histolytica* revealed considerable conservation of the primary structures of MIPS, highlighting the importance of this enzyme and its catalyzed reaction.^{212,215} Although the enzyme has been observed to be membrane-associated in specific conditions,²¹³ its biochemical and structural characterization in a membrane extract has not been yet performed.

2 Aim of this thesis

The aim of this thesis was the evaluation of different membrane mimetic systems for the investigation of membrane proteins by cryo-EM with the focus on polymer nanodiscs of different charge. The focus was set on polymer nanodiscs to identify their applicability in cryo-EM to observe membrane proteins in a close-to-native state.

In the first part, the conventionally detergent-purified membrane protein FocA was structurally characterized using cryo-EM. The resolved structure was used to identify and characterize the active pore of a protomer from FocA. These findings aid to update the previously resolved structure of a N-terminal truncated version of FocA and further aid in the understanding of its import/export mechanism.

In the next part, amphiphilic polymers of different charge were used to solubilize multi-component vesicles to probe their solubilization efficiency and behavior on membranes that mimic the inner mitochondrial membrane composition of pig heart, *Saccharomyces cerevisiae* and *Myceliophthora thermophila*—as analogue for *Chaetomium thermophilum*. To this extent, multi-component vesicles that mimic the inner mitochondrial lipid composition and the membrane composition of a thermophilic fungus were formed, from artificial and natural lipids and were, subsequently, characterized. Thereafter, the so-formed vesicles were solubilized by polymers of different charge. As the solubilization of membranes is a complex mechanism, which is, yet, not fully understood, the solubilization of these different membranes was investigated. The so-formed nanodiscs were morphologically characterized through DLS, negative stain electron microscopy (NS-EM), and cryo-EM.

The best solubilizing polymer, from the previous experiments, will be taken for subsequent solubilization experiments of membranes from the eukaryotic organism *C. thermophilum* to extract and stabilize membrane proteins in a close-to-native environment. The so-purified membrane proteins will be investigated through size exclusion chromatography (SEC), sodium dodecyl sulfate polyacryl amide gel electrophoresis (SDS-PAGE), NS-EM, cryo-EM, and mass spectrometry, developing this way new workflows for further applications.

3 Materials and methods

3.1 Materials

This chapter lists all chemicals, buffers, cellular sources, lipids, polymers, and proteins that were used in this thesis.

3.1.1 Chemicals

Table 1: All chemicals that were used in this thesis.

Chemicals and enzymes	Source	Identifier
1,4-Dithiothreit, min. 99 %, p.a.	Carl Roth	6908.4
Acrylamide/Bis solution, 37.5:1	Serva	10688.01
Agar-Agar, bacteriological highly pure	Carl Roth	2266.3
Aprotinin from bovine lung	Sigma-Aldrich	A1153-1MG
Bestatin, 10 mg	Sigma-Aldrich	10874515001
Chloroform	Carl Roth	67-66-3
D-Sucrose, ≥99,5%, p.a.	Carl Roth	4621.1
D (+)-Glucose p. a., ACS, anhydrous	Carl Roth	X997.2
Dextrin for microbiology (from potato starch)	Carl Roth	3488.1
di-Potassium hydrogen phosphate trihydrate	Carl Roth	6878.1
di-Potassium hydrogen phosphate, ≥99%, p.a., anhydrous	Carl Roth	P749.1
DNase I	Sigma-Aldrich	10104159001
E-64	Sigma-Aldrich	E3132-1MG
ECL fluorescent mixture	BIO-RAD	1705062
EDTA disodium salt dihydrate, min. 99%, p.a., ACS	Carl Roth	8043.2
Glycine	Serva	23391.02

HEPES PUFFERAN®, min. 99.5 %, p.-1 kg	Carl Roth	9105.3
Iron (III) sulphate hydrate, 80 %, pure	Carl Roth	0492.1
Isopropanol	Carl Roth	CP41.1
Leupeptin	Sigma-Aldrich	L2884-1MG
Magnesium chloride hexahydrate, min. 99%, p.a., ACS	Carl Roth	2189.1
Magnesium sulphate heptahydrate, ≥99%, p.a., ACS	Carl Roth	P027.1
Methanol	Carl Roth	4627.6
Pefabloc	Sigma-Aldrich	11585916001
Pepstatin A	Sigma-Aldrich	77170-5MG
Peptone ex casein	Carl Roth	8986.1
Phosphate buffered saline tablets (PBS)	Sigma-Aldrich	P4417
Potassium chloride min. 99.5%, 1 kg	Carl Roth	6781.1
Potassium dihydrogen phosphate, ≥99%, p.a., ACS	Carl Roth	3904.2
Precision plus protein all blue standards (marker)	BIO-RAD	161-0373
Sodium chloride 99,5%, p.a., ACS, ISO	Carl Roth	3957.2
Sodium dodecyl sulfate (SDS)	Carl Roth	0183.2
Sodium nitrate, ≥99 %, p.a., ACS, ISO	Carl Roth	A136.1
TEMED	Carl Roth	2367.3
Tris	Carl Roth	AE15.2
Tris hydrochloride	Carl Roth	9090.2
Tween 20	Carl Roth	9127.1
Tryptone	Sigma-Aldrich	T7293
Yeast extract, micro-granulated	Carl Roth	2904.3

β -mercaptoethanol	Sigma-Aldrich	444203-250ML
--------------------------	---------------	--------------

3.1.2 Buffers

Table 2: List of all buffers with their components that were used in this thesis.

Buffer	Ingredients	pH
1 L CCM-media	3 g Sucrose, 0.50 g NaCl, 0.65 g K ₂ HPO ₄ x 3 H ₂ O, 0.50 g MgSO ₄ x 7 H ₂ O, 0.01 g Fe ₂ (SO ₄) x 3 H ₂ O, 5 g tryptone, 1 g peptone, 1 g yeast extract, 15 g dextrin	7.4
CCM-agar plates	3 g Sucrose, 0.50 g NaCl, 0.65 g K ₂ HPO ₄ x 3 H ₂ O, 0.50 g MgSO ₄ x 7 H ₂ O, 0.01 g Fe ₂ (SO ₄) x 3 H ₂ O, 5 g tryptone, 1 g peptone, 1 g yeast extract, 15 g dextrin	7.4
Lysis buffer	100 mM HEPES, 95 mM NaCl, 5 mM KCl, 1 mM MgCl ₂ , 0.5 mM EDTA, 5% Glycerol	7.4
Solubilization buffer	50 mM Tris, 200/500 mM NaCl	7.4
Protease inhibitor cocktail	1 mM DTT, 10 μ g/mL DNase, 2 mM Pefabloc, 40 μ M E-64, 130 μ M Bestatin, 0.5 μ M Aprotinin, 1 μ M Leupeptin, 60 μ M Pepstatin A	-
4x SDS sample buffer	250 mM Tris-HCL, 8% (w/v) SDS, 0.2% (w/v) bromphenol blue, 40% (v/v) Glycerol, 20% (w/v) β -mercaptoethanol	6.8
1 L SDS running buffer	3.03 g Tris, 14.4 g glycine, 0.1% (w/v) SDS	8.3

3.1.3 Cellular sources

The model organism *Chaetomium thermophilum* var. *thermophilum* La Touche 1950 (*Thermochaetoides thermophila*²¹⁶) was purchased from DSMZ (Leibniz Institute DSMZ-German Collection of Microorganisms and Cell Cultures, Germany). The spores were cultivated as recommended by the company guidelines.

3.1.4 Lipids, polymers, and proteins

Table 3: List of all lipids, polymers, and proteins used in this thesis. A precise composition of the lipids from the respective compositions can be found in the appendix.

1	Type	Company
Sokalan 9, DIBMA	Polymer	Kind gift from BASF
SMA(2:1)	Polymer	Polyscope

Sulfo-DIBMA	Polymer	Kindly provided by Prof. Dr. Sandro Keller
Glyco-DIBMA	Polymer	Kindly provided by Prof. Dr. Sandro Keller
QA1-SMA	Polymer	Kindly provided by Dr. Adrian Kopf
QA2-SMA	Polymer	Kindly provided by Dr. Adrian Kopf
Cardiolipin (CL)	Lipid	Avanti Polar Lipids
Bovine heart cardiolipin, sodium salt (Heart-CL)	Lipid ^a	Avanti Polar Lipids
Bovine liver L- α -Phosphatidylinositol, sodium salt (Liver-PI)	Lipid ^a	Avanti Polar Lipids
Bovine heart L- α -Phosphatidylethanolamin (Heart-PE)	Lipid ^a	Avanti Polar lipids
Bovine heart L- α -Phosphatidylcholin (Heart-PC)	Lipid ^a	Avanti Polar lipids
Soy L- α -phosphatidylglycerol sodium salt (PG)	Lipid ^a	Avanti Polar Lipids
1-Palmitoyl-2-linoleoyl- <i>sn</i> -glycero-3-phosphocholine (PC)	Lipid	Avanti Polar Lipids
1-Palmitoyl-2-oleoyl- <i>sn</i> -glycero-3-phosphoethanolamine (PE)	Lipid	Avanti Polar Lipids
1-Palmitoyl-2-oleoyl- <i>sn</i> -glycero-3-phospho-(1'- <i>rac</i> -glycerol) (PG)	Lipid	Avanti Polar Lipids
1-Palmitoyl-2-oleoyl- <i>sn</i> -glycero-3-phosphoinositol (ammonium salt) (PI)	Lipid	Avanti Polar Lipids
1-palmitoyl-2-oleoyl- <i>sn</i> -glycero-3-phospho-L-serine (sodium salt) (PS)	Lipid	Avanti Polar Lipids
1-palmitoyl-2-linoleoyl- <i>sn</i> -glycero-3-phosphate (sodium salt) (PA)	Lipid	Avanti Polar Lipids
Ergosterol (ERG)	Lipid	Avanti Polar Lipids

^a Alcyl chain saturation of the natural lipids is described in Figure S2

3.1.5 Instruments, consumables, and software

Table 4: List of all instruments that were used in this thesis.

Instrument	Type	Company
------------	------	---------

Incubator	Heracell 150i	Thermo Fisher Scientific
Tabletop Centrifuge	Heraeus Megafuge 40 R	Thermo Fisher Scientific
Bead beater	FastPrep-24™ 5G	MP Biomedicals™
Ultracentrifuge	OPTIMA™ MAX-XP (TLA110)	Beckman Coulter
FPLC system	ÄKTA pure 25 M	Cytiva (GE Healthcare)
Plate reader	Epoch 2 Microplate Spectrophotometer	Agilent (BioTek)
Gel imaging system	ChemiDoc™ MP Imaging Systems	Bio-Rad
Thermomixer	ThermoMixer C	Eppendorf
Glow discharge cleaning system	PELCO easiGlow™	Ted Pella, Inc.
Microbalance	XPR56 Microbalance	Mettler Toledo
Particle measurement device	Litesizer 500	Anton Paar
Refractometer	Abbemat 3200	Anton Paar
Vitrification instrument	Vitrobot Mark IV System	Thermo Fisher Scientific
Microscope 1 (120 kV)	EM 900 transmission electron microscope	Carl Zeiss
Camera (Microscope 1)	SM-1k-120 slow-scan charge-coupled device (slow-scan CCD) camera	TRS
Microscope 2 (200 kV)	Glacios Cryo Transmission Electron Microscope (Cryo-TEM)	Thermo Fisher Scientific
Camera (Microscope 2)	Falcon 3EC Direct Electron Detector	Thermo Fisher Scientific
Microscope 3	JEM-3200FS Field Emission Energy Filter Electron Microscope	JEOL
Camera (Microscope 3)	K2 IS Direct Detection Camera for low dose imaging	Amtek (Gatan)

Table 5: List of all software that was used in this thesis.

Software	Source	Identifier
----------	--------	------------

3DFSC		https://3dfsc.salk.edu/
COOT	217	https://www2.mrc-lmb.cam.ac.uk/personal/pemsley/coot/
cryoSPARC	Structura Biotechnology	https://cryosparc.com/
EMAN 2.0		https://blake.bcm.edu/emanwiki/EMAN2
EPU	Thermo Fisher Scientific	https://www.thermofisher.com/de/de/home/electron-microscopy/products/software-em-3d-vis/ePU-software.html
Fiji	218	https://imagej.net/Fiji
Gctf	198	https://www.mrc-lmb.cam.ac.uk/kzhang/
Gen5™	BioTek Instruments	https://www.biotek.com/products/software-robotics-software/gen5-microplate-reader-and-imager-software/
Image Lab Software 6.1	BIO-RAD	https://www.bio-rad.com/de-de/product/image-lab-software
MaxQuant 1.6.1	219	https://www.maxquant.org/
MotionCor2	220	https://emcore.ucsf.edu/ucsf-motioncor2
MS Excel	Microsoft Corporation	https://www.microsoft.com/en-ww/microsoft-365/excel
Phenix	221	https://www.phenix-online.org
PyMOL	Schrödinger inc	https://pymol.org/
Python & Pandas	222, 223	https://www.python.org https://pandas.pydata.org
Relion 3.0	224	https://github.com/3dem/relion
UCSF ChimeraX	225	https://www.rbvi.ucsf.edu/chimerax
UNICORN 7 Workstation for ÄKTA pure, pilot, process, Ready to Process WAVE 25	GE Healthcare Europe GmbH	https://www.gelifesciences.com/en/us/shop/chromatography/software/unicorn-7-p-05649

3.2 Methods

3.2.1 Molecular biology methods

3.2.1.1 Cell culture

The fungus, *Chaetomium thermophilum*, was grown and maintained on CCM-Agar plates in an incubator at 52°C with 10% CO₂. For liquid cultures, an initial pre-culture was started. To this end, a 500 ml Erlenmeyer flask was filled with 250 mL of CCM media and inoculated from small cut-out pieces from a freshly grown agar plate, and cultivated in the incubator at 52°C with 10% CO₂ and 100 rpm. Once the pre-culture produced small spherical shaped colonies, 5 mL of the pre-culture was used to inoculate 300 mL of CCM media, which was filled into 1 L Baffled flasks, for the main culture and was grown at 54°C with 10% CO₂ and 110 rpm until the flask was at the level where the spherical shaped colonies of the organism reached 90% confluence.

3.2.1.2 Cell lysis and membrane preparation

The grown mycelium was gathered and drained through a metal sieve with 180- μ M pore size and was 3x washed with PBS and centrifuged with 2200 *g* at 4°C for 5 min. Washed mycelium was snap-frozen in liquid nitrogen and grinded down in a pre-chilled mortar to ~0.5-cm sized pieces. Subsequently, ~8 g of mycelium was taken and lysed by adding 20 mL of lysis buffer and subjected to three rounds of mechanical bead beating with a shaking speed of 6.5 mps for 25 s and 3 min rest on ice in-between the rounds in a FastPrep Tissue Homogenizer (MP Biomedical, Irvine, California, USA). The crude cell extract was centrifuged for 5 min at 4000 *g*, pelleting the major cell wall debris and any non-lysed cells. The supernatant was then ultracentrifuged at 100000 *g* for 60 min at 4°C to separate the membrane from the soluble cell extract. Afterwards, the supernatant was discarded and the membrane pellet was used for the solubilization experiments.

3.2.2 Biochemical methods

3.2.2.1 Preparation of polymer stock solutions

Sulfo-DIBMA, Glyco-DIBMA, QA1-SMA, and QA2-SMA stock solution was prepared by weighing an appropriate amount of polymer on a high-precision XPR56 microbalance (Mettler Toledo, Gießen, Germany) and resuspended in an appropriate amount of solubilization buffer to be able to create the highest polymer (P) to lipid (L) ratio $m_P/m_L = 10$. The so-obtained suspension was sonicated in an ultrasonic bath at 70°C until the solution appeared to be clear and was subsequently filtered through a 220-nm cellulose filter (Carl Roth, Karlsruhe, Germany) and stored at room temperature.

Commercially obtained DIBMA and SMA(2:1) were dialyzed against 1 L of solubilization buffer for 24 h with a buffer exchange after 16 h. Once dialyzed the polymer solution was filtered through 200-nm cellulose filter. The molar and mass concentration were determined by measuring the refractive index of the polymer solution on an Abbemat 3200 instrument (Anton Paar, Graz, Austria) and calculated by using the molar and mass refractive increments, dn/dc , as previously described in the literature.

3.2.2.2 Protein precipitation

All samples required protein precipitation before measuring them in mass spectrometry, SDS-Page, and BCA assay. To this extent, a chloroform/methanol precipitation protocol from Wessel *et. al* was adapted and employed.²²⁶ Briefly, all solvents and samples were kept on ice and have only been used ice-cold. The sample was mixed with 4x the sample volume of methanol and got vortexed thoroughly for 10 s. Thereafter, 2x the initial sample volume of chloroform was added and vortexed for 10 s. Subsequently, 3x the initial sample of ddH₂O was added and vortexed thoroughly for 15 s and is followed by a 3 min centrifugation at 14000 *g* at 4°C. After centrifugation, the upper aqueous phase is removed without disturbing the layer in between the two phases, and 4x the initial sample volume of methanol is added and vortexed thoroughly for 10 s. Once vortexed, the sample is centrifugated at 5000 *g* at 4°C for 1 min followed by a 20000 *g* centrifugation at 4°C for 4 min. The supernatant is then discarded, and the precipitate was left to air-dry overnight at room temperature

in a chemical hood. The morning after, samples that are used for BCA assay and SDS-Page were resuspended in a 2% SDS solution.

3.2.2.3 Bichonic acid assay

Determination of the protein concentration in all samples was measured with the aid of a bichonic acid assay (BCA) kit from ThermoFisher (Pierce™ GOLD BCA Protein assay Kit) (ThermoFisher Scientific Inc., Massachusetts) and was performed according to the manufacturer's instructions. Briefly, 10-20 µL of sample was pipetted into a 96-well plate and mixed with 200 µL of the component A+B solution (50:1) that was freshly prepared. After 5 min incubation at 25°C the absorption at 562 nm was measured in a plate reader (Plate Reader specifications).

3.2.2.4 Gel electrophoresis – SDS-PAGE

For sodium dodecyl sulfate polyacrylamide gel electrophoresis (SDS-PAGE) 10 µL of 4x concentrated SDS loading buffer was mixed with 30 µL of sample and incubated at 95°C for 5 min. After incubation, the sample was centrifuged at 20000 g for 1 min at room temperature. Subsequently, 10 µL of sample and 5 µL of marker were applied onto a freshly prepared 12 % polyacrylamide gel that was suspended in SDS buffer in the gel camber. The loaded chambers were then connected to a power supply and electrophorized at a constant charge of 100 V for ~90 min. Once finished, gels were stained and fixated for 60 min with Coomassie staining solution. After staining the gels were destained in ddH₂O until they appeared to have a clear background and, subsequently, imaged.

3.2.2.5 Size exclusion chromatography

In order to enrich the sample with the desired particles—nanodisc-embedded proteins—and decrease the overall sample complexity, size exclusion chromatography (SEC) was performed. To this extent, 2 column volumes (CV) of pre-cooled solubilization buffer were used to equilibrate a BioSep 5 µm SEC-S4000 500 Å, LC Column 600 x 7.8 mm (Phenomenex, Torrance, California) column. Once equilibrated, 500 µL of 250 mg/mL *C. thermophilum* membranes with 1.25 mg/mL Sulfo-DIBMA were injected into a 500 µL sample loop with a flushing volume of 1 mL and an elution

volume of 1.5 CV. The injected material was fractionated with a flow rate of 150 $\mu\text{L}/\text{min}$ into fractions of a 250 μL volume. The fractionation was monitored by measuring the absorbance at 280 nm (A_{280}). Subsequently, eluted fractions of two simultaneous experiments were pooled together and renamed as following: fraction 1–14 as high molecular weight (hMW), fraction 27–35 as medium molecular weight (mMW), and fraction 36–45 as low molecular weight (lMW). Freshly pooled samples were concentrated to a final volume of ~ 100 μL with a 100-kDA cut-off Amicon filter at 3000 g and 4°C .

3.2.2.6 In-solution digestion in the presence of RapiGest

The protocol described here was performed by Dr. Marie Alfes and is included in her courtesy.

The protein pellet obtained from precipitation was dissolved in 10 μL of 1% (m/v) RapiGest (waters) in 25 mM ammonium bicarbonate, pH 8.5 and incubated for 5 min at 100°C . For reduction of disulfide bridges, 10 μL of 50 mM dithiothreitol in 25 mM ammonium bicarbonate, pH 8.5 were added and followed by incubation at 60°C for 30 min. Alkylation by addition of 10 μL 100 mM iodoacetamide in 25 mM ammonium bicarbonate, pH 8.5, and incubation at 37°C for 30 min was then performed. RapiGest was diluted to 0.1% (m/v) with 25 mM ammonium bicarbonate, pH 8.5, and chymotrypsin (Roche) was added at a 1:50 enzyme:protein ratio followed by incubation at 24°C for 3 h. Trypsin (Promega) was added at a 1:50 enzyme:protein ratio followed by incubation at 37°C overnight. RapiGest was hydrolyzed by addition of 20 μL 5% (v/v) trifluoroacetic acid and incubation at 37°C for 2 h. The samples were then centrifuged at 16200 g for 30 min. The supernatant was collected and peptides were dried in a vacuum centrifuge. The obtained peptides were stored at -20°C .

3.2.2.7 Liquid chromatography-coupled mass spectrometry

The protocol described here was performed by Dr. Marie Alfes and included in her courtesy.

Peptides were analyzed by nano-flow reversed-phase liquid chromatography on a DionexUltiMate 3000 RSLCnano System coupled with a Q Exactive Plus Hybrid Quadrupole-Orbitrap mass spectrometer. Peptides were dissolved in 2% (v/v)

acetonitrile/ 0.1% (v/v) formic acid. For liquid chromatography 0.1% (v/v) formic acid was used as mobile phase A and 80% (v/v) acetonitrile/ 0.1% (v/v) formic acid was used as mobile phase B. Peptides were loaded onto a trap column (μ -Precolumn C18 Acclaim™ PepMap™ 100, C18, 300 μ m I.D., particle size 5 μ m) with a flow rate of 10 μ l/min. The peptides were then separated on an analytical C18 capillary column (50 cm, HPLC column Acclaim™ PepMap™ 100, C18, 75 μ m I.D., particle size 3 μ m) with a flow rate of 300 nl/min and a gradient of 4 – 90% (v/v) mobile phase B over 90 min was applied. Following chromatographic separation, the peptides were directly eluted into the mass spectrometer. Typical mass spectrometric conditions were: data depended mode; capillary voltage, 2.8 kV; capillary temperature, 275°C and polarity, positive. Survey full scan MS spectra were acquired in a mass range of 350 – 1600 m/z, with a resolution of 70000 and an automatic gain control (AGC) target at 3e6. The maximum injection time was set to 80 ms. The 20 most intense peaks were selected for fragmentation in the HCD cell with an AGC target of 1e5, a fixed first mass of 105 m/z and a normalized collisional energy of 30%. The maximum injection time for MS2 spectra was 150 ms and the resolution of MS2 spectra was 17,500. Ions with a charge of 1 and > 8 were excluded from fragmentation and previously selected ions were dynamically excluded for 30 s. For internal mass calibration the lock mass option was enabled using the lock mass m/z 445.120025

3.2.2.8 Data analysis of mass spectrometry data

Mass spectrometry data were analyzed using the software MaxQuant²¹⁹ (version 1.6.17.0) and performing a database search against the *C. thermophilum* UniProt database (UniProt, Proteome ID: UP000008066, version data: 9th September 2021). In the analysis, the following standard parameters were used: variable modifications, oxidization (methionine) and acetylation (protein N-terminus); fixed modification, carbamidomethyl (cysteine); max missed cleavage sites, 2; min peptide length, 7; max peptide mass 6000 Da; peptide FDR, 0.01; protein FDR, 0.01 and enzyme, trypsin/P (cleavage C-terminal of lysine or arginine also when the C-terminal amino acid is proline) and chymotrypsin. Additionally, the MaxQuant LFQ as well as the iBAQ options were enabled. Thereafter, the LFQ values were isolated from the “proteinGroups.txt” result file and used for the Proteome wide Blastp analysis and the identification of membrane proteins.

3.2.3 Biophysical methods

3.2.3.1 Preparation of vesicles

All lipid mixtures were prepared by dissolving the purchased lipid powders in chloroform and combining the appropriate volumes of each lipid. Once mixed, the lipid mixtures were split into smaller aliquots. The organic solvent was evaporated from the lipid containing solution under a constant stream of N₂ and was, subsequently, placed in a vacuum for 8 h to remove any residual solvent. Lipid films were stored under an argon environment at -80°C, until further usage. Before usage, the dried lipid films were rehydrated by adding buffer consisting of 50 mM Tris at pH 7.4 containing either 200 mM or 500 mM NaCl to a final volume of 1 mg/mL. The lipid suspension was subsequently vortexed for 5 min at 22°C and subjected to an 11-fold extrusion through a polycarbonate membrane with a pore diameter of 100 nm in a Mini Extruder (Avanti, Alabama, USA). Large unilamellar vesicle (LUV) formation was confirmed by DLS, and a hydrodynamic diameter of ~160 nm for the LUVs was observed.

3.2.3.2 Preparation of protein-free polymer-bound nanodiscs

Preparation of nanodiscs, from artificial membranes, was done by adding the appropriate amount of the respective polymer solution to vesicles to achieve the desired mass ratio of polymer (P) to lipid (L) $m_P/m_L = 0.25-10$. Once mixed, the suspension was incubated for 16 h at 35°C at 700 rpm and directly used for further experiments.

3.2.3.3 Preparation of protein-containing polymer-bound nanodiscs

The isolated native *C. thermophilum* membrane pellet was solubilized by adding Sulfo-DIBMA to the pellet to a final concentration of 250 mg/mL of *C. thermophilum* membranes and 1.25 mg/mL of Sulfo-DIBMA, resulting in a $m_P/m_L = 0.005$ and supplemented with a protease inhibitor cocktail (Table 2). The solution was homogenized by subjecting it to approximately 20x strokes in a Potter-Elvehjem tissue grinder (Corning, New York, USA). The homogenized solution was incubated on a rotary shaker at 37°C at 700 rpm for 16 h and, subsequently, ultracentrifuged for 100000 g at 4°C for 80 min. The supernatant was used for further experiments, and the pellet was rehydrated in an equal volume to the supernatant of 2% SDS.

3.2.3.4 Dynamic light scattering

All dynamic light scattering (DLS) experiments were performed on a Litesizer 500 instrument (Anton Paar, Graz, Austria), which is equipped with a 633-nm He-Ne laser and the signal was detected in a 90° detection angle. Samples containing nanodiscs from *C. thermophilum* membranes were measured in a 3 mm x 3 mm quartz glass cuvette (Hellma, Munich, Germany), whereas samples containing vesicles or nanodiscs from artificial lipid compositions were measured in 1.5-mL disposable cuvettes with a cross-section of 12.5 mm x 12.5 mm (Brand, Wertheim, Germany). Prior to measurements, samples were thermally equilibrated at 25°C for 2 min and subsequently measured 6 times. During the data analysis, any effects of the buffer components and their concentration, affecting the refractive index (RI) and the viscosity, were accounted for. A non-negatively constrained least-squares function, further regularized by a so-called Tikhonov regularization²²⁷ was applied, using the Kalliope software (Anton Paar, Graz, Austria) to fit the autocorrelation function,¹³⁴ yielding the intensity-weighted particle size distribution and by a cumulant analysis the z-average particle diameter as well as their associated polydispersity indices (PDIs). The distribution width of the z-average diameter, σ , was calculated according to $\sigma = (\text{PDI})^{1/2} z$.²²⁸ For multimodal distributions, the position of the first peak, corresponding to the smallest particle size, was connected to the hydrodynamic particle diameter, which is substantiated by the strong correlation of light scattering intensity and particle size.

3.2.3.5 Proteome wide blastp and membrane protein identification

First, a local installation of the blast suite (NCBI blast 2.113.0+) was performed and all entries of the UniProt proteome (UP000008066) were downloaded and subsequently blasted against the Swiss-Prot database (downloaded 06.04.2022) by executing the following command:

```
“blastp -db SwissProt -query <input fasta> -out <result txt file>”
```

This resulted in a text file from which the top 10 blast hits were selected and their corresponding uniprot information file was downloaded. Subsequently, the information, if available, of the organism as well as the subcellular localization was isolated from

these files. In order to be considered a membrane protein and filter out false positive hits, at least 50% of the top 10 blast hits required to have the tag “membrane” in the subcellular localization field.

3.2.3.6 Negative stain EM sample preparation

Negative stain samples were prepared by applying 10 μL of protein-free polymer-encapsulated nanodiscs (0.05 mg/mL lipid) onto continuous 10–12 nm carbon coated grids with a 300 mesh size (Quantifoil, Micro Tools, Großlöbichau, Germany). Prior to usage, grids were glow discharged with 15 mA, grid negative, at 0.4 mbar, and 25 s glowing time using a PELCO easiGlow™ (Ted Pella Inc, Redding, California). After 1 min, any excessive liquid was blotted off with ash-free filter papers and subsequently, two times washed with 15 μL distilled water. Afterwards, 5 μL of 2% (*w/v*) aqueous uranyl acetate solution ($\text{UO}_2(\text{CH}_3\text{COO})_2 \cdot 2\text{H}_2\text{O}$) was applied and subsequently blotted off after 1 min. Grids were then covered and left to air-dry overnight.

3.2.3.7 Image processing of negative-stain data and size calculations

A total of 660 micrographs were collected for the dataset that was used for the statistical size analysis of protein-free nanodiscs from an artificial lipid mixture. Micrographs were recorded as movies with 15 fraction movies with a dose of $30 \text{ e}^-/\text{\AA}^2$ at a pixel size of 0.9612 \AA and were subsequently imported into Relion 3.0.²²⁴ There the movies were motion corrected, averaged and, dose weighted using the MotionCor2 software.²²⁰ Quality of the contrast transfer function (CTF) and estimation of the defocus and astigmatism were evaluated by GCTF.¹⁹⁸ For the 2D classification 37623 particles were picked manually, and subsequently, 2D classified into 100 classes. Obvious junk classes were discarded, resulting in 39 classes, containing 83.46% (31401 particles) that were selected for the further analysis. The measurements of the particle sizes were performed in FIJI.²¹⁸ There, the minor and the major axis was measured and used to calculate the average diameter of the particles.

3.2.3.8 Cryo-EM sample preparation

Cryo-EM samples were prepared by applying 3.5 μL of the sample on holey carbon support films, type R2/1 on 200 mesh copper grids (Quantifoil, Großlöbichau,

Germany). Before usage, the grids were glow-discharged with 15 mA, grid negative, at 0.4 mbar, and 25 s of glowing time, using a Pelco easiGlow™ apparatus (Ted Pella Inc, Redding, California). Once the sample was applied, excessive liquid was blotted away from the grids with Vitrobot Filter Paper (Grade 595 ash-free filter paper ø55/20 mm) and subsequently plunge frozen in liquid ethane using a Vitrobot Mark IV System (Thermo Fisher Scientific, Hillsboro, Oregon, USA). During the whole procedure, a constant temperature of 4°C and 95% humidity was maintained in the chamber. Subsequently, vitrified grids were clipped and loaded onto a Glacios 200 kV cryo-electron transmission microscope (Thermo Fisher Scientific, Eindhoven, Germany). Image acquisition was performed using a Falcon 3EC direct electron detector. Prior to imaging, the electron beam was aligned to be parallel and in the perpendicular to the sample and confined to a diameter of 2.5 µm using a 70 µm condenser aperture. Also, the numerical aperture of the objective lens was restricted to 14.7 mRad using a 100 µm objective aperture.

3.2.3.9 Size analysis of native nanodiscs in cryo-EM

The size analysis of native nanodiscs in cryo-EM was performed using the 2D classes. There the minor and major axis of the nanodiscs was measured in Fiji. The measured axis was then weighted by the particles in each class. Overall, the best 2D classes containing, 64827 particles, were taken and their minor and major axis was measured and used to calculate the weighted average diameter of the particles.

3.2.3.10 Image analysis and modelling of cryo-EM Data

FocA

Image analysis was performed in cryoSPARC v3.1.0.²²⁹ Collected movies were aligned and corrected for beam-induced motion and drift with MotionCor2.²²⁰ Contrast transfer function (CTF) was estimated using gCTF in cryoSPARC 3.1.0. Particles were automatically picked with the template picker in cryoSPARC, where clear templates from a previous acquisition were used. The resulting 1767285 particles were extracted and subsequently subjected to an iterative reference-free 2D classification. The best resulting classes, containing 236209 particles, were chosen and used for another round of iterative reference-free 2D classification.

Particles that did not meet the quality required for 2D class averaging were eliminated, resulting in a total of 192440 particles, which were used for homogenous refinement with an imposed C5 symmetry that produced a map of 3.88 Å. The PDB ID: 3KCU was downloaded, low-pass filtered to 40 Å, and used as an initial reference for this refinement. These same particles underwent local CTF refinement in cryoSPARC and were subsequently used for two more rounds of homogenous refinement, resulting in an overall resolution of 3.11 Å.²³⁰

The initial model (PDB ID: 3KCU) was fitted into the final map using Chimera²³¹ and was subsequently real-space refined in PHENIX.²³² The real space refined model was manually assessed in COOT.²¹⁷ After further refinement, C5 symmetry was manually applied to generate the final complete model.

Analysis of the channel was performed with MoleOnline. The mode was switched to pore mode and the parameters used for the analysis were as follows: probe radius 13 Å; interior threshold 0.8 Å. Residue-based polarity values were also calculated using build-in a build-in scale in MoleOnline.

Myo-inositol-phosphate synthase (MIPS)

Image analysis was performed in cryoSPARC v3.1.0. Collected movies were aligned and corrected for beam-induced motion and drift with Patch Motion (Multi). Contrast transfer function (CTF) was estimated using Patch CTF (Multi) cryoSPARC 3.1.0. Particles were picked automatically with in a reference-free manner, employing the Blob Picker algorithm of cryoSPARC which resulted in a total of 1720004 picked particles and was followed by their subsequent extraction and 2D classification into 200 classes. Junk classes were discarded and the left-over particles were re-classified. This process was repeated until clear 2D classes were obtained. After the last iteration of 2D classification, a distinctive looking group of 2D classes, containing 11836 particles, was used for *ab-initio* classification. The obtained reconstruction, was later identified as the myo-inositol-1-phosphate synthase complex, and got further refined by the Homogenous Refinement (new) method, built-in in cryoSPARC resulting a 6.62 Å cryo-EM map. Further refinement was performed by a D2 symmetry expansion that resulted in a total stack of 38628 particles. The so-obtained particles were used the local refinement operation in cryoSPARC, finally, resulting in a cryo-EM map with a resolution of 4.73 Å (FSC = 0.143).

Unknown nanodisc-embedded membrane protein

Image analysis was performed in cryoSPARC v3.1.0. Collected movies were aligned and corrected for beam-induced motion and drift with Patch Motion (Multi). Micrograph CTF was estimated using Patch CTF (Multi) in cryoSPARC 3.1.0. Particles were picked automatically in a reference-free manner, employing the Blob Picker algorithm of cryoSPARC which resulted in a total of 1720004 picked particles and was followed by their subsequent extraction and 2D classification into 200 classes. Junk classes were discarded and the left-over particles were re-classified. This process was repeated until clear 2D classes were obtained. A group of 2D classes, containing 7253 particles, was taken for *ab-initio* reconstruction. The so-obtained reconstruction was then processed for a non-uniform refinement operation in cryoSPARC, resulting in a cryo-EM map with a resolution of $\sim 18.59 \text{ \AA}$ (FSC = 0.5).

4 Results and Discussion

4.1 Detergent-mediated membrane mimetic system: The membrane protein FocA in detergent micelles

4.1.1 Structural analysis of FocA by single-particle cryo-EM

Imaging of purified FocA by negative stain electron microscopy (NS-EM) allowed for the investigation of the sample and its particle distribution on an electron microscopy grid. A typical micrograph can be seen in Figure 10A. There, a homogenous, white, and round in shape looking particle, distributed over the whole grid, was observed (Figure 10A, black arrow). However, only top and bottom views of the particle were observed and no side views, pointing out an issue with a preferential orientation in negative stain. As this sample consisted only of the purified protein FocA in DDM micelles and the particles had a diameter of about ≈ 10 nm, the particles were identified as FocA. To gain more insight on the structural features of FocA, negatively stained particles were picked (Figure 10B) and subsequently 2D classified (Figure 10C). Indeed, 2D class averages revealed structural features, resembling the architecture of FocA that are comparable to previously published results, e.g., pentameric assembly of FocA subunits.²⁰⁶ Based on the quality of the initial screening data obtained with NS-EM, the sample was judged suitable for vitrification and subsequent cryo-EM data collection and analysis.

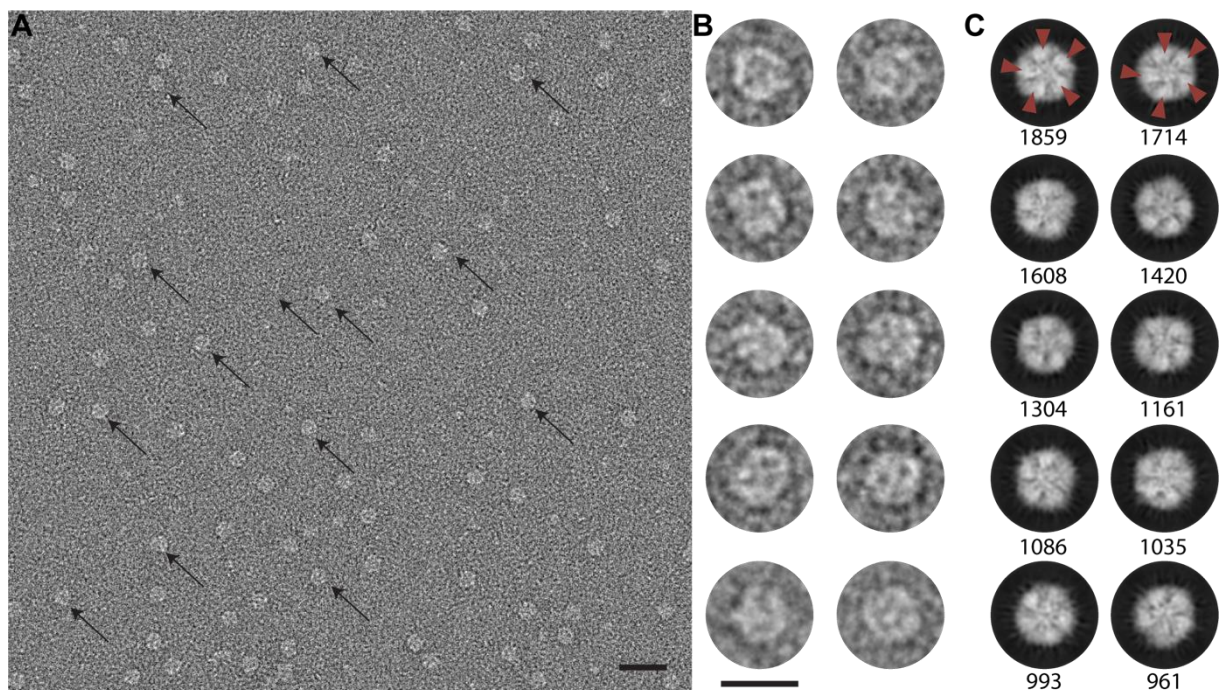


Figure 10 Micrograph, picked particles and 2D classification of negatively stained FocA. (A) Representative micrograph of negative stained FocA. Micrograph reveals top and bottom

orientations of FocA that are annotated with black arrows. Scale bar = 20 nm. **(B)** Representative particle picks of FocA that went into the 2D classification. Scale bar = 10 nm and accounts for panel B and C. **(C)** Representative 2D classes of negatively stained FocA. Denoted below is the number of particles that went into the classification of the respective class. Annotated with red arrows are visible monomers.

In order to obtain the complete structure of the pore of FocA, including the identification of all amino acid residues lining the pore, an enriched sample that was used in NS-EM was prepared. This sample was subsequently vitrified and imaged with cryo-EM. In total 3665 micrographs were collected which were used for subsequent image processing steps. A representative micrograph of vitrified FocA can be seen in Figure 11.

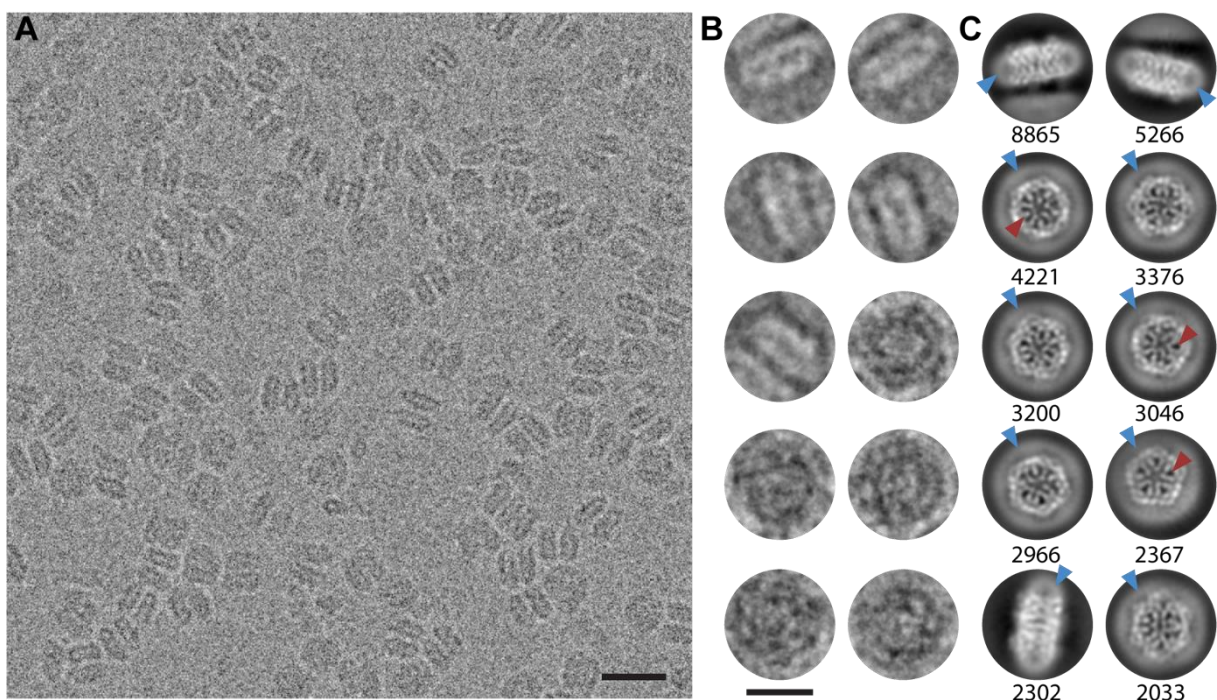


Figure 11: Micrograph, picked particles and 2D classification of vitrified FocA. **(A)** Representative micrograph of vitrified FocA. The micrograph reveals top, bottom, and side views of FocA. Scale bar = 20 nm. **(B)** Representative particle picks of FocA that went into the 2D classification. Scale bar = 10 nm and accounts for panel B and C. **(C)** Representative 2D classes of FocA. Denoted below is the number of particles that went into the classification of the respective class. Surrounding detergent densities are indicated by blue arrows and structural features are indicated by red arrows.

Unlike in the micrograph of negative stained FocA, no preferential orientation could be observed. After particle picking (Figure 11B) and 2D classification, an inspection of the individual 2D classes (Figure 11C) verified the initially observed pentameric assembly of FocA. There high-resolution structural features were retrieved. Additionally, surrounding the particles, a diffuse density attributed to DDM used to extract and stabilize the membrane protein FocA was observed.

The final FocA cryo-EM reconstruction included 192440 single-particles, which were obtained from refined 2D class averages, and had a resolution of ~ 3.1 Å (Figure 12A) (Fourier shell correlation, FSC=0.143, Figure S4). The 3D reconstruction verified the initial observation, of both NS- and cryo-EM 2D class averages, displaying the pentameric assembly of the FocA. The *N*-terminus (residues 1-7) of each protomer was flexible, with the first clearly resolved residue being D8, located at the cytoplasmic side of the central pore of each protomer (Figure 12A). A comparison with the previously resolved crystal structure of the *Escherichia coli* (*E. coli*) FocA channel, which lacks the first 21 *N*-terminal amino acid residues, reveals specific, large-scale rearrangements (Figure 12A, B). The missing *N*-terminus is clearly resolved (Figure 12C), and now assembles the complete cytoplasmic-exposed vestibule. This allowed for the assignment of all relevant amino acid residues that form both the vestibule and the central hydrophobic core of the pore.

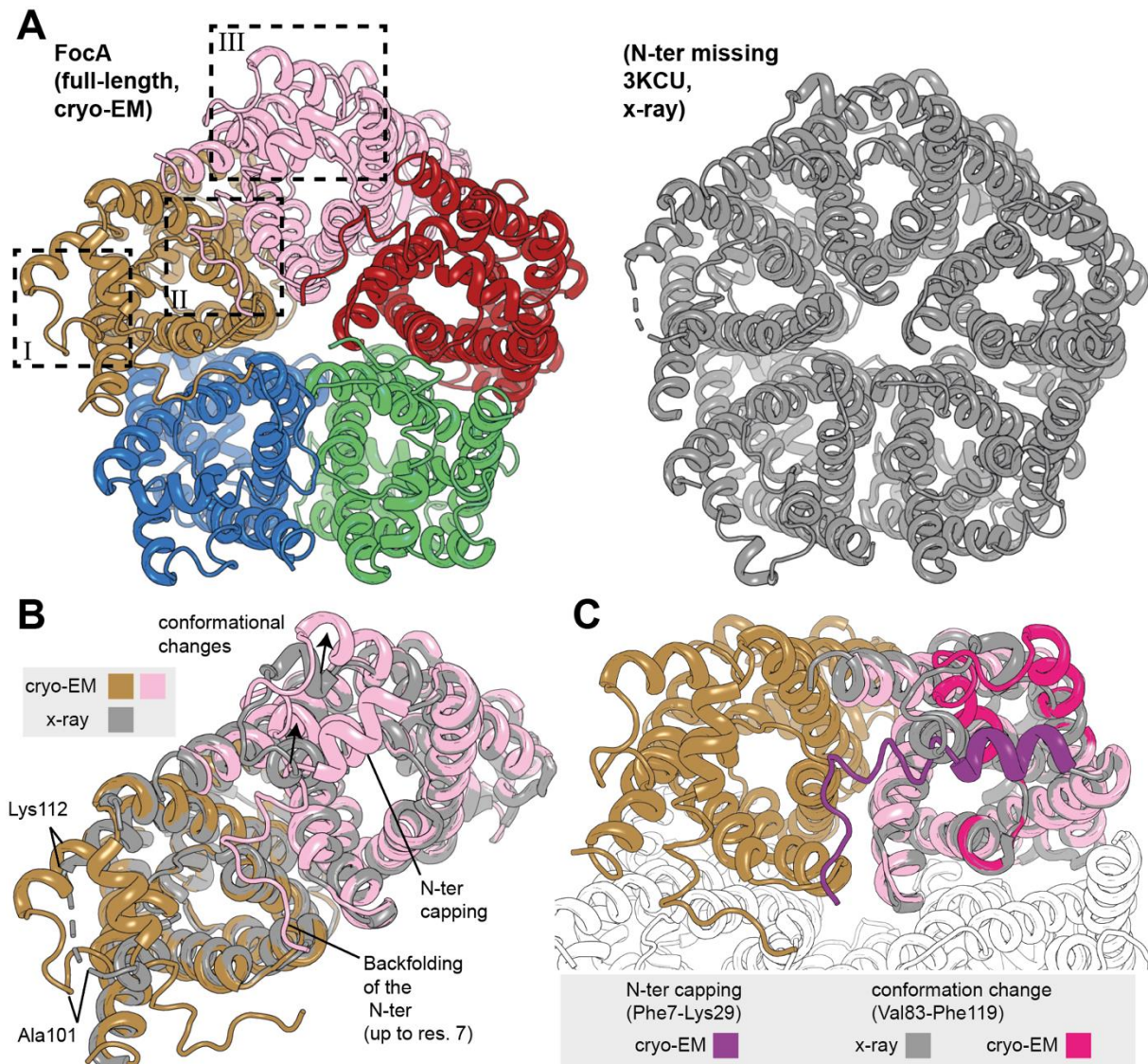


Figure 12: Cryo-EM model of FocA channel resolved to 3.1 Å. The structure is compared with the previously resolved FocA channel from *E. coli* lacking the N-terminal helix (residues 1–21).²⁰⁶ **(A)** The overall architecture shows that both structures are highly similar, and are composed of 5 protomers. Localized changes are highlighted inside the dashed squares and labelled I, II and III. **(B)** Annotation of conformational changes observed for the cryo-EM-resolved structure compared to the X-ray-derived counterpart (PDB ID 3KCU).²⁰⁶ **(C)** N-terminal capping of the cytoplasmic portion of the channel and the structural changes induced by the presence of this structural element (V83–F119 segment) are highlighted.

Furthermore, densities stemming from the detergent micelles were observed in proximity to the outer surfaces of the transmembrane helices (Figure 13A, colored in purple). In general, the low resolution of the detergents can be attributed to their flexibility, averaging of the particles and/or non-specific interactions with the hydrophobic moieties of FocA. Interestingly, the central core on the extracellular side of the pentamer contained five tube-like electron densities, which turned out to be DDM detergent densities (Figure 13B, C). These detergent densities, presumably, contribute to the stabilization of the pentameric complex, as previously observed by

Wang *et al.*²⁰⁶ In a cellular complex, these detergent molecules are most-likely exchanged for lipid molecules that stabilize or even aid in governing the higher-order assembly.

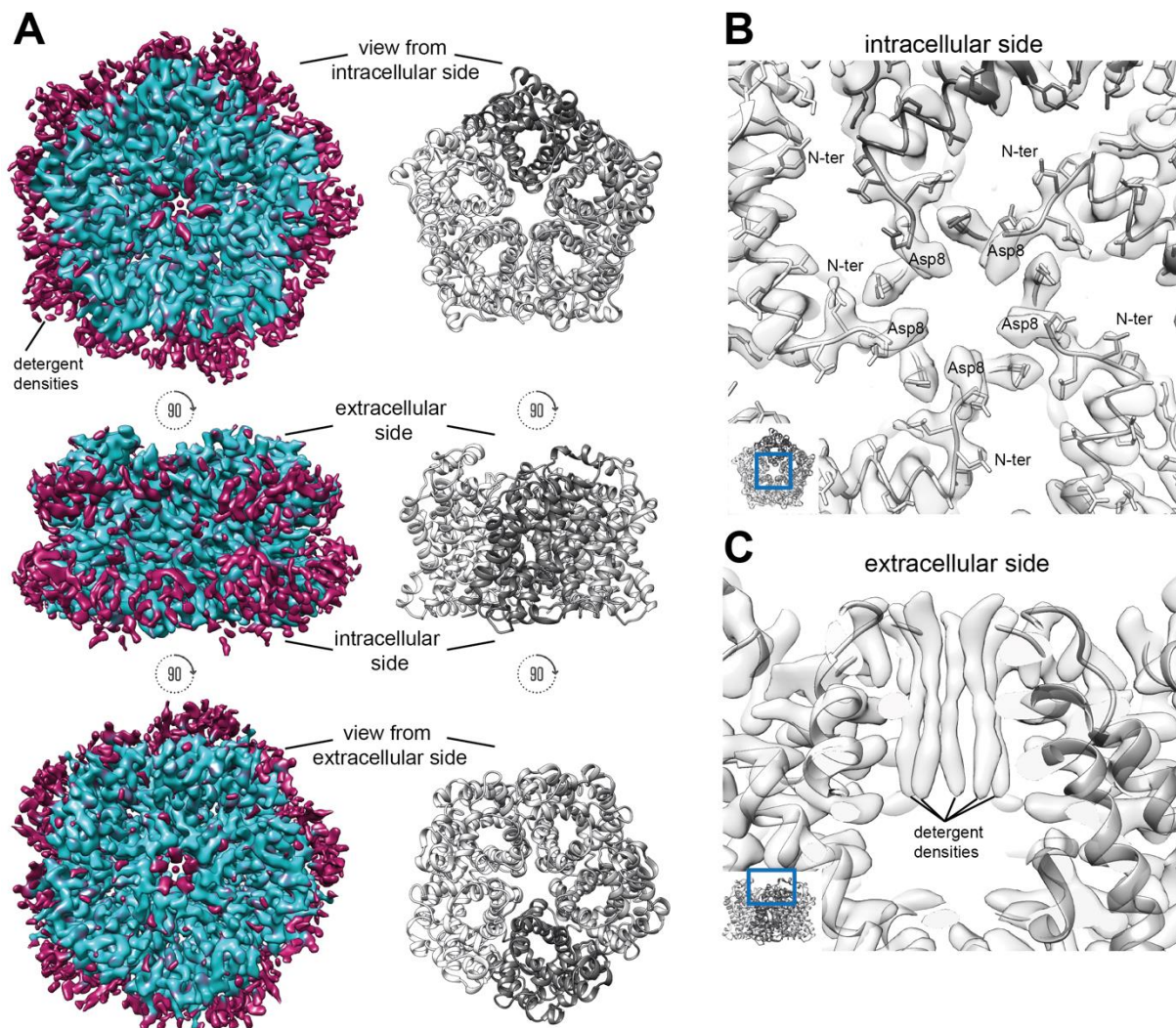


Figure 13 Cryo-EM map of the FocA channel resolved to 3.1 Å with highlighted detergent densities. (A) The channel (shown in cyan, with the adjacent atomic model shown in grayscale) is surrounded by low-resolution densities (shown in magenta). The structure reveals a pentamer and each monomer is color-coded in a step-wise grayscale gradient (from white to gray). (B) On the cytoplasmic (intracellular) side of the channel, density appears at a lower resolution for the initial 7 N-terminal amino acid residues, and the high-quality model building begins from residue D8. (C) The densities of five detergent molecules are clearly resolved at the periplasmic (extracellular) side of the channel and are localized at the centre of the pentameric complex.

Resolving the complete FocA structure reveals that H209 resides centrally within the membrane interface (Figure 14A), its *pros*-nitrogen (N-1) faces the pore and is tightly packed with its surrounding amino acids. It establishes non-covalent van der Waals interactions with vicinal residues within the core of the pore (Figure 14B). These include interactions between H209 and N262 ($d_{vdw} = 2.9 \text{ \AA}$), but also with F202 ($d_{vdw} = 3.3 \text{ \AA}$), I45 ($d_{vdw} = 3.5 \text{ \AA}$), V175 ($d_{vdw} = 3.6 \text{ \AA}$), T91 and A212 ($d_{vdw} = 4.0 \text{ \AA}$, with

the closest atom-atom distance being 2.4 Å). Interestingly, a network of π - π stacks is also observed between F75, F202, and H209 (Figure 14C). H209 is further stabilized by a hydrogen-bond between its main-chain oxygen atom and the nitrogen of N262 ($d_{hb} = 3.0$ Å). This interaction network highlights an extensive, localized polar environment around H209, manifested by the vicinal polar T91, the extended van der Waals interactions and the π - π stacking.

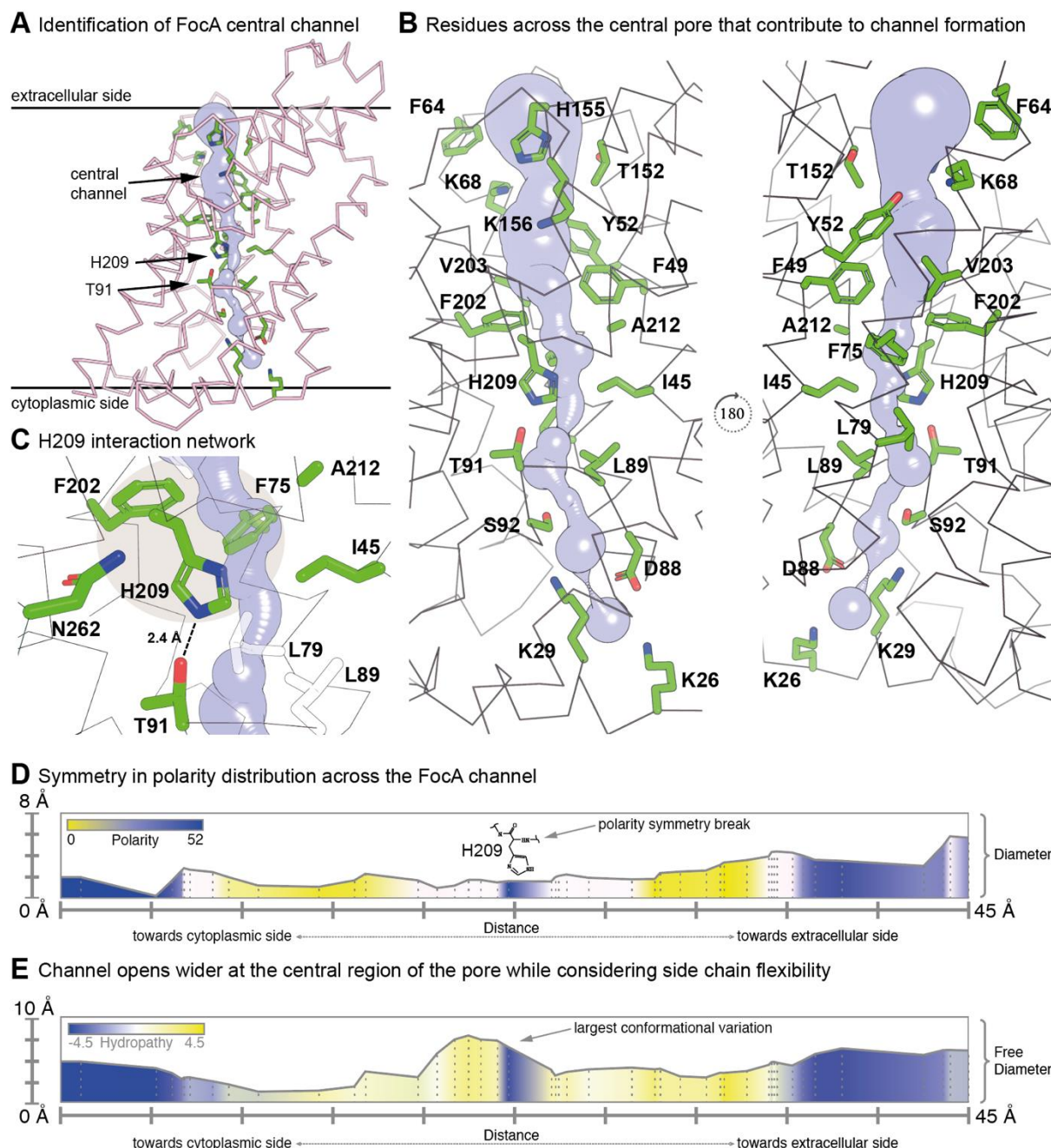


Figure 14: Identification and characterization of the complete FocA channel. (A) Calculated pore within a FocA protomer. Extracellular and cytoplasmic sides are indicated, as well as the central channel, and key residues at the core of the pore are shown. (B) Detailed view of the residues structuring the pore, with the lower portion of the figure depicting the cytoplasmic side, and the upper portion showing the periplasmic side, of the channel. FocA is illustrated in ribbon representation and residues in stick representation show only the side chains of these residues. (C) The local non-covalent interaction network maintained by H209

(see text) is revealed. **(D)** Calculated polarity across the channel (x axis shows the pore length in Å) with the diameter as function of channel length/position (y axis in Å). Diameter is calculated after multiplying the radius of a sphere within channel by 2 and is limited by the three closest atoms. **(E)** Calculated hydrophathy across the channel (x axis shows pore length in Å) with the diameter as function of channel length/position (y axis in Å). The free diameter is calculated in a similar way to D, but a sphere radius within the channel that is limited by the three closest main-chain atoms is taken into account to allow side-chain flexibility.

The structure determination allowed calculation of the polarity and hydrophathy of the protomer's pore (Figure 14D, E), including the unambiguous annotation of all residues structuring the pore and its vestibules (Figure 14B). It is notable that both vestibules have a high density of positive charges with the two lysines, K26 and K29, in the cytoplasmic vestibule being clearly defined, both of which face inwards (Figure 14B). The conserved K156 has a prominent location at the boundary of the periplasmic vestibule and hydrophobic core (Figure 14B), in agreement with its suggested role in electrostatic attraction of formate.^{207,233} As expected, the hydrophobic pore is narrow and is in its presumed closed conformation (Figure 14B, C), with the Ω -loop, including T91²⁰⁵, close to H209. Calculation of known polarity values for amino acids reveals a symmetrical polarity distribution across the pore, including the vestibules and constriction sites (Figure 14D). The channel is highly polar on its rims, and at equidistance from the periplasmic and cytoplasmic rim regions; however, polarity decreases to a depth of ~20 Å within the central pore around H209 (Figure 14D). This region of high polarity disrupts the otherwise non-polar pore, and is promoted by H209 (Figure 14D). Protonation of H209 will alter the charge-balance further, leading to an electrostatic potential that could play a role in the efflux directionality of the channel.

Calculation of the pore diameter using a sphere radius limited by the three closest main-chain atoms, and taking into account side-chain flexibility, reveals that the overall pore diameter increases, across the channel, but not proportionally (Figure 14E). The largest conformational changes are expected to occur in the core of the channel towards the vestibules (Figure 14E), where H209 and its network of interacting residues, including T91 and N262, are present (Figure 14C). This potentially extensive conformational flexibility within the channel would allow increased side-chain dynamics and, therefore, increased plasticity in the non-covalent forces organized by H209. It should also be considered that acidification of the periplasm might influence protonation of the periplasmic rim residues, allowing a charge-transfer along the hydrophobic helix due to a macro-dipole effect²³⁴, which could result in protonation of H209. Taken together, the central location of H209 within the pore, coupled with

protonation of the imidazole side-chain and inherent increase in polarity, would introduce an asymmetric electrostatic funnel for anion attraction. It is therefore conceivable that a protonation/deprotonation switch could play an important role in the directionality of the formate translocation across the pore, augmented by local conformational changes within the channel's pore and vestibules.^{235,236} Moreover, these conformational changes could further be facilitated upon the interaction of the N-terminal helix of FocA with pyruvate formate lyase, which is also essential for the bidirectional passage of formate through FocA and could provide additional conformational constraints to help impose the directionality of the anion transport.²³⁶ However, the precise mechanism, concerning how the directionality of anion transport is gated still remains elusive and further experiments are required.

The here shown structural investigation of a detergent-solubilized membrane protein highlights cryo-EM as a powerful tool in the research field of membrane proteins. However, the interaction of detergents in the inner core of the pentameric assembly of FocA, points out concerns for detergents as a membrane mimetic system. Here, detergent monomers stabilize the higher-order assembly of the FocA pentamer while they also displace phospholipids.²⁰⁶ Nevertheless, multiple studies reported a detrimental outcome while using detergents as a membrane mimetic system to stabilize membrane proteins.

4.2 Detergent-free membrane mimetic systems: Protein-free and protein-containing polymer-bound nanodiscs

In chapter 4.1 a membrane protein—isolated and stabilized with the help of detergents—was structurally investigated. There, unspecific hydrophobic interactions of DDM (Figure 13) in the pentameric assembly of FocA were observed. As mentioned above, lipids are present instead of detergents in a cellular context.⁶⁷ Several studies have shown how the removal of the structural and annular lipids, and their replacement by detergents, can be detrimental to the membrane protein structure and function.^{71,76,237} Additionally, in a pharmacological context a distortion of the structure can hamper the development of potential inhibitors against these proteins, making the initial process of drug development more difficult.¹¹⁷ These flaws urge for a more conserving approach to membrane protein isolation, one that preserves structurally

important lipids around the membrane protein during solubilization and purification, facilitating the investigation of membrane proteins in a more close-to-native state.

4.2.1 Protein-free polymer-bound nanodiscs

Over the recent years, numerous studies described the use of amphiphilic polymers instead of detergents to solubilize artificial and cellular membranes.⁹⁴ These studies investigated how the charge, and phase state of the polymer through changes in its backbone and side chain affect the solubilization.^{128,131,238} However, not just the polymer properties affect the solubilization, but also the properties of the lipids and the lipid composition, ion concentration in the buffer, and the pH.^{96,239} Only recently, polymers with zwitterionic and hydrophobic side chains revealed improved solubilization properties in contrast to the polymers SMA(2:1) and DIBMA.^{126,131} Solubilization of membranes by polymers is not fully understood, but models have been proposed to explain the mechanism.^{98,240} Especially, lipids such as cardiolipin pose, due to its effect on the flexibility and mobility in the lipid bilayer, a difficulty for conventional polymers such as SMA(2:1) and DIBMA to solubilize.^{241,242} In the following chapter, artificial model membranes that mimic the native inner mitochondrial membrane of pig hearts²⁴³ and *Saccharomyces cerevisiae*²⁴⁴ as well as the native membrane of the thermophilic fungus *Myceliophthora thermophila*²⁴⁵—as analogue for *C. thermophilum* membranes—were prepared, solubilized, and analyzed to understand the factors influencing the solubilization behavior of polymers.

4.2.1.1 Multi-component lipid vesicles

First, vesicles from an artificial inner mitochondrial lipid mixture (IMLM) that mimic the inner mitochondrial lipid composition of pig hearts were prepared (Table 6).^{243,246} The lipids for these compositions were obtained from natural sources, thus, the obtained lipids varied in their acyl chain length (C16–C20) and in their degree of saturation (C18:1, C18:2, and 20:4 (Figure S2, Table S1)). Moreover, pig heart IMLM vesicles were prepared in multiple compositions: without cardiolipin (CL) (IMLM) and with CL (IMLM_{CL}), with phosphatidylglycerol (PG), as a substitute for CL, (IMLM_{PG}), and a neutral variant, without the negatively charged lipids PG, CL, and phosphatidylinositol (PI) (IMLM_{neut.}) (Table 6). These different mixtures were used to investigate the effect of lipid charge and shape on the solubilization efficiency of various polymers.

Table 6: Lipid headgroup distribution of pig heart inner mitochondrial membranes²⁴³ and IMLM artificial inner mitochondrial lipid mixtures.^{a, †}

Lipid headgroup	Pig heart inner mitochondrial membrane ^b		IMLM _{CL}	IMLM _{PG}	IMLM	IMLM _{neut.}
PC	26.5	Heart-PC	28.0	17.65	38.35	41.2
PE	38.0	Heart-PE	40.0	25.2	54.8	58.8
PI	3.4	Liver-PI	5.0	3.15	6.85	-
CL/PA	25.4	Heart-CL	27.0	Soy-PG: 54.0	-	-

^a all values are given in mol%

^b Includes 2% Lyso-PC/PE and 4.7% unknown components

Additionally, vesicles that mimic the inner mitochondrial lipid composition of *S. cerevisiae*²⁴⁴, were prepared (Table 7). Different organism-specific mitochondrial membranes were used to investigate a potential difference in the solubilization efficiency. Even though both compositions mimic the same organelle their composition differs. IMLM_{yeast} has compared to IMLM a higher content of PC a decreased amount of CL and PE but an increased amount of PI and furthermore contains PS.

Table 7: Lipid headgroup distribution of *S. cerevisiae* inner mitochondrial membranes²⁴⁴ and IMLM_{yeast} artificial inner mitochondrial lipid mixture.^{a, †}

Lipid headgroup	<i>S. cerevisiae</i> inner mitochondrial membranes		IMLM _{yeast}
PC	38.4	POPC	38.0
PE	24.0	POPE	24.0
PI	16.2	POPI	16.0
PS	3.8	POPS	4.0
CL/PA	17.6	CL	18.0

^a all values are given in mol%

In general, the shape of the vesicles that are formed by a lipid composition depends on the packing properties of the lipids (cf. chapter 1.1.1). In their unsaturated state and with their relatively large headgroup, PC, PG, and PI have a packaging parameter of ~1 indicating a cylindrical shape (Figure 2), thus favoring the formation of large vesicles with a low curvature or flat bilayer sheets.³⁴ Whereas, PE and CL with unsaturated lipids have a $P < 1$ indicating the shape of an inverted truncated cone (Figure 2A) and thus are preferentially located in the inner bilayer leaflet of highly curved vesicles.³⁴ Furthermore, at high concentrations PE favors the formation of multilamellar vesicles, due to its zwitterionic headgroup being capable to be donor- and acceptor, allowing for intra- and intermolecular hydrogen bonds between the bilayers.²⁴⁷ On the contrary, due to the high negative charge, which is present in the IMLM membranes, the electrostatic

[†]Adapted with permission from Pu.3 (cf. chapter 10), Copyright 2023 Elsevier.

repulsion, between the bilayers, would repel each other, thus preventing the formation of multilamellar vesicles. Thus, a high amount of negatively charged lipids (CL and PI) as well as zwitterionic lipids are present, a coexistence of uni- and multilamellar vesicles is expected. Figure 15 depicts cryo-EM micrographs of extruded IMLM vesicles. The diameter of the vesicles were ranging from 80–200 nm and no preference for uni- or multilamellar vesicles was observed, as expected. A closer inspection of the morphology of the vesicles revealed smooth spherical vesicles without any facets, suggesting that the vesicles are in the liquid-crystalline state.²⁴⁸ Additionally, the size distribution of the vesicles was probed by DLS (Figure 15F). Their hydrodynamic diameter was (162 ± 3) nm for IMLM_{CL}, (170 ± 10) nm for (IMLM_{PG}), (158 ± 10) nm for IMLM, (156 ± 5) nm IMLM_{neut.}, and (135 ± 35) nm for IMLM_{yeast}. Even though the vesicles were extruded through a 100 nm polycarbonate membrane, their diameter was considerably larger than the utilized membrane. The larger size of the vesicles might be due to the lipid composition, as e.g., ~33% of lipids from IMLM_{CL} and ~75% from IMLM_{PG} have *P* values being equal or close to ~1, thus favoring a low curvature. Therefore, during extrusion vesicles are deformed but maintain their large diameter.³⁴

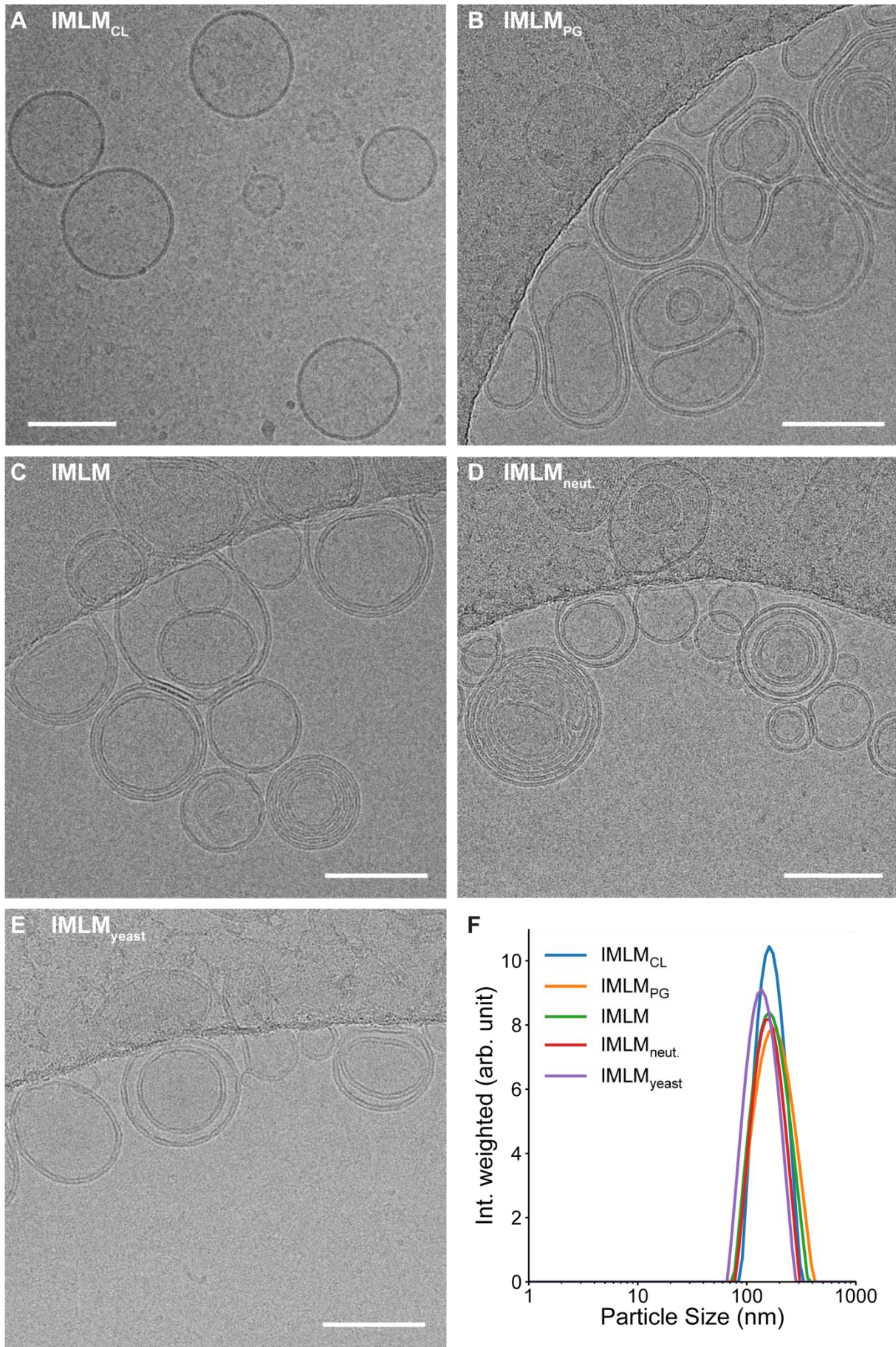


Figure 15: Artificial vesicles mimicking the inner mitochondrial lipid composition of pig heart and *S. cerevisiae*. Cryo-EM micrographs of (A) IMLM_{CL}, (B) IMLM_{PG}, (C) IMLM,

(D) IMLM_{neut.}, and (E) IMLM_{yeast} vesicles. Scale bar = 100 nm. (F) DLS intensity-weighted size distribution of IMLM_{CL}, IMLM_{PG}, IMLM, IMLM_{neut.}, and IMLM_{yeast} vesicles.[†]

As the model organism used in this thesis, *C. thermophilum*, is a thermophilic fungus, and thermophilic organisms have a considerably different chemical composition compared to their mesophilic counterparts, vesicles mimicking the membrane composition of a thermophilic fungus, here *M. thermophila*²⁴⁵, a thermophilic fungus lipid mixture (TFLM) was prepared (Table 8).

Table 8 Lipid headgroup distribution of the *M. thermophila*²⁴⁵ membranes and TFLM artificial thermophilic fungus lipid mixture.^{a, †}

Lipid headgroup	<i>M. thermophila</i> membranes		TFLM
PC	14.0	16:0-18:2 PC	15.0
PE	13.0	16:0-18:1 PE	14.0
PA	25.0	16:0-18:2 PA	27.0
CL	13.0	Heart-CL	14
ERG	27.0	Ergosterol	30.0

^a all values are given in mol%

Recent studies found a high phosphatidic acid and ergosterol (ERG) content in membranes of thermophilic fungi, which is further upregulated as a response to heat stress, while downregulating PC and PE contents.²⁴⁵ Due to the increased amount of phosphatidic acid the membranes possess a higher negative charge than the IMLM membranes, however, due to ~30% of zwitterionic lipids (PC/PE) the coexistence of uni- and multilamellar vesicles is expected. Figure 16 depicts cryo-EM micrographs of TFLM vesicles and DLS data.

[†]Adapted with permission from Pu.3 (cf. chapter 10), Copyright 2023 Elsevier.

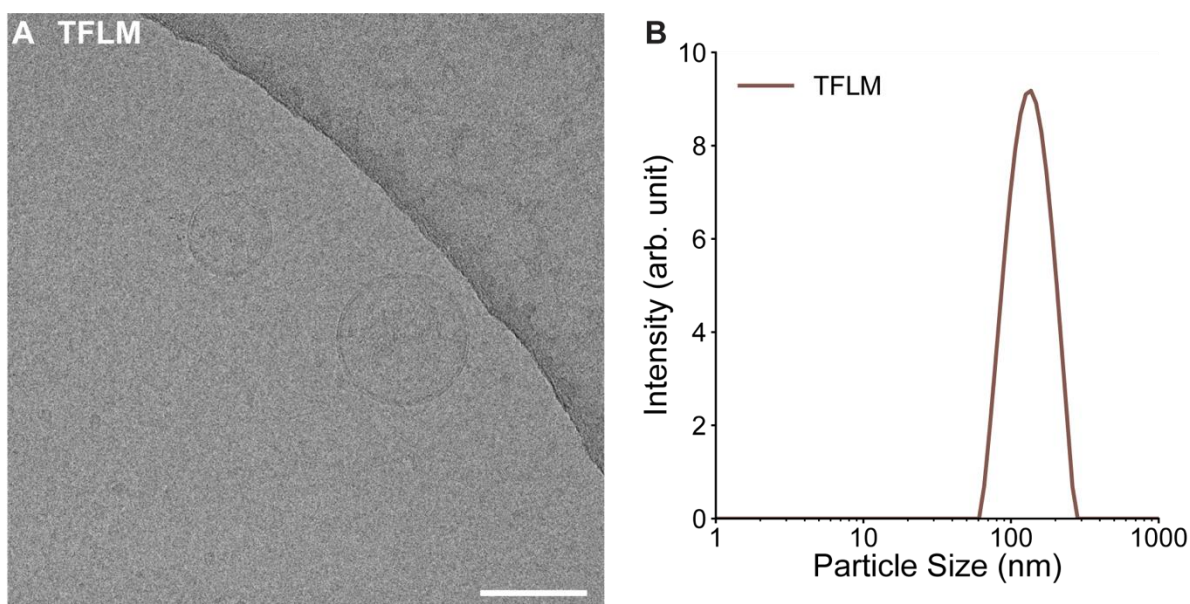


Figure 16: Artificial TFLM vesicles mimicking thermophilic fungus lipid mixture of *M. thermophila*.²⁴⁵ (A) Cryo-EM micrograph of TFLM vesicles. Scale bar = 100 nm. (B) Intensity-weighted particle size distribution of TFLM vesicles.[†]

In the cryo-EM micrographs the majority of observed vesicles were unilamellar and were ranging from 90–150 nm; however, due to the size of the acquired dataset, a clear preference for uni- over multilamellar vesicles could not be identified. The hydrodynamic diameter of the TFLM vesicles was (135 ± 40) nm and is in a good agreement with the observed sizes through cryo-EM. However, the size of the vesicles is considerably larger than the size of the membrane pores that were used for extrusion (100 nm). This might be explained by the same phenomenon that was described above that the larger diameter of the TFLM vesicles is due to 30% of lipids possessing a P value being close or equal to ~ 1 , thus favoring a low curvature and therefore larger vesicles.³⁴ Additionally, the observed TFLM vesicles showed smooth spherical surface without any facets, suggesting that these vesicles are also in the liquid-crystalline state. The results presented above, showed that the lipid mixtures successfully self-assembled into vesicles in the liquid-crystalline state and are amenable to be used for solubilization experiments to form lipid-bilayer nanodiscs.

4.2.1.2 Solubilization and characterization of multi-component lipid vesicles

4.2.1.2.1 Solubilization of vesicles mimicking pig heart inner mitochondrial membranes by diisobutylene/maleic acid

The ability to solubilize the prepared IMLM vesicles, which mimic the lipid composition of pig heart inner mitochondrial membranes, by polymers, was first tested with the

[†]Adapted with permission from Pu.1 (cf. chapter 10), Copyright 2023 American Chemical Society.

polymer DIBMA. To this extent, IMLM_{CL}, IMLM_{PG}, IMLM, and IMLM_{neut} vesicles were subjected to increasing concentrations of DIBMA in the presence of 200 mM and 500 mM NaCl. The increased salt concentration was chosen because a previous study showed an improved solubilization yield at a higher ionic strengths.²³⁹ Solubilization was monitored by negative-stain EM (NS-EM) and DLS and is summarized for the mass ratios of polymer to lipid $m_P/m_L = 1.5, 3.5, 5, 7, \text{ and } 10$ in Table 9.

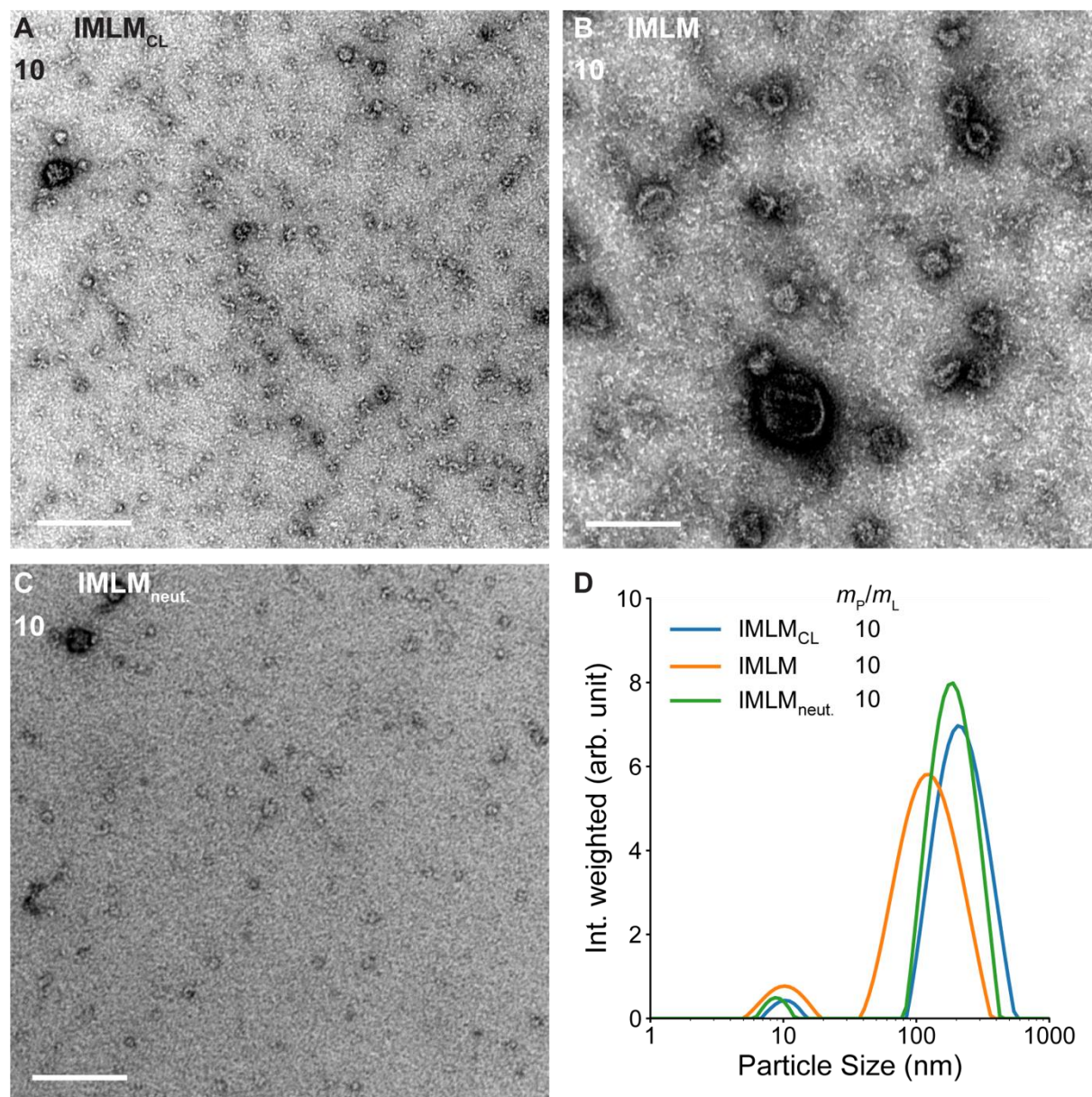


Figure 17: DIBMA-nanodiscs mimicking inner mitochondrial lipid composition of pig heart at 200 mM NaCl. NS-EM micrographs of (A) IMLM_{CL} ($m_P/m_L = 10$), (B) IMLM (10), and (C) IMLM_{neut}. (10). Scale bar = 100 nm. (D) Intensity-weighted size distribution of DIBMA-nanodiscs originating from artificial IMLMs, as obtained from DLS.[†]

[†]Adapted with permission from Pu.3 (cf. chapter 10), Copyright 2023 Elsevier.

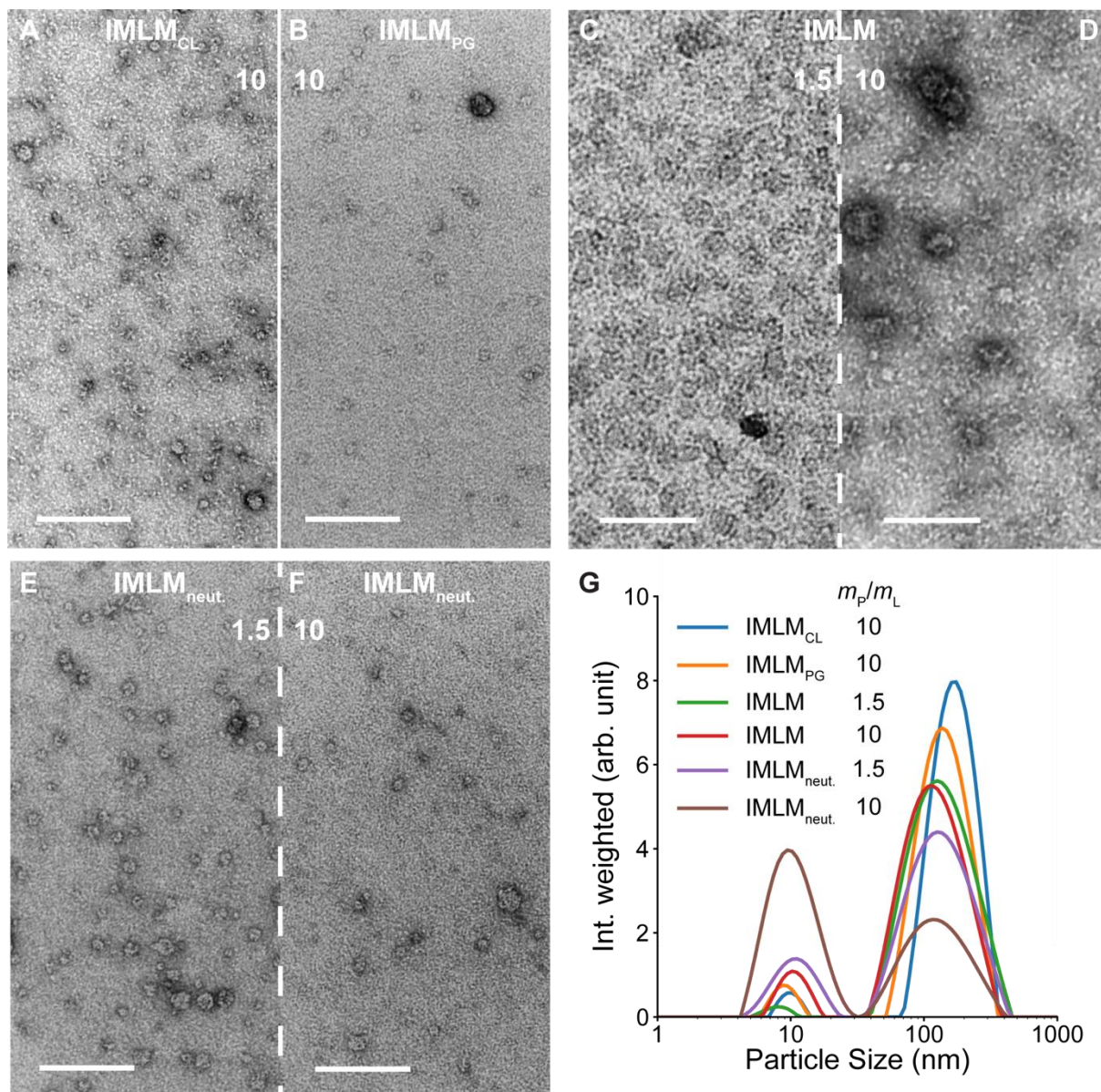


Figure 18 DIBMA-nanodiscs mimicking inner mitochondrial lipid composition of pig heart at 500 mM NaCl. NS-EM micrographs of (A) IMLM_{CL} ($m_P/m_L = 10$), (B) IMLM_{PG} (10), (C, D) IMLM_{neut.} (1.5, 10), (E, F) IMLM_{neut.} (1.5, 10). Scale bar = 100 nm. (G) Intensity-weighted size distribution of DIBMA-nanodiscs originating from artificial IMLMs, as obtained from DLS.[†]

An inspection of the intensity-weighted particle size distributions (Figure 17, Figure 18) reveals multimodal distributions suggesting the coexistence of nanodiscs and vesicles alike in the solubilization experiments. For a better overview the solubilization experiments are summarized in Table 9. Thus, DIBMA was not able to completely solubilize the artificial pig heart vesicles at the tested m_P/m_L . The first peak from the intensity-weighted particle size distributions, corresponding to the smallest particle size, was taken as the hydrodynamic particle diameter. This is justified by the strong dependency of light scattering intensity towards the particle size (cf. chapter 1.3.2), resulting in z-average hydrodynamic diameters between $d_z = (8 \pm 3)$ nm for IMLM_{PG} at $m_P/m_L = 10$ and $d_z = (11 \pm 6)$ nm for IMLM_{neut.} at $m_P/m_L = 1.5$.¹⁴² Interestingly, the size

[†]Adapted with permission from Pu.3 (cf. chapter 10), Copyright 2023 Elsevier.

of the nanodiscs, reported here, are smaller than those reported for DIBMA-solubilized DMPC membranes.²⁴⁹

Table 9: Solubilization of artificial vesicles mimicking inner mitochondrial membrane composition of pig heart with DIBMA at different polymer to lipid mass ratios. Crosses indicate ND formation based on DLS and NS-EM.[†]

Lipid mix m_P/m_L (g/g)	IMLM _{CL}		IMLM _{PG}		IMLM		IMLM _{neut.}	
	c_{NaCl} (mM)							
	200	500	200	500	200	500	200	500
1.5						X		X
3.5						X		X
5						X		X
7						X		X
10	X	X		X	X	X	X	X

This can be attributed to the differences in the lipid composition, notably the use of naturally unsaturated, charged lipids or the use of much higher concentrations of DIBMA. A detailed analysis of the nanodisc size is impaired due to high polydispersity observed in the sample which is caused by residual unsolubilized vesicles. (Figure 17C, D). The observed polydispersity, is reflected in the NS-EM micrographs, showing vesicles as well as nanodiscs (Figure 17C, D).

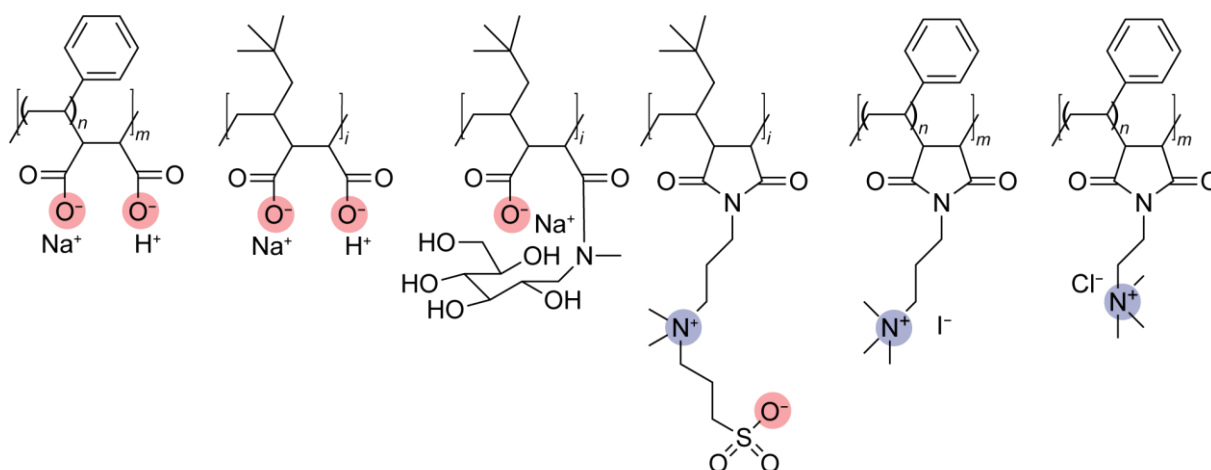
The combined results of DLS and NS-EM show that DIBMA is able to solubilize IMLM_{CL}, IMLM_{PG}, IMLM, and IMLM_{neut.} at 200 mM or 500 mM NaCl. The solubilization of IMLM_{CL}, IMLM, and IMLM_{neut.} at 200 mM NaCl was only observed at high polymer concentrations ($m_P/m_L = 10$). Interestingly, after an exchange of CL (IMLM_{CL}) to PG (IMLM_{PG}) no solubilization was observed at 200 mM NaCl. This changed by increasing the NaCl concentrations to 500 mM. Due to the increase of NaCl concentration, DIBMA was able to solubilize IMLM and IMLM_{neut.} at all investigated m_P/m_L , whereas, IMLM_{PG} and IMLM_{CL} were only solubilized at high polymer concentrations ($m_P/m_L = 10$) (Table 9).^{239,250} The reason why DIBMA was able to solubilize the negative lipid mixtures at high polymer concentrations is complex and depends on a multitude of factors.²³⁹ For IMLM_{CL} all lipids possess a great amount of poly-unsaturated acyl chains (Table S1) that interfere with the solubilization process, as they increase lateral pressure of the membrane. Additionally, the lipids PE and CL possess an intrinsic negative curvature, further increasing the lateral pressure of the membrane.²⁵⁰ The increase in lateral pressure makes it difficult for DIBMA to insert into the membrane, thus affecting the solubilization.^{240,251} Further, the charge of the anionic lipids CL and PI cause electrostatic repulsion, repelling the negatively charged polymer DIBMA (cf. chapter 1.2.2), thus decreasing the efficiency and rate of solubilization.

[†]Adapted with permission from Pu.3 (cf. chapter 10), Copyright 2023 Elsevier.

Interestingly, Scheidelaar *et al.* reported a similar observation with the harsher polymer SMA(2:1).²⁴⁰ There, difficulties were reported for the solubilization of vesicles that are composed of a total polar lipid extract, composed of PE, PG, and CL. The results of the solubilization of IMLM_{CL} vesicles at high m_P/m_L , highlights the lipid shape and saturation as important factors during solubilization, even at low and high levels of coulombic screening. As mentioned above an exchange of CL to PG led to the result that DIBMA could not solubilize IMLM_{PG} vesicles at 200 mM NaCl and only at $m_P/m_L = 10$ at 500 mM NaCl (Table 9, Figure 17). A plausible explanation could be the lipid distribution inside the membrane, as the preferential location of CL is the inner bilayer leaflet, whereas PG is equally distributed.²⁴⁷ This results in a higher surface charge of IMLM_{PG} vesicles, thus require a higher salt concentration to screen the charges to allow for solubilization of vesicles. Vesicles that have no CL content, such as IMLM and IMLM_{neut.} only 7% or none of the lipids are negatively charged, respectively. These lipid mixtures were solubilized at considerably lower m_P/m_L at 500 mM NaCl, when compared to IMLM_{CL} and IMLM_{PG} (Table 9, Figure 18). However, at 200 mM NaCl a solubilization of IMLM and IMLM_{neut.} is only possible at $m_P/m_L = 10$. In conclusion, the shape of the lipids and their degree of saturation as well as the charge state of the membrane considerably affect the solubilization of membranes and should be carefully taken into consideration.

4.2.1.2.2 Solubilization of pig heart IMLM_{CL} vesicles by polymers of different charge

IMLM_{CL} mimics the lipid composition of pig heart inner mitochondrial membranes the closest, therefore, this lipid composition was used to probe the solubilization efficiency of amphiphilic polymers of different charge. The different polymers that were used can be seen in Figure 19.



SMA (2:1) DIBMA Glyco-DIBMA Sulfo-DIBMA QA1-SMA QA2-SMA

Figure 19: Chemical Structure of amphiphilic polymers used to solubilize vesicles that mimic the lipid composition of pig heart inner mitochondrial membranes. The amphiphilic polymers SMA(2:1), DIBMA, and Glyco-DIBMA have an overall negative charge, whereas Sulfo-DIBMA is of zwitterionic nature and QA1-SMA and QA2-SMA possess an overall positive charge. The red and blue colour, indicate a negative or positive charge, respectively.[†]

SMA(2:1) and DIBMA are the conventional polymers and possess two negative charges per subunit and are commonly used as the basis to derive new polymers.¹²⁸ Glyco-DIBMA is a glycosylated derivative of DIBMA and possess a greater hydrophobicity and a decreased charge density in comparison with DIBMA and SMA(2:1).²³⁸ Sulfo-DIBMA is a zwitterionic derivative of DIBMA with a sulfobetaine group attached to it.¹³¹ Whereas the previous introduced polymers are negatively charged or zwitterionic, QA1-SMA and QA2-SMA are positively charged and are derivatives from styrene maleimide polymers with the addition of a quaternary ammonium to it.²⁵² In order to test the solubilization efficiency of the polymers, each polymer was incubated with IMLM_{CL} vesicles at increasing m_P/m_L ($m_P/m_L = 0.25, 0.5, 1, 1.5, 5, 10$) at 200 mM and 500 mM NaCl. The formation of nanodiscs was monitored by DLS and NS-EM and can be seen in Figure 20 and Figure 21, respectively. As seen in the chapter above (cf. chapter 4.2.1.2), IMLM_{CL} was only solubilized by DIBMA at high m_P/m_L irrespective of the NaCl. An inspection of Table 10 shows a comparable trend for SMA(2:1) with the difference that SMA(2:1) solubilized IMLM_{CL} at $m_P/m_L = 5$ at 500 mM NaCl, which was not observed for DIBMA. In contrast, the positively charged polymers QA1-SMA and QA2-SMA were only able to solubilize IMLM_{CL} at $m_P/m_L = 10$ at 500 mM NaCl. Glyco-DIBMA, independently of the NaCl concentration, was able to solubilize IMLM_{CL} at low $m_P/m_L = 1$. Interestingly, Sulfo-DIBMA showed successful solubilization with 200 mM at $m_P/m_L = 1$ and at 500 mM NaCl at

[†]Adapted with permission from Pu.3 (cf. chapter 10), Copyright 2023 Elsevier.

$m_P/m_L = 0.25$, making Sulfo-DIBMA the polymer with the highest solubilization efficiency.

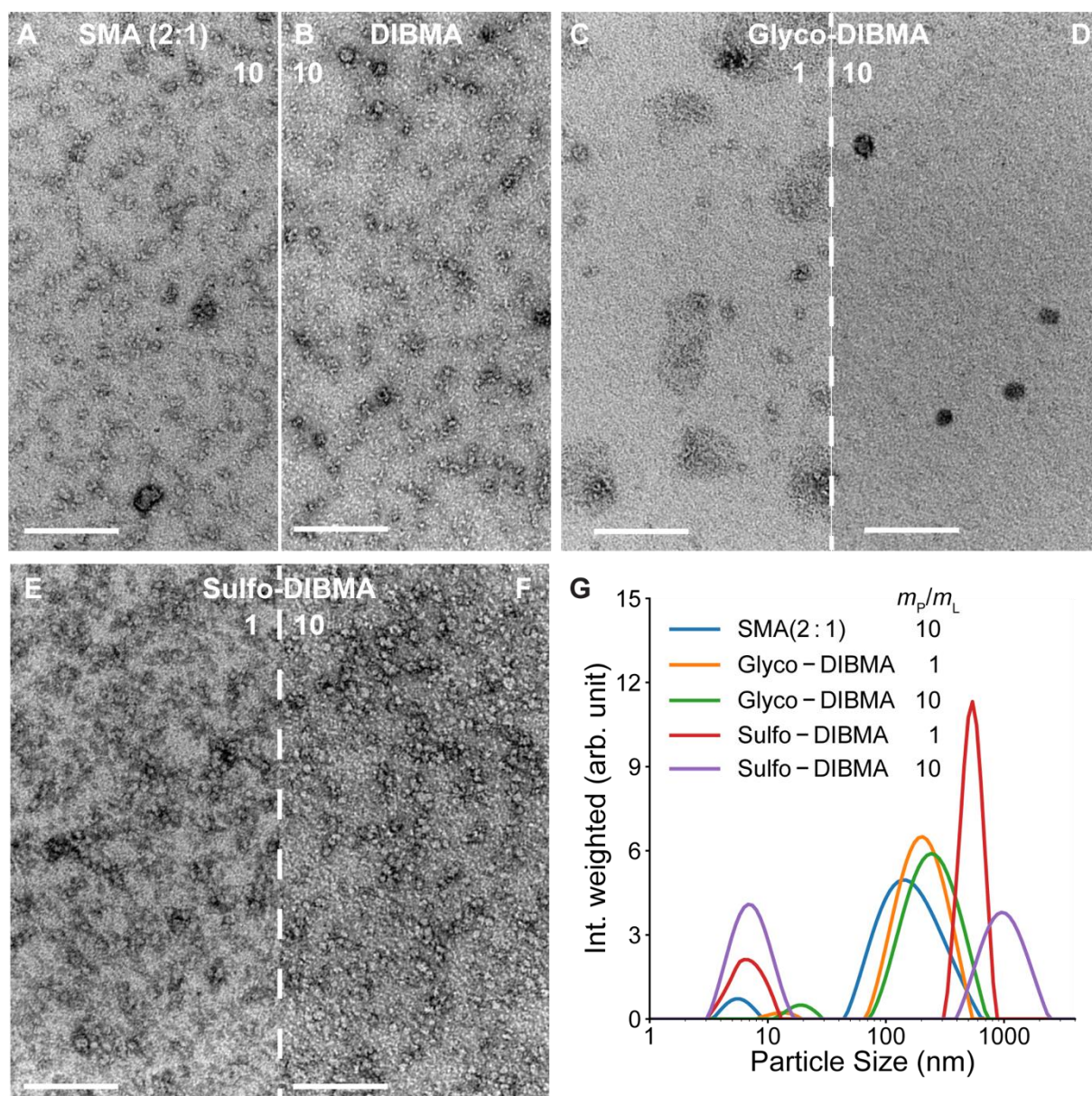


Figure 20: Polymer/IMLM_{CL}-nanodiscs of different charge at 200 mM NaCl. NS-EM micrographs of (A) SMA(2:1) ($m_P/m_L = 10$), (B) DIBMA (10), (C, D) Glyco-DIBMA (1, 10), and (E, F) Sulfo-DIBMA (1, 10). Scale bar = 100 nm. (G) Intensity-weighted size distribution of various polymer/IMLM_{CL}-nanodiscs originating from artificial, as obtained from DLS.[†]

In the samples containing 200 mM NaCl, the intensity-weighted size distribution revealed for the negatively charged polymers SMA(2:1) and DIBMA a $d_z = (6 \pm 3)$ nm and $d_z = (6 \pm 3)$ nm, respectively. Whereas the zwitterionic polymers Glyco-DIBMA showed a $d_z = (13 \pm 5)$ nm up to $d_z = (19 \pm 9)$, depending on the m_P/m_L , and Sulfo-DIBMA showed sizes around $d_z = (7 \pm 3)$ nm.

[†]Adapted with permission from Pu.3 (cf. chapter 10), Copyright 2023 Elsevier.

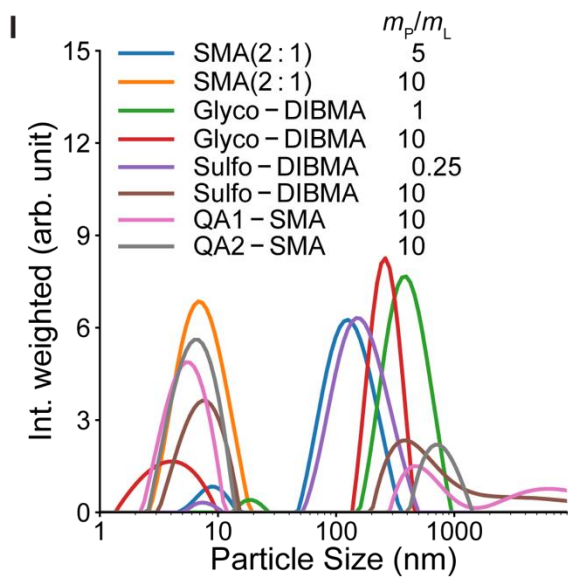
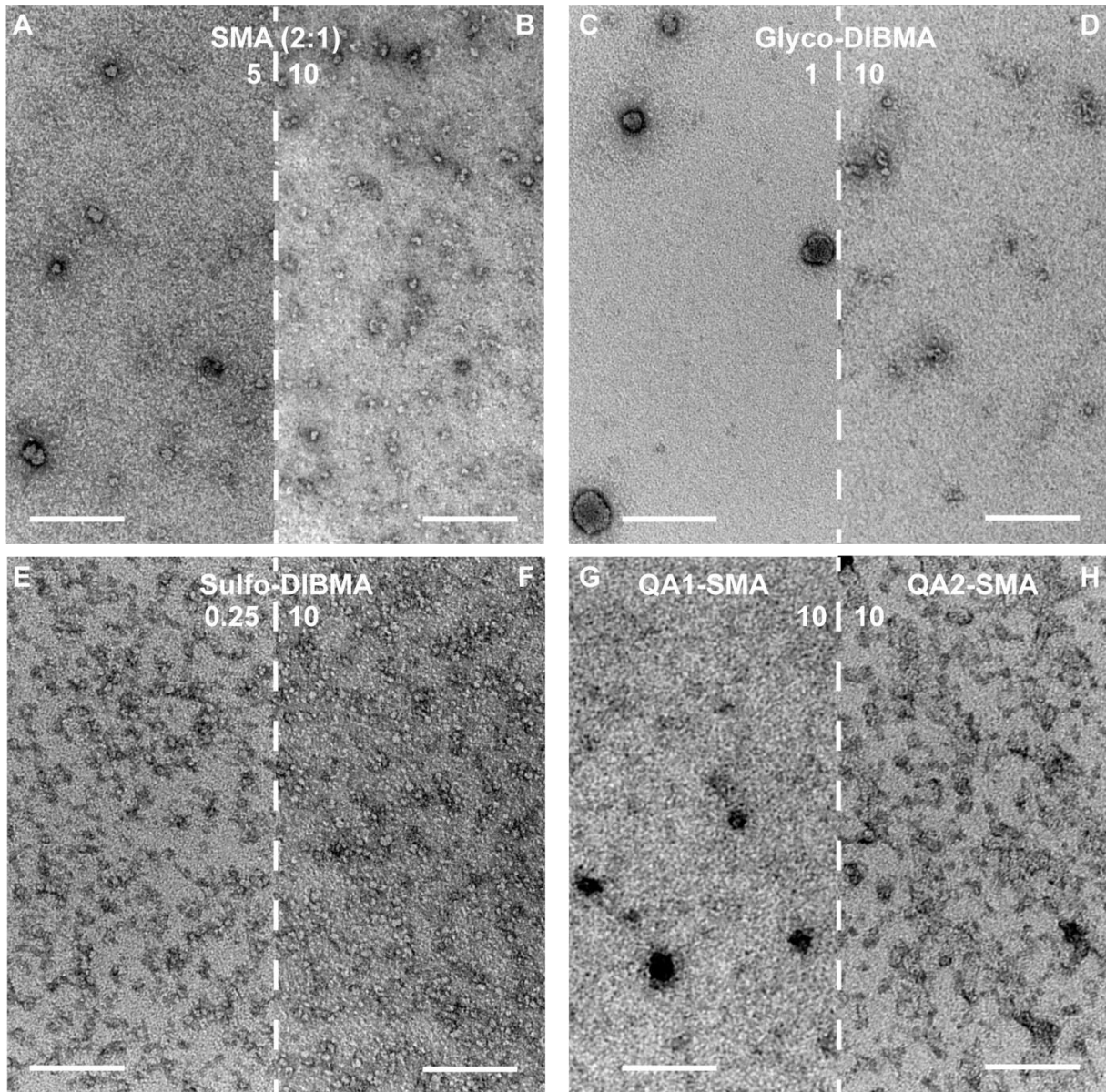


Figure 21: Polymer/IMLM_{CL}-nanodiscs of different charge at 500 mM NaCl. NS-EM micrographs of (A, B) SMA(2:1) ($m_P/m_L = 5, 10$), (C, D) Glyco-DIBMA (1, 10), (E, F) Sulfo-DIBMA (0.25, 10), (G) QA1-SMA (10), and (H) QA2-SMA. Scale bar = 100 nm. (I) Intensity-weighted size distribution of polymer/IMLM_{CL}-nanodiscs, as obtained from DLS.[†]

[†]Adapted with permission from Pu.3 (cf. chapter 10), Copyright 2023 Elsevier.

At 500 mM NaCl the positively charged QA1 and QA2-SMA revealed a size distribution of $d_z = (6 \pm 3)$ nm, whereas the negatively charged DIBMA was between $d_z = (10 \pm 4)$ nm and SMA(2:1) was ranging from $d_z = (9 \pm 4)$ nm to $d_z = (7 \pm 3)$ nm, depending on the m_P/m_L . The results of the solubilization are summarized in Table 10.

Table 10: Solubilization of artificial vesicles mimicking inner mitochondrial membrane composition of pig heart using polymers of various charge at different m_P/m_L . Indicated with a cross are successful nanodisc formations that were observed by NS-EM and DLS.[†]

Polymer	SMA(2:1)		DIBMA		Glyco-DIBMA		Sulfo-DIBMA		QA1-SMA		QA2-SMA	
Polymer subunit charge	-2		-2		-1		0		+1		+1	
m_P/m_L (g/g)	c_{NaCl} (mM)											
	200		500		200		500		200		500	
0.25												X
0.5												X
1					X	X	X	X				
1.5					X	X	X	X				
5			X		X	X	X	X				
10	X	X	X	X	X	X	X	X			X	X

Glyco-DIBMA ranged from $d_z = (19 \pm 6)$ nm to $d_z = (10 \pm 1)$ nm. The successful solubilization by Glyco-DIBMA and Sulfo-DIBMA, at the low m_P/m_L could be explained by their lower or completely absent negative net charge, as this results in a decreased charge related repulsion from the negatively charged IMLM_{CL} membrane to the polymer. Additionally, a closer inspection of the DLS data (Figure 21) revealed the presence of larger particles in all samples, even at high m_P/m_L , indicating that no polymer was able to fully solubilize the IMLM_{CL} vesicles. Owing to the high polydispersity a detailed discussion of the observed sizes is hindered. To complement and confirm the observed hydrodynamic diameters through DLS measurements, a dataset of 660 micrographs from negatively stained Sulfo-DIBMA nanodiscs from IMLM_{CL} vesicles at $m_P/m_L = 1$ was acquired, and quantitatively analyzed through image analysis. Sulfo-DIBMA was chosen as it was the polymer that showed the highest

[†]Adapted with permission from Pu.3 (cf. chapter 10), Copyright 2023 Elsevier.

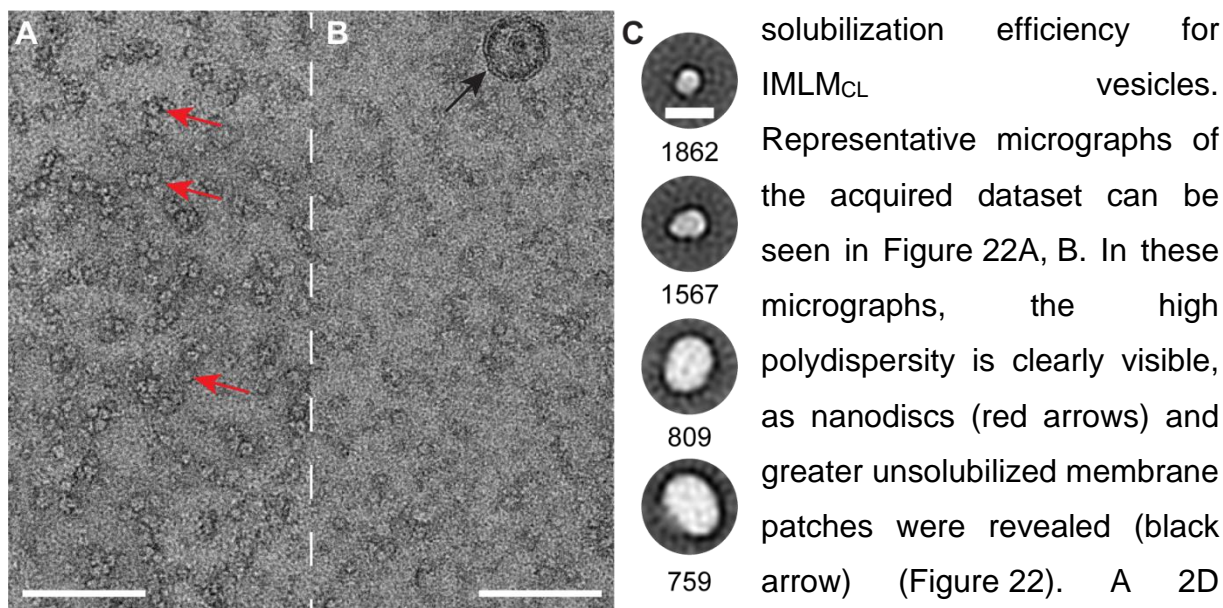


Figure 22: Exemplary NS-EM micrograph and 2D class averages of Sulfo-DIBMA/IMLM_{CL}-nanodiscs. (A, B) Selected NS-EM micrographs from the dataset that was used for the 2D classification and the subsequent statistical size analysis. Indicated by red arrows are nanodiscs and by black arrows unsolubilized membrane patches. Scale bar = 100 nm (C) Representative 2D classes with the number of particles per class denoted below. Scale bar = 10 nm.[†]

solubilization efficiency for vesicles. Representative micrographs of the acquired dataset can be seen in Figure 22A, B. In these micrographs, the high polydispersity is clearly visible, as nanodiscs (red arrows) and greater unsolubilized membrane patches were revealed (black arrow) (Figure 22). A 2D classification of 37623 nanodiscs and the subsequent statistical analysis of those classes, revealed their broad size distribution which was previously measured through

DLS. Representative 2D classes can be seen in Figure 22C (Figure S3). The sizes of the nanodiscs were in a good agreement with the DLS data. Interestingly, due to the higher spatial resolution of the electron microscope, the NS-EM data revealed a bimodal distribution of the nanodiscs at ~8 nm and ~13 nm which was not visible in the DLS data before (Figure 23A). Additionally, it is noteworthy that the NS-EM revealed a not perfectly circular shape of the nanodiscs, shown by measuring their minimal and maximal axis in the 2D classes (Figure 23B). Here, the minimal axis was ~10 nm and the maximum axis ~12 nm.

[†]Adapted with permission from Pu.3 (cf. chapter 10), Copyright 2023 Elsevier.

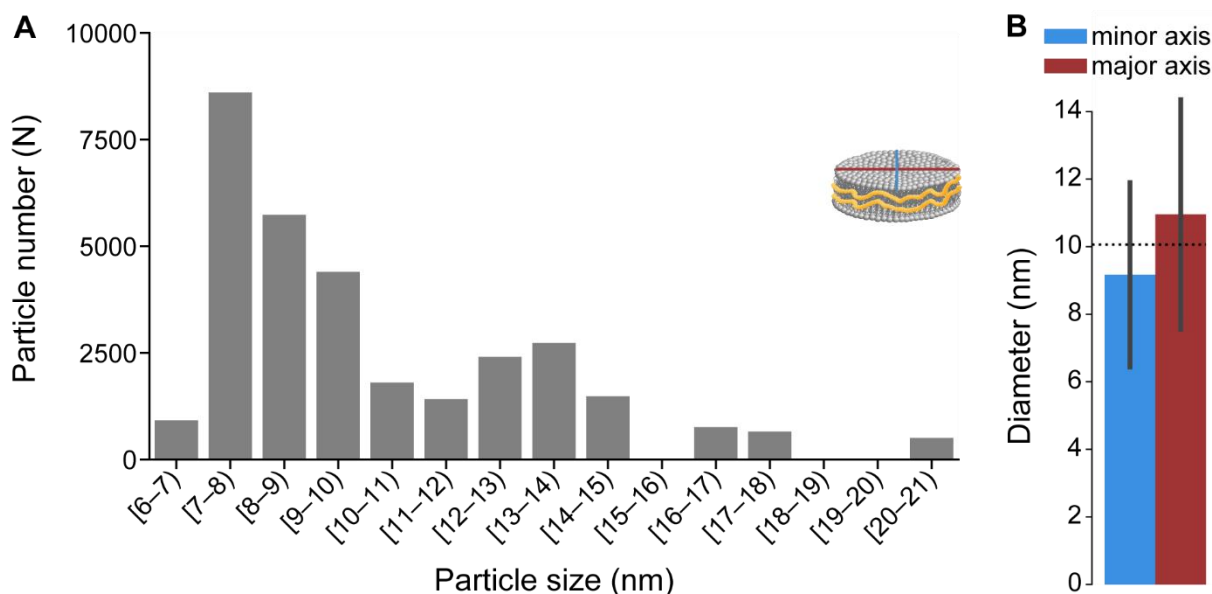


Figure 23: Size distribution of Sulfo-DIBMA nanodiscs from solubilized IMLM_{CL} vesicles. (A) number of particles per binned averaged particle size in nm. Illustrated in the upper right corner is a nanodisc that got annotated with the minor (blue) and major (red) axis, which were measured to calculate the average diameter. (B) Depicted are the weighted average of the minor and major axis of the observed nanodiscs in the 2D classes from NS-EM. The dotted line represents the averaged particle size.[†]

Interestingly, a closer inspection of the 2D classes revealed that nanodiscs with a higher diameter are frequently showing side-by-side interactions between two nanodiscs (Figure 24). The interactions span from long ranged interactions, incidental colocalization of nanodiscs, to short ranged interactions (Figure 24A from left to right, respectively). Such side-by-side interactions have been previously observed for the polymer SMA(2:1).²⁵³

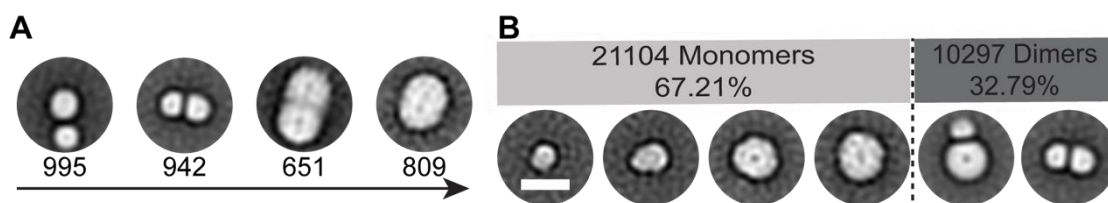


Figure 24: Side-by-side nanodisc interactions and statistical distribution of monomers and dimers. (A) Class averages showing side-by-side nanodisc interactions as function of nanodisc proximity. (B) Distribution of monomers (light gray) and dimers (dark gray) among the 2D classes (83.5% of the 37623 nanodiscs ended up in the analyzed classes). Scale bar = 10 nm.[†]

Additionally, a statistical evaluation of these interactions revealed that these interactions make up >30% of the averaged single particles (Figure 24B). Furthermore, these interacting particles account for a substantial fraction of the larger particles in the bimodal size distribution (Figure 23, Figure 24). The NS-EM data reflected not just the complexity of the whole sample but also the complexity of the nanodiscs, which is not possible by measuring the size distribution by batch methods such as DLS. The here

[†]Adapted with permission from Pu.3 (cf. chapter 10), Copyright 2023 Elsevier.

observed interactions can either be attributed to the incidental co-localization of nanodiscs or, more likely, to the charge neutrality of the zwitterionic polymer. In the case of the latter, it seems reasonable that due to the absence of a negative charge on the polymer and thus the absence of electrostatic repulsive forces, nanodiscs formed by net neutral polymers could interact in such a manner.¹²⁰ Moreover, previous studies of SMA(2:1)- and DIBMA-nanodiscs reported that upon collision with another nanodisc, a rapid exchange of lipid molecules between the nanodiscs was observed. This exchange is facilitated by the flexible nature of the polymer rim of the nanodiscs.^{120,254} The results shown here support previously observed data of the collisional interaction of nanodiscs.²⁵⁴ Further, electron microscopy aided in the clarification of how frequently nanodiscs, with a net neutral charge, can engage in side-by-side interactions.

4.2.1.2.3 Solubilization of IMLM_{yeast} vesicles by DIBMA and SMA(2:1)

The solubilization of vesicles mimicking the inner mitochondrial lipid composition of *S. cerevisiae* was performed to investigate the solubilization behaviour of SMA(2:1) and DIBMA to organism-specific mitochondria. More specifically to investigate the effect of cardiolipin and membranes with a high negative charge towards the solubilization. As mentioned above, the IMLM_{yeast} lipid mixture has less CL but higher contents of PI and additionally contains PS (Table 6, Table 7). Furthermore, the acyl chain lengths and the degree of saturation are different compared to pig heart IMLM. IMLM_{yeast} were solubilized with DIBMA and SMA(2:1). The formation of nanodiscs was monitored by DLS and NS-EM and are illustrated in Figure 25. The results of the solubilization are summarized in Table 11.

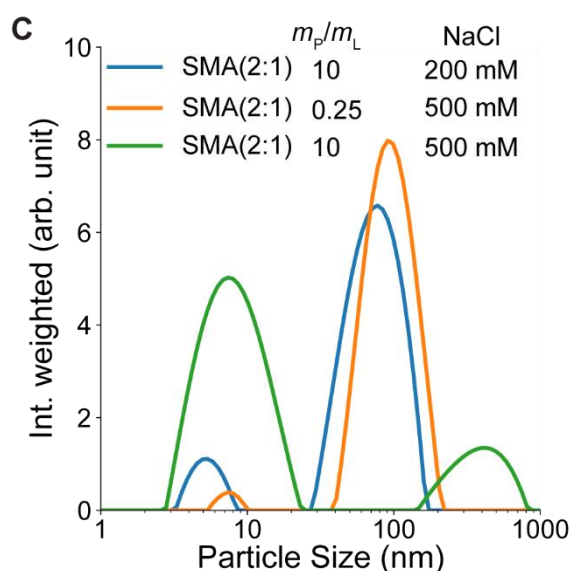
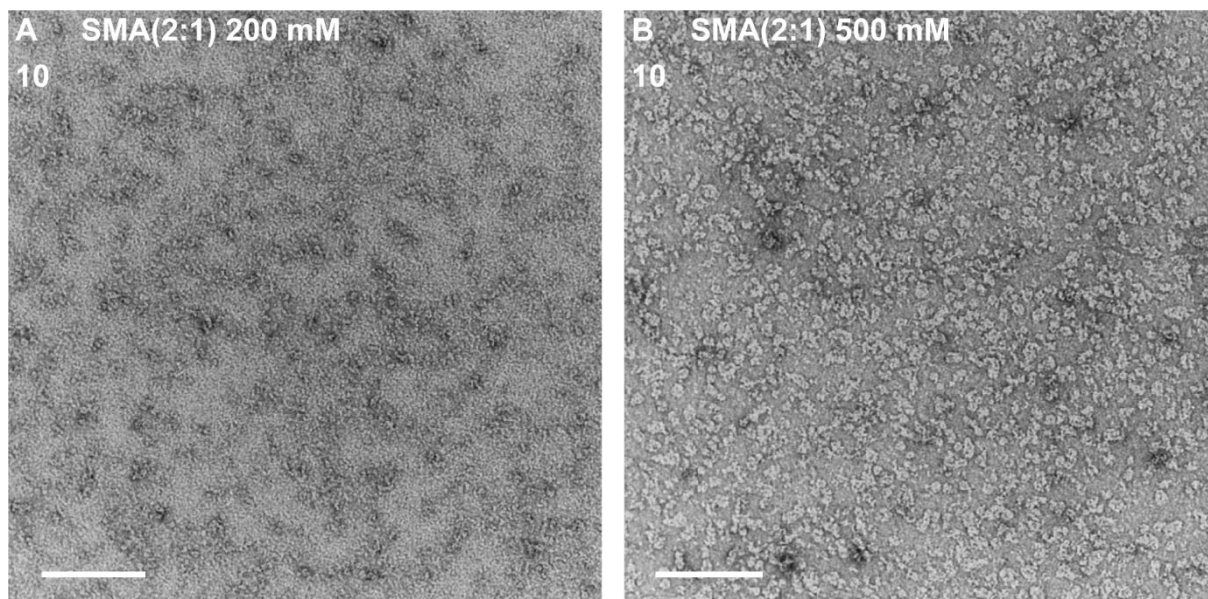


Figure 25: SMA/IMLM_{yeast}-nanodiscs at 200 mM and 500 mM NaCl. NS-EM micrographs of (A) IMLM_{yeast} ($m_P/m_L = 10$) at 200 mM NaCl, (B) IMLM_{yeast} (10) at 500 mM NaCl. Scale bars = 100 nm. (C) Intensity-weighted size distribution of SMA/IMLM_{yeast}-nanodiscs, as obtained from DLS.[†]

An inspection of Table 11 shows that DIBMA was not able to solubilize IMLM_{yeast} at any given m_P/m_L even at 500 mM NaCl. In contrast, SMA(2:1) was able to solubilize IMLM_{yeast} vesicles and form nanodiscs at 200 mM NaCl at $m_P/m_L = 10$ and at 500 mM at m_P/m_L as low as 0.25, underlining the harsher solubilization character than DIBMA. The nanodiscs, formed by SMA(2:1), had diameters ranging from $d_z = (5 \pm 3)$ nm up to $d_z = (8 \pm 3)$ nm. This highlights that the lipid composition has a great influence on the solubilization efficiency, even though they are mimicking the same organelle. Especially, lipids such as CL, can have a considerable effect on the solubilization efficiency due their effect on the lateral pressure of a membrane. A similar behavior was seen for the solubilization of vesicles that mimicked the composition of myelin sheets, which have a high cholesterol content.²⁵⁵

[†]Adapted with permission from Pu.3 (cf. chapter 10), Copyright 2023 Elsevier.

Table 11: Solubilization of artificial vesicles mimicking inner mitochondrial membrane composition of *S. cerevisiae* using polymers of various charge at different m_P/m_L . Indicated with a cross are successful nanodisc formations that were observed by NS-EM and DLS.[†]

Polymer m_P/m_L	SMA(2:1)		DIBMA	
	cNaCl			
	200	500	200	500
0.25		x		
0.5		x		
1		x		
1.5		x		
5		x		
10	x	x		

Cholesterol, similarly to cardiolipin, exerts an increase on the lateral pressure of membranes.²⁵⁶ An investigation of the lipid content of polymer/myelin-sheath-nanodiscs revealed a ~10% decrease in cholesterol content in them.²⁴¹ However, in case of the solubilization of IMLM_{yeast} the decreased content of CL and a high salt concentration (500 mM) still allowed SMA at $m_P/m_L = 0.25$ to solubilize the membranes.

4.2.1.2.4 Solubilization of thermophilic fungus lipid mixture by Sulfo-DIBMA

The solubilization of vesicles mimicking the lipid composition of a thermophilic fungus (*M. thermophila*) was performed to probe the solubilization efficiency of Sulfo-DIBMA on a membrane composition that is similar to the model organism *C. thermophilum*.²⁴⁵ Sulfo-DIBMA was chosen as the only polymer tested, as it showed the highest solubilization efficiency for IMLM_{CL} vesicles, which additionally was the closest model membrane of eukaryotic mitochondria that were tested. The formation of nanodiscs was monitored by DLS and NS-EM (Figure 26) and an overview of the solubilization results can be seen in Table 12.

[†]Adapted with permission from Pu.3 (cf. chapter 10), Copyright 2023 Elsevier.

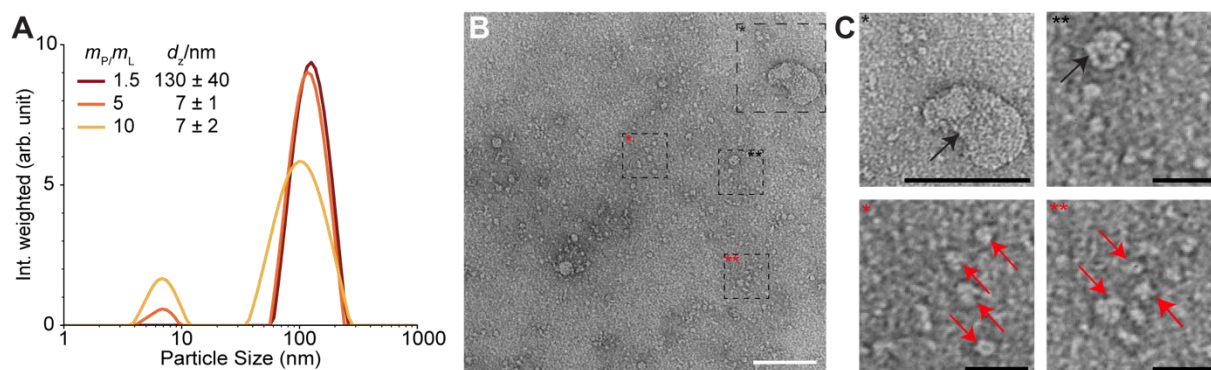


Figure 26: Architecture and morphology of Sulfo-DIBMA nanodiscs from solubilized TFLM vesicles. (A) Intensity-weighted particle size distribution of Sulfo-DIBMA nanodiscs from solubilized TFLM vesicles at different m_P/m_L . (B) Micrograph of negatively stained Sulfo-DIBMA nanodiscs with special positions encircled with a dotted line and annotated with asterisks. Scale bar = 100 nm (C) Highlighted areas from (B). Black arrows annotated left-over vesicles and membrane patches, whereas red arrows annotate the nanodiscs. Upper left image scale bar = 100 nm, other scale bars = 50 nm.[†]

Sulfo-DIBMA was able to solubilize the TFLM vesicles (cf. chapter 4.2.1.1) at high $m_P/m_L = 5$, whereas for IMLM_{CL} (cf. chapter 4.2.2.3) solubilization was observed at

Table 12: Solubilization of artificial vesicles mimicking a the thermophilic fungus lipid mixture of *M. thermophila* using Sulfo-DIBMA at different m_P/m_L . Indicated with a cross are successful nanodisc formations that were observed by NS-EM and DLS.

Polymer	Sulfo-DIBMA
m_P/m_L	
1.5	
5	x
10	x

$m_P/m_L = 1$. Further inspecting the DLS data reveals an additional peak at ~120 nm, and in general a high polydispersity of the samples, indicating that Sulfo-DIBMA was not able to fully solubilize the TFLM vesicles, however, an increase in m_P/m_L increased the signal of the 10 nm while simultaneously decreasing the peak at ~120 nm. These findings were further substantiated by NS-EM (Figure 26B, C), where nanodiscs and unsolubilized vesicles could be observed alike. The observed particles in the NS-EM resembled the structure of nanodiscs with sizes of ~7–10 nm. A possible explanation for the lower solubilization efficiency of TFLM membranes might be due to the high content of ERG (~30%). Sterols are known to increase the lateral pressure in the membrane and could even induce the formation of ordered domains, thus causing issues for the polymers to solubilize the membranes.^{27,95,100,257} This is further corroborated by a previous study, where the lipid content of liposomes and the formed nanodiscs were analyzed and compared to each other. There sterols revealed to be considerably more difficult to solubilize than other lipids, as they had a decreased content in the nanodiscs than in the liposomes.²⁴¹

[†]Adapted with permission from Pu.1 (cf. chapter 10), Copyright 2023 American Chemical Society.

4.2.2 Protein-containing polymer-bound nanodiscs

The most polymer that showed the best solubilization efficiency of the multi-component vesicles in chapter 4.2.1.2, Sulfo-DIBMA previous chapter of the solubilization of artificial multi-component lipid mixtures was used to solubilize native membranes from the thermophilic eukaryote *C. thermophilum*.

4.2.2.1 Isolation and solubilization of cellular membranes from *Chaetomium thermophilum*

The complete protocol for the growth of *C. thermophilum* and the isolation of membranes can be found in the materials and methods part of this thesis (cf. chapter 3.2.1.2, 3.2.3.3) and is depicted as a schematic in Figure 27.

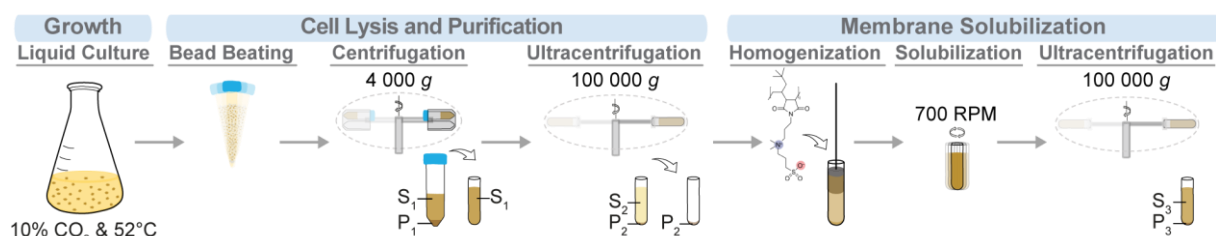


Figure 27: Schematic illustration of the experimental workflow from cell culture to nanodisc. The liquid culture is drained of media, and washed with PBS. Washed cells are lysed by mechanical bead beating. The obtained extract is centrifuged by 4000 g to separate the crude cell extract (S1) from bigger cell debris or non-lysed cells (P1). Thereafter, S1 is ultracentrifuged with 100000 g at 4°C for 80 min, separating the crude cell extract into the soluble cell extract (S2) and the membrane pellet of the cell extract (P2). S2 is discarded and the pellet P2 is being taken further for the solubilization. P2 is rehydrated with buffer and supplemented with a polymer solution in the selected concentration. Moreover, a protease inhibitors cocktail is added (c.f. chapter 3.1.2). The resulting solution is placed into a rotary shaker at 37°C at 700 rpm and incubated over-night. The incubated solution is objected to an ultracentrifugation at 100000 g at 4°C for 80 min, resulting in the nanodisc containing supernatant (S3/SN) and the unsolubilized membranes and aggregates (P3).[†]

Briefly, *C. thermophilum* was cultivated at 52°C with 10% CO₂ supply until the flask was grown at the level where the spherical shaped colonies of the organism reached 90% confluence. Subsequently, the grown hyphae of the fungus were harvested and lysed through mechanical bead beating. The lysed cells were centrifuged at 4000 g to precipitate larger debris and any non-lysed cells (P1) of the crude cell extract (S1). The remaining crude cell extract was ultracentrifuged at 100000 g for 60 min at 4°C to separate the soluble extract (S2) from the cellular membranes (P2). S2 was discarded and P2 was mixed with the polymer Sulfo-DIBMA. The addition of the polymer solution was followed by a complete homogenization of the suspension to allow for the best accessibility of the polymer towards the membranes. After the homogenization the

[†]Adapted with permission from Pu.1 (cf. chapter 10), Copyright 2023 American Chemical Society.

membrane-polymer suspension was incubated on a rotary shaker with 700 rpm at 37°C for ~16 h to allow for a complete solubilization and it was subsequently submitted to another round of ultracentrifugation at 100000 g for 80 min at 4°C. The ultracentrifugation achieved the separation of the nanodisc containing fraction (S3) from the unsolubilized material (P3). The results shown here were achieved by solubilizing 250 mg/mL *C. thermophilum* membranes with 1.25 mg/mL Sulfo-DIBMA resulting in a m_P/m_L of 0.005. This low m_P/m_L was chosen in order to improve the parameters for the subsequent vitrification.

4.2.2.2 Biochemical analysis of protein-containing polymer-bound nanodiscs

The last ultracentrifugation step in the membrane solubilization protocol yielded the crude membrane solubilized part S3 and the unsolubilized membrane patches and aggregates P3. The solubilized membrane part, S3, was injected into a HPLC column with the goal to decrease the sample complexity and enrich the nanodisc population in the eluting fractions. The complete SEC profile can be observed in Figure 28, and depicts the absorbance at the wavelength of 280 nm, A_{280} , across all the eluting fractions.

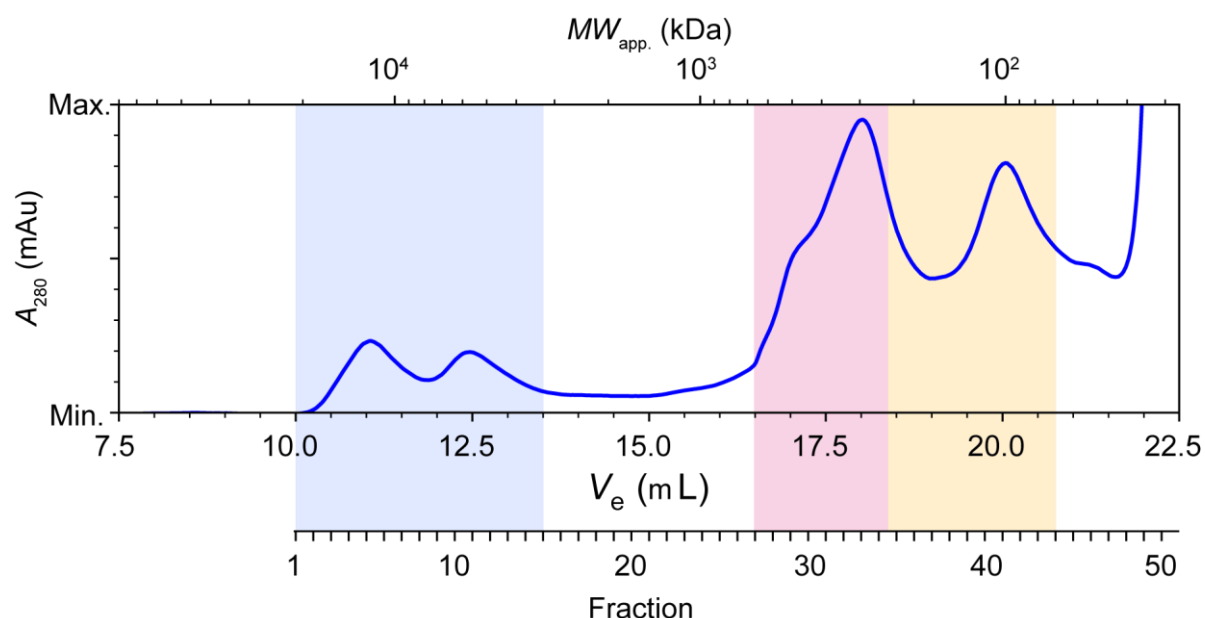


Figure 28: Size exclusion chromatography of Sulfo-DIBMA nanodiscs originating from native *C. thermophilum* membranes. 500 μ L containing 250 mg/mL *C. thermophilum* membranes and 1.25 mg/mL Sulfo-DIBMA. Absorbance at 280 nm (A_{280}) is plotted against the elution volume (V_e) and the corresponding apparent molecular weight (MW_{app}). The colored areas indicate the fractions that were used to create the pooled samples, hMW (blue, fractions 1–14), mMW (red, fractions 27–35), and IMW (yellow, fractions 36–44).[†]

[†]Adapted with permission from Pu.1 (cf. chapter 10), Copyright 2023 American Chemical Society.

The highest absorption was observed in the fractions 27–35 (850–260 kDa), resembling particles with a size of ~10 nm or higher. This particle size is slightly bigger than the nanodisc size that was previously observed by DLS, NS-EM, and cryo-EM (cf. chapter 4.2.1.2.5). However, the elution of nanodiscs in earlier fractions can be explained by the additional weight and shape of the nanodisc surrounding the extracted membrane protein.¹³¹ Thus, an elution of nanodiscs at higher molecular weight can be expected, as observed here. For further analysis, the fractions were merged into 3 separate samples, based on the A_{280} during elution because the peaks are rather broad and protein complexes are not eluting in a single fraction, but rather over multiple ones. These merged fractions are as following: high-molecular weight fractions 1–14 (hMW), medium-molecular weight fraction 27–35 (mMW), and low-molecular weight fraction 36–44 (lMW) with their expected molecular weight ranging from 20000–4000 kDa, 850–260 kDa, and 239–60 kDa, respectively. Additionally, pooling of the fractions was performed to increase the protein concentrations in order to reach a sufficient concentration for cryo-EM analysis.

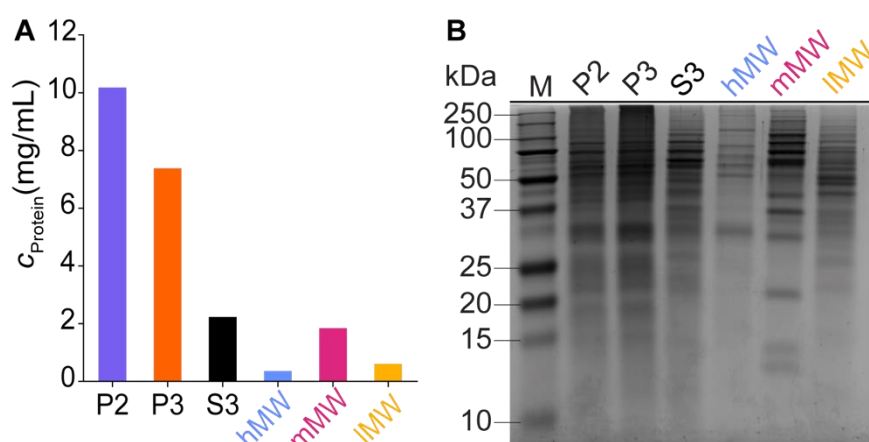


Figure 29: Bichonic acid assay and SDS-PAGE of the pooled samples hMW, mMW, and lMW and experimental intermediates P2, P3, and S3.[†]

In order to estimate the protein concentration and the variety of proteins in the pooled samples a bicinchonic acid assay (BCA) and SDS-PAGE were performed and can be seen in Figure 29A, B. First, looking upon the samples P3 and S3 in the BCA assay, a summation of their determined protein concentration gives the approximate protein concentration, determined in P2. Upon an inspection of the SDS-PAGE, clear bands of various proteins, which are also present in P2 and P3, are visible (Figure 29). All protein bands that are observed in the fractions are also visible in P3, thus no protein got completely solubilized from the pellet. This came to no surprise as the amount of polymer, was considerably lower than the concentration of the membranes, meaning that there was more material amenable for further solubilization. Taking a closer look

[†]Adapted with permission from Pu.1 (cf. chapter 10), Copyright 2023 American Chemical Society.

onto the individual samples hMW, mMW, and IMW in the BCA, the highest protein concentration in the fractions was found in the mMW with ~ 1.84 mg/mL which is followed by the IMW with ~ 0.61 mg/mL and then hMW with ~ 0.36 mg/mL. Furthermore, the later the fraction eluted the lower is the MW of the protein bands that are present in the SDS-PAGE (Figure 29B). Furthermore, in the SDS-Page the sample mMW does not just show the highest intensity but also revealed the greatest variety in bands, indicating the greatest variety in proteins among the samples. The particle size distribution of S3, and the pooled samples was measured to determine the particles sizes, which are present in the samples (Figure 30A). The greatest sample polydispersity was observed in the injected material S3, which is reflected in three defined peaks at ~ 10 nm, ~ 100 nm, and ~ 1000 nm. The observed peak at ~ 10 nm indicates the formed nanodisc in the sample whereas the peaks at ~ 100 nm suggest the presence of vesicles, even after the ultracentrifugation. A peak at ~ 1000 nm was surprising as before injection, S3 was filtered through a 220 nm PVD membrane, supposedly removing any bigger particles. A possible explanation could be that this peak could originate from the formation of bigger lipid/lipid or polymer/lipid aggregates during SEC. Upon further inspection of the DLS data, a decreasing trend in particle sizes was revealed in the fractions. The biggest particles were found in the sample hMW and the smaller ones in mMW and IMW. This result was expected and got further corroborated by the DLS results. After SEC and DLS hMW, mMW, and IMW were negatively stained and subsequently imaged by NS-EM (Figure 30B, C).

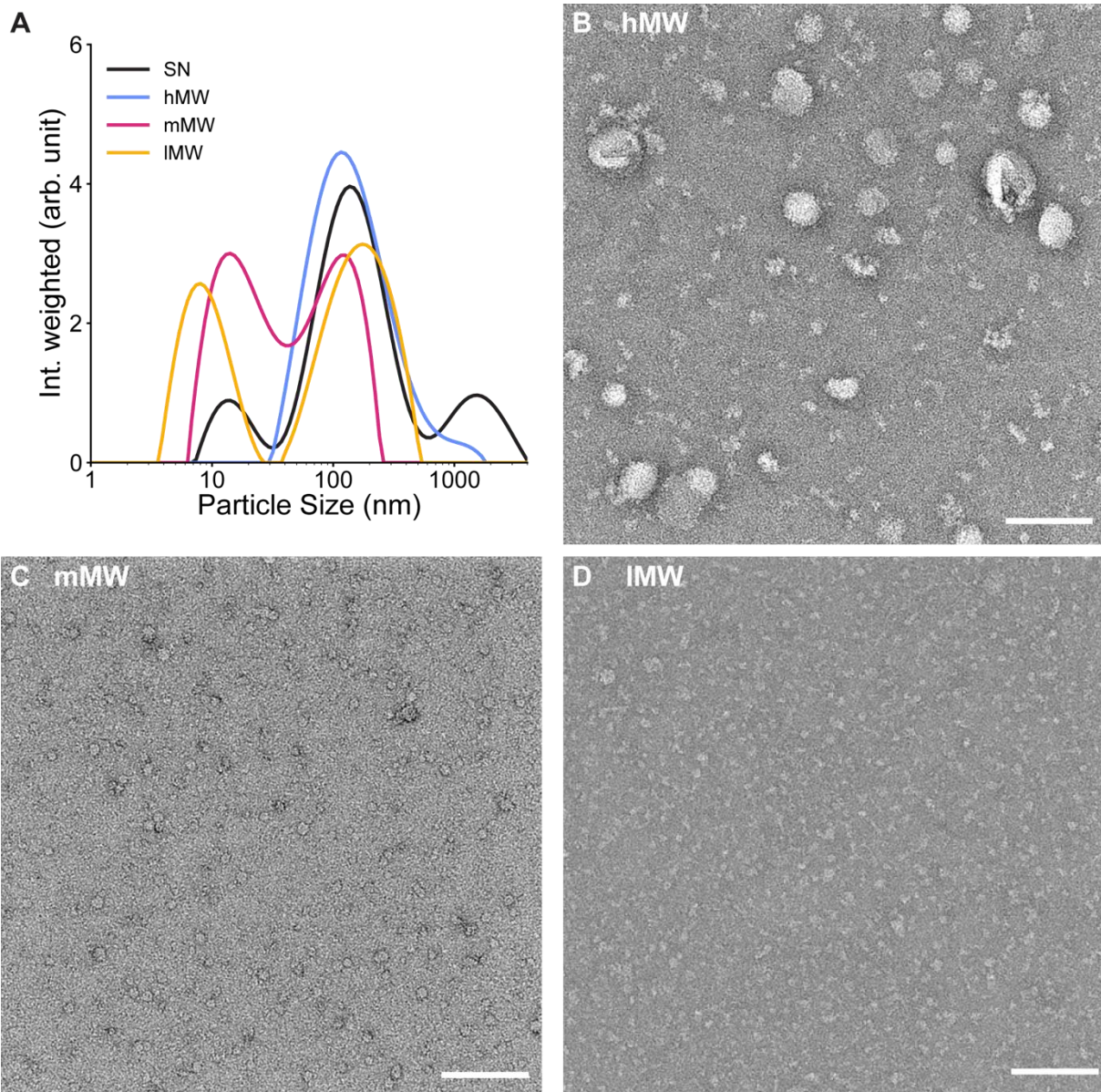


Figure 30: DLS data and NS-EM micrographs stained S3 and the fractions hMW, mMW, and IMW. (A) Intensity-weighted particle size distribution of the fractions S3, hMW, mMW, and IMW. NS-EM micrographs of (B) hMW, (C) mMW, and (D) IMW. Scale bar = 100 nm.

The presence of the peak at ~100 nm in mMW and IMW suggested the co-elution of smaller membrane patches that later reformed into bigger vesicles, however, these ~100 nm particles could not be observed by NS-EM. However, membrane patches and bigger particles were clearly visible in the hMW fraction but no particle of a size of ~1000 nm. In the micrographs of mMW, mainly smaller particles resembling nanodiscs could be observed. This highlights the effective enrichment of nanodiscs while decreasing the sample complexity by SEC (Figure 30B, C). In the IMW fraction, even smaller particles were observed. In comparison with the nanodiscs that were observed in mMW (Figure 30C) the particles in IMW seemed to be smaller and have various

structure, indicating that these particles are either polymer aggregates or small proteins that eluted.^{88,258}

As it could be shown that nanodiscs were formed and proteins were found in the samples, the sample mMW, which contained the highest protein content as well as the clearest nanodisc resembling signals in the NS-EM, was vitrified and loaded onto the electron microscope to structurally investigate the membrane proteins.

4.2.2.3 Cryo-EM and mass spectrometry of protein-containing polymer-bound nanodisc

From the vitrified mMW sample a representative micrograph can be seen in Figure 31. At a first look circular/elliptically shaped particles, with a higher inner electron density, were identified. Upon further inspection of the micrograph, it is apparent that majorly top views of the nanodiscs were captured.

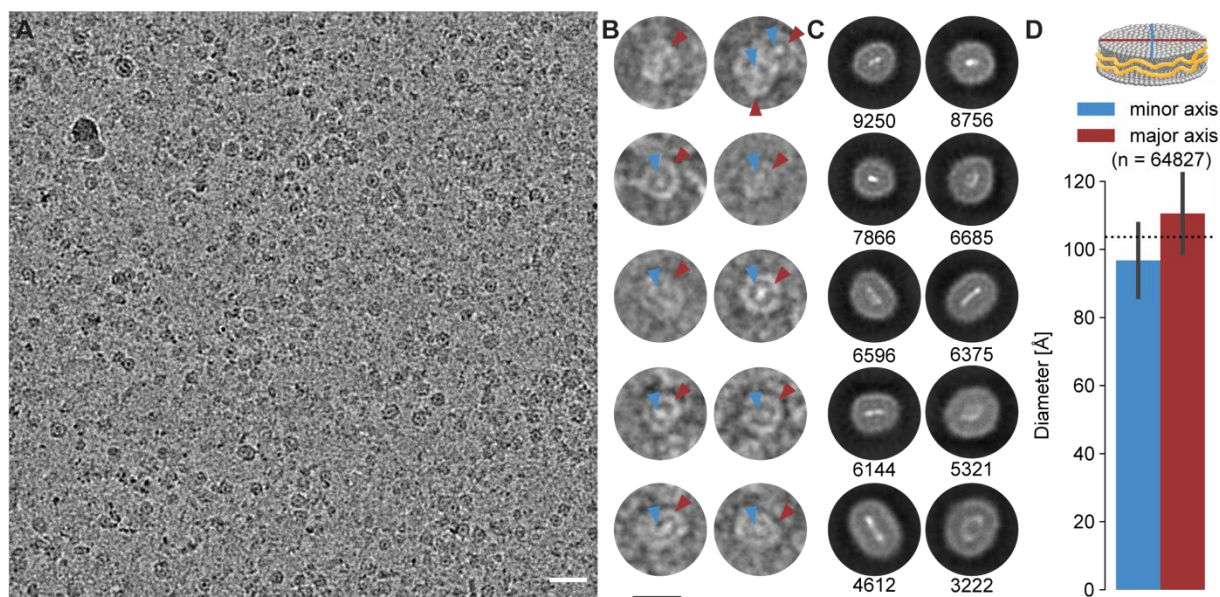


Figure 31: Architecture and morphology of native *C. thermophilum* Sulfo-DIBMA nanodiscs. (A) Representative micrograph of vitrified mMW fraction of thin ice. Scale bar = 50 nm. (B) Representative particle picks that went into the 2D classification. Blue arrows indicate the inner densities attributed to proteins embedded within the nanodiscs, whereas red arrows indicate the edges of the nanodisc. Scale bar = 10 nm and accounts for panel B and C. (C) Representative 2D classes of native *C. thermophilum* Sulfo-DIBMA nanodiscs. Denoted below is the number of particles that went into the classification of the respective class. (D) Weighted size distribution of the nanodiscs from panel C. Plotted are the lengths of the minor axis (blue) and major axis (red) that were observed in the 2D classes in panel C and indicated at the top with a schematic nanodisc.[†]

The preferred orientation of the nanodiscs can be explained by the ice thickness. The produced vitreous ice was thin, therefore the mobility of the nanodiscs inside the

[†]Adapted with permission from Pu.1 (cf. chapter 10), Copyright 2023 American Chemical Society.

amorphous ice was limited, and thus favoring the top or bottom orientation. This was most likely caused by the increased blotting time that was applied in order to obtain a stronger contrast of the nanodiscs, being very challenging particles to visualize with cryo-EM due to their size. However, this sample allowed for the investigation of the morphology of the protein-embedded nanodiscs. To this extent, 1206 movies were acquired and subsequently analyzed. From a representative dataset of 10 2D classes that together contained 64827 particles, a statistical size analysis was performed yielding the minor and major axis as well as the average nanodisc size. The observed sizes in the NS-EM were in a good agreement with the previously observed size distributions using DLS and had a similar size as the Sulfo-DIBMA/TFLM-nanodiscs originating from artificial multi-component lipid mixtures (cf. chapter 4.2.1.1, Table 8). Furthermore, the 2D classes (Figure 31C) revealed a stronger inner density that is most likely originating from the nanodisc-embedded proteins. Moreover, an inspection of the nanodiscs and their embedded inner density suggests an inherently flexible shape of the nanodiscs that could be determined by the shape of the embedded membrane protein. This indicated that the shape and size of the nanodiscs is also affected by the membrane protein, which is embedded. However, in this vitrification no clear or distinct protein densities could be observed via further classification efforts.

This could be explained by the inherent challenges of the 2D classification of heterogenous nanodisc samples, as the Sulfo-DIBMA nanodiscs have only a small variety/deviation in their overall size and morphology but contain various different proteins (Figure 31). This makes the 2D classification of nanodiscs a challenging task, This is further exemplified in comparison to the case of purified FocA, where clear and distinct structural elements were visible in the 2D classes (Figure 10, Figure 11). Furthermore, the small deviation in overall size of nanodiscs at high and low m_P/m_L highlights how Sulfo-DIBMA-nanodiscs are not altered in size due to the polymer/lipid ratio, in contrast to SMA- or DIBMA-nanodiscs where their size highly depends on the m_P/m_L . This could probably be an additional property of zwitterionic polymers and their formed nanodiscs.

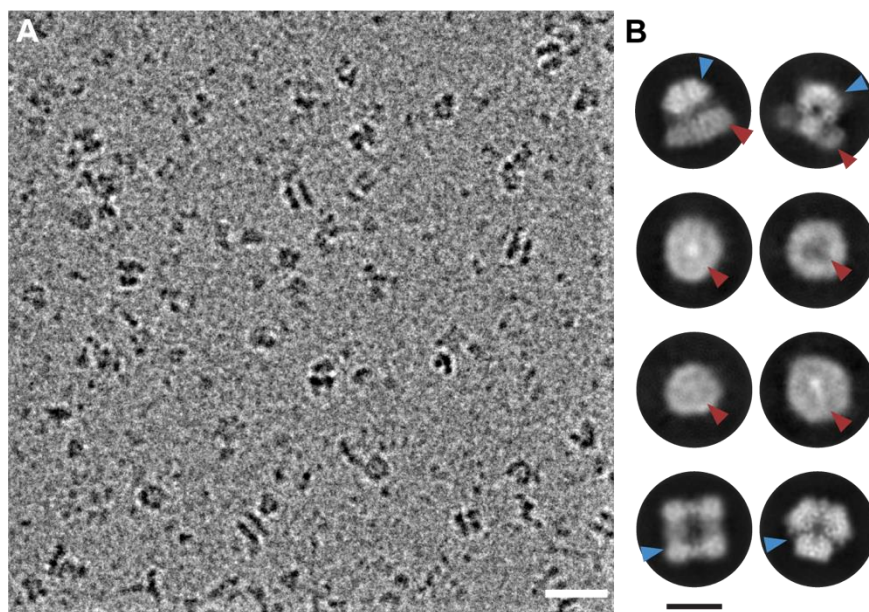


Figure 32: Representative cryo-EM micrograph and 2D classes from mMW vitrification with a decreased blotting time. (A) Cryo-EM micrograph of mMW with decreased blotting time, thus a thicker ice was achieved. Scale bar = 20 nm (B) 2D classes of potentially membrane embedded or associated proteins in the mMW sample. Blue arrows indicate the inner densities attributed to proteins embedded within the nanodiscs, whereas red arrows indicate the edges of the nanodisc. Scale bar = 10 nm.[†]

As the first vitrification attempt yielded only top and bottom views of the nanodiscs an adjustment in the blotting time was done in order to achieve a thicker ice layer and by this a greater coverage of particle orientations in the ice. Figure 32A depicts a representative micrograph of this vitrification experiment. In this micrograph a great variety of proteins and nanodiscs in different orientations are captured, compared to the previous attempt. The majority of the characterized proteins were small in size, all at ~150–250 kDa in the SDS-PAGE and ~10 nm in 2D classes, which fits to the experimentally determined size of the particles by DLS and also the size of the observed nanodiscs. In the cryo-EM data, higher-order membrane assemblies are captured, such as the square tetrameric signature (lower left 2D class) that could potentially represent a channel-like molecule or the lightbulb signature that is inserted into a bilayer density (top right 2D class) (Figure 32).

[†]Adapted with permission from Pu.1 (cf. chapter 10), Copyright 2023 American Chemical Society.

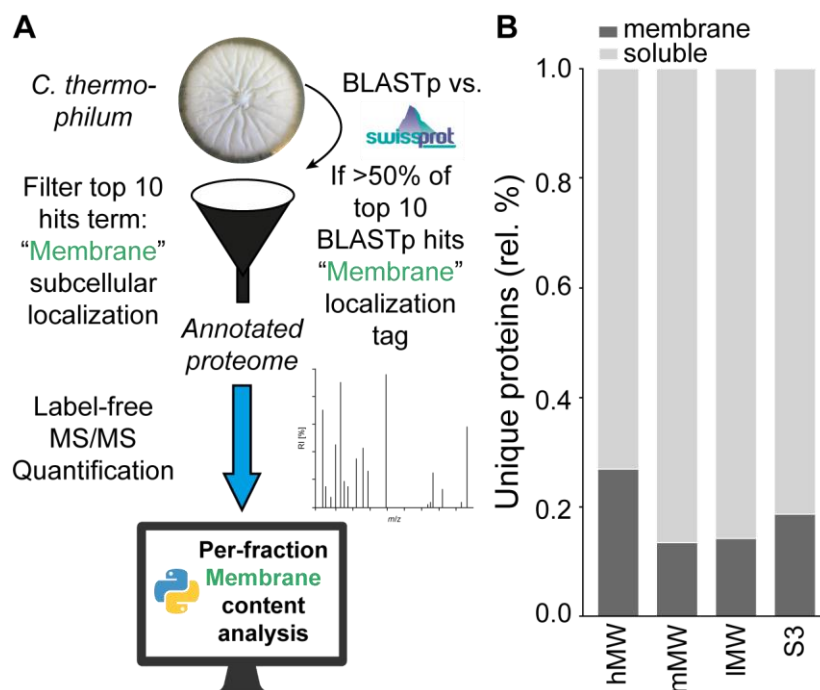


Figure 33: Computational workflow of membrane protein identification and mass spectrometry of nanodisc-embedded membrane proteins. (A) Depicts a schematic workflow that was developed and applied to the MS data to identify potential membrane proteins. (B) Depicts the relative percentage of the unique proteins that were identified in each fraction.[†]

Thereafter, to obtain an idea of proteomic content in the sample, mass spectrometry of the fractions hMW, mMW, and IMW as well as the injected material S3 were measured. The subsequent identification of the proteins, especially the identification of membrane proteins from *C. thermophilum*, posed a difficult task, as the proteome of *C. thermophilum* is limited in its annotation. To overcome this issue a homology-based algorithm, to identify membrane proteins, was developed. A schematic description of the workflow can be seen in Figure 33A and a concise description can be found in the materials and methods section. The analyzed sample content for hMW, mMW, and IMW can be found in Figure 33B. Mass spectrometry identified 204 unique membrane proteins and 912 unique soluble proteins in S3, 80 unique membrane proteins and 218 unique soluble proteins in hMW, 83 unique membrane proteins and 536 soluble proteins in mMW, and 109 unique membrane proteins and 660 unique soluble proteins in IMW. Surprisingly, the highest number of unique membrane proteins was detected in IMW, however, NS-EM revealed in this fraction mainly smaller particles that did not resemble any protein or nanodisc structure. This may suggest that membrane proteins could be fragmented and possibly co-elute with the polymer aggregates as well. This could be possible due to the long duration of the solubilization protocol combined with the dilution of the sample through SEC. Even though most of the protease inhibitors

[†]Adapted with permission from Pu.3 (cf. chapter 10), Copyright 2022 American Chemical Society.

are stable and active for a certain time, their activity-span could not be enough or their required concentration is decreased through dilution over the course of the experiment. Thus a constant protection against the degradation by all proteases through-out the complete protocol might not be guaranteed.²⁵⁹ Therefore, further adjustments, such as a decrease in solubilization time could be performed in the future to improve the quality of the samples.⁹⁴ This was already done in other research groups – membranes were successfully solubilized after 1 h, instead of solubilizing over 16 h as it was done here.²⁶⁰ However, a defined solubilization time should be tested individually for the specific membranes that are to be solubilized to achieve the best result. For example, thermophilic membranes should pose a greater difficulty to be solubilized due to their higher stability.

Additionally, the great number of soluble proteins in the fraction could be explained by the preparation method of the membranes. There, the first ultracentrifugation step separates the soluble (S1) from the membrane (P1) part in the crude cell extract. During this step the liposomes, which reformed after the cell lysis, have enveloped parts of the soluble fraction together with proteins of the soluble fraction. These proteins are then carried over, during solubilization, with the membrane fraction through-out the complete workflow and are thus co-purified. Moreover, the $m_P/m_L = 0.005$ which was used is considerably low, meaning that a surplus of membranes will be unsolubilized, thus a great fraction of membrane proteins will not come into solution.^{131,239}

4.2.2.4 Structural analysis of protein-containing polymer-bound nanodiscs

Among the identified proteins in the MS, MIPS, a transiently membrane-associated protein was found. Transiently membrane-associated proteins are not stably anchored in a membrane through transmembrane domains, or membrane anchors e.g. myristoylated termini,²⁶¹ but are transiently located at the membrane through secondary effects e.g. protein-protein or protein-lipid interactions.²⁶² MIPS is involved in the synthesis of phospholipids,²¹² and has been localized in proximity to membranes.²¹³ In this thesis, MIPS was identified in the membrane fractions of *C. thermophilum*, which were solubilized by the zwitterionic copolymer Sulfo-DIBMA. This result confirms the previous observation that polymer-treated native membranes

indeed recover possible membrane-associated proteins and complexes, such as MIPS, and allows for the structural elucidation of such without the need of overexpression. Due to MIPS symmetrical structure and relative abundance in the pooled fraction, a 4.73 Å (FSC=0.143, Figure S5) reconstruction of the complex was achieved (Figure 34).

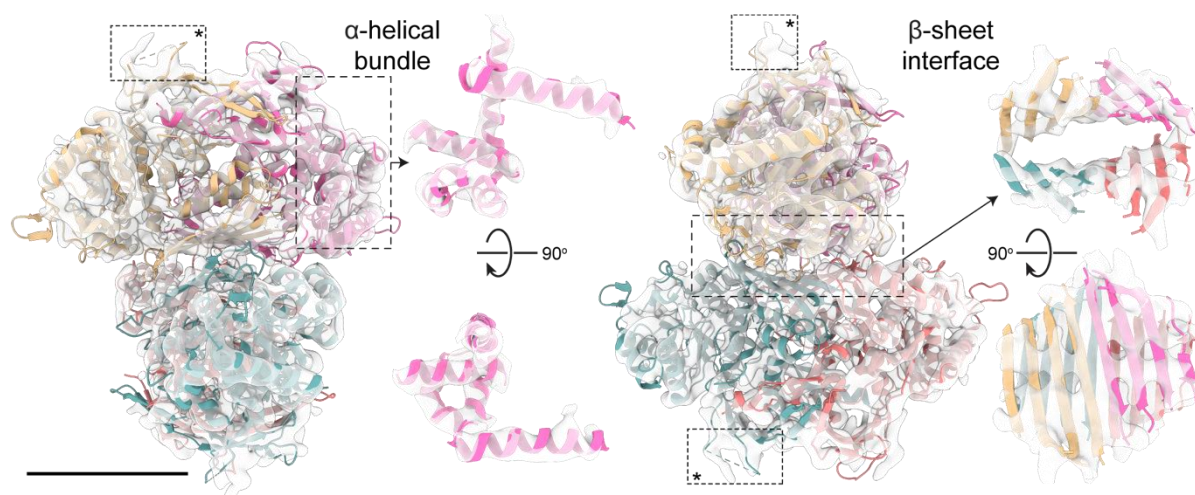


Figure 34: 3D reconstruction of MIPS with highlighted structural features. Highlighted are clearly defined alpha-helical bundles (left side) and a beta-sheet interface (right side). Indicated with a star are densities that were observed in cryo-EM but not in the X-ray structure.[†]

The cryo-EM map at this resolution, combined with the MS-data allowed for the unambiguous identification of this protein. The secondary structure is clearly discernable in the density, and the previously published X-ray structure from another species could fit, while additional densities are recovered (Figure 34, asterisk annotated field).²⁶³ Even though, the atomic model could be expanded, multiple regions remain unseen in the density map. This indicates either high flexibility or the existence of an intrinsic disordered region (IDR).²⁶⁴ These structural elements play an important role in biological processes, including but not limited to protein-protein interactions,²⁶⁵ gene regulation,²⁶⁶ and substrate shuttling.¹⁸²

Additional to the transiently membrane-associated protein complexes, an integral membrane protein, embedded in nanodiscs could be reconstructed from the cryo-EM data (Figure 35). In a recently published large-scale proteomic analysis, a library of nanodisc-embedded membrane proteins was generated.¹³¹ As expected, full membrane protein complexes in different oligomeric states, folds and sizes eluted in

[†]Adapted with permission from Pu.1 (cf. chapter 10), Copyright 2023 American Chemical Society.

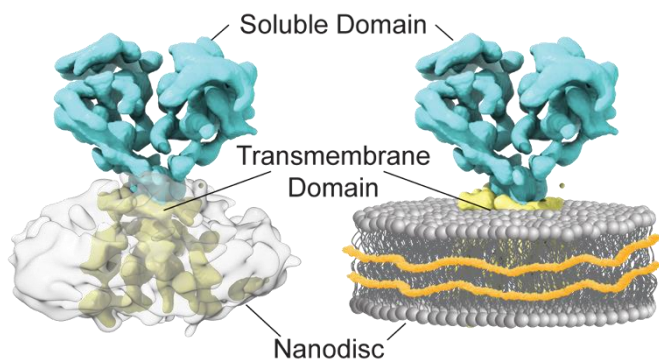


Figure 35: Reconstructed electron density map of an unidentified potential nanodisc-embedded native membrane protein with a schematic nanodisc in the same color aside. Annotated are the soluble domain(cyan), transmembrane domain (yellow), and the nanodisc (transparent/grey). Scale bar = 5 nm.[†]

well-defined peaks.¹³¹ The results reported there are corroborated by the cryo-EM data that is presented in this thesis, where potential higher-order membrane protein assemblies are captured and structurally investigated (Figure 32B, Figure 35). Furthermore, the observed shape of the nanodisc does not seem to be round but more elliptical, thus supporting the hypotheses in chapter 4.2.2.3 that the shape of the nanodiscs can be influenced by the shape of the embedded protein. A combination of the mass spectrometry results and the homology-based identification algorithm gave rise to potential hits towards the identification the extracted protein. Among them, the most promising candidate was an uncharacterized protein (UniProt-ID: G0SI00) in *C. thermophilum*, which is, based on homologous and annotated protein sequences, a putative voltage-gated potassium channel. Multiple structures of published voltage gated potassium channels were downloaded and fitted, supervised and unsupervised, into the density. The overall shape of the models fitted well to the reconstructed electron density map. However, due to the low-resolution of the reconstruction ($\sim 18 \text{ \AA}$) (FSC=0.5, Figure S6), an unambiguous identification of the nanodisc-embedded protein complex was not possible.

As a concluding remark, the MS and cryo-EM data from this specimen of native membrane complexes from a thermophilic eukaryote comprises a first and important step in the most native-like large-scale recapitulation of membrane complexes to date. Future work must include higher starting quantities of *C. thermophilum* material and polymer, to eventually resolve membrane complexes in a parallel and large-scale fashion. Another solution would be the purification of specific organelles to decrease sample complexity.²⁶⁷ If the polymer does indeed confine the recovered complexes to nanodiscs with a diameter of 10 nm, a polymer with different properties must be applied in order to study larger complexes in their native, endogenous state.

[†]Adapted with permission from Pu.1 (cf. chapter 10), Copyright 2023 American Chemical Society.

5 Conclusion and outlook

The findings of this thesis highlight how invaluable cryo-EM has become as a tool in the field of structural biology of membrane proteins, which is reflected in the rising amount of deposited protein structures by cryo-EM over the recent years.⁶⁶ Cryo-EM and the usage of DDM allowed the reconstruction and the structural analysis of the full-length version of FocA—previously studied with X-ray crystallography but with a truncated N-terminus—and the subsequent analysis of its bi-directional formate translocating channel. There, a vertical two-fold symmetry of polarity across the pore was revealed, which is centered around the important residue H209 inside this pore. A combination of previously reported *in vivo* results,²⁶⁸ paired with the structural findings in this thesis demonstrate the importance of H209 and its protonation state in the directionality of the FocA channel. In such a way, the effectiveness of cryo-EM as a tool to investigate membrane proteins is being highlighted, revealing simultaneously insights that were previously not observable through other structural analysis methods, such as the channel properties and the full-length protein FocA (cf. chapter 4.1). However, the diversity and the difficulties of such systems, e.g., the incorporation of detergent molecules in the pentameric assembly of FocA, led to approaches in which the membrane mimetic systems in use interferes less with the extracted membrane protein while maintaining an environment that is as close to the native environment as possible. In the same direction, cryo-EM with all advances that took place in this field the last decade stands as an advantageous tool that can bring the study of such mimetic systems one step further.^{66,174}

To this extent, well-established and recently developed copolymers of different charge were tested for their solubilization efficiency as an alternative to the conventional detergents.^{131,238} The copolymers were first used to solubilize lipid vesicles, which mimic the inner mitochondrial lipid mixtures from organisms such as pig heart and *S. cerevisiae*. Different compositions were tested to investigate the effect of cardiolipin, charged lipids and different salt concentrations on the solubilization efficiency of the copolymers. Although, the used vesicles mimicked the same organelle, the physical-chemical properties of the lipid mixtures were different enough to impact the solubilization efficiency of the tested polymers. The solubilization experiments on artificial multi-component lipid mixtures revealed Sulfo-DIBMA, a zwitterionic copolymer, as the copolymer with the highest solubilization efficiency on the IMLM vesicles, as it required the least amount of polymer to solubilize the high negatively

membranes. Moreover, the investigation of the zwitterionic Sulfo-DIBMA nanodiscs revealed various interactions spanning from incidental co-localizations to closer interactions, where two nanodiscs could possibly fuse, showing that nanodiscs are highly dynamic assemblies. This result corroborates the previous reported results of the rapid lipid exchange among nanodiscs.^{119,120,251}

Due to the shown effectiveness of the zwitterionic polymer Sulfo-DIBMA artificial vesicles mimicking the membrane of a thermophilic fungus as well as native membranes of *C. thermophilum* were subsequently tested for solubilization. There, Sulfo-DIBMA was able to solubilize at a surprisingly low mg/mL , 0.005. Furthermore, SEC and NS-EM experiments followed showing the possibility to effectively enrich nanodiscs in the fractions while decreasing the sample complexity. The purified samples, although still highly heterogenous, were amenable to structural elucidation of membrane proteins, which was shown through the sub 5 Å reconstruction of MIPS, a cellular protein that is transiently membrane associated.

This thesis highlights the possibility for copolymers, such as SMA, DIBMA, Glyco-DIBMA or Sulfo-DIBMA, to be a suitable membrane mimetic system that can find a widespread of application. Moreover, the effectiveness of the polymer derivatives Glyco-DIBMA and Sulfo-DIBMA revealed the importance to optimize polymers for specific targets. Finally, it was shown how the combined power of polymer nanodiscs and cryo-EM was able to structurally characterize membrane proteins in a near native state with minimal purification efforts.

Outlook

The copolymers SMA and DIBMA are not applicable to all experimental conditions and depending on the target not able to solubilize certain membranes—as shown in this thesis—or possess properties that would interfere with subsequent measurement techniques.⁹⁵ Therefore, over the last decade the scientific community strived to design novel copolymers that overcome these deficiencies and improve them even further. On this direction, examples of those copolymers such as styrene/maleic acid sulfhydryls SMA-SH, Sulfo-SMA, Sulfo-DIBMA, AASTY or zSMA were developed.^{126,131,269} As an example SMA-SH is a SMA derivative with a sulfhydryl group bound to a reactive thiol-group, making it ideal to bind to functionalized surfaces or to the addition of fluorophores.^{128,129,131} However, areas such as the purification of nanodiscs or the solubilization protocols improved over this last decade, constantly

developing e.g., the yield of membrane proteins or a specific purification approach. However, there is still room for improvements and many challenges still need to be addressed. Recently, a new proteomic profiling approach of Glueck *et al.* has been performed.¹³¹ There, a large-scale proteomic library was collected, revealing the coelution of preserved membrane protein complexes by mass spectrometry. A similar approach has also been established by the group of Jun.-Prof. Dr. Panagiotis Kastiris in the case of soluble cell extracts,¹⁸² which was introduced in 2017.²⁷⁰ There, a minimal purification approach in order to retain as much protein–protein interactions as possible revealing important co-binders of proteins is attempted. Therefore, combining the nanodisc technology with the current advancements of cryo-EM and biochemical approaches with minimal sample perturbation, enhances the possibility to identify and structurally characterize a plethora of previously uncharacterized membrane proteins. Additionally, with the currently available lipidomic techniques and an increasing availability of mass spectrometry analyses and approaches/improvements, the identification of the lipidome of many organisms is being achieved. Thus, knowing the lipidome of the target organism/organelle makes it easier to choose for the polymer or membrane mimetic system that would increase the chances to optimally solubilize the membrane protein of interest.

Overall, the future perspective for the research field of membrane proteins and the use of polymer nanodiscs is bright. This is mainly due to the interest and the progress that has been made to understand the structure and function of membrane proteins in general. Furthermore, the advances in deriving and improving specific copolymers, make them applicable to a broader range. Additionally, the deeper understanding of membrane proteins itself, gives hope to develop possible treatments for a wide range of diseases and obtain further insights on crucial biological processes previously unexplored.

6 References

- 1 Nicolson, G. L. The Fluid-Mosaic Model of Membrane Structure: still relevant to understanding the structure, function and dynamics of biological membranes after more than 40 years. *Biochim Biophys Acta* **1838**, 1451-1466 (2014). <https://doi.org/10.1016/j.bbamem.2013.10.019>
- 2 Ballweg, S. *et al.* Regulation of lipid saturation without sensing membrane fluidity. *Nat Commun* **11**, 756 (2020). <https://doi.org/10.1038/s41467-020-14528-1>
- 3 Lorent, J. H. *et al.* Plasma membranes are asymmetric in lipid unsaturation, packing and protein shape. *Nat Chem Biol* **16**, 644-652 (2020). <https://doi.org/10.1038/s41589-020-0529-6>
- 4 Cikaluk, D. E. *et al.* GERp95, a membrane-associated protein that belongs to a family of proteins involved in stem cell differentiation. *Molecular biology of the cell* **10**, 3357-3372 (1999).
- 5 Dainiak, N. & Tan, B. Utility of biological membranes as indicators for radiation exposure: alterations in membrane structure and function over time. *Stem cells (Dayton, Ohio)* **13**, 142-152 (1995).
- 6 LaNoue, K. F. & Schoolwerth, A. C. Metabolite transport in mitochondria. *Annual review of biochemistry* **48**, 871-922 (1979).
- 7 Takizawa, P. A., DeRisi, J. L., Wilhelm, J. E. & Vale, R. D. Plasma membrane compartmentalization in yeast by messenger RNA transport and a septin diffusion barrier. *Science* **290**, 341-344 (2000).
- 8 Sodt, A. J., Venable, R. M., Lyman, E. & Pastor, R. W. Nonadditive Compositional Curvature Energetics of Lipid Bilayers. *Phys Rev Lett* **117**, 138104 (2016). <https://doi.org/10.1103/PhysRevLett.117.138104>
- 9 Sezgin, E., Levental, I., Mayor, S. & Eggeling, C. The mystery of membrane organization: composition, regulation and roles of lipid rafts. *Nat Rev Mol Cell Biol* **18**, 361-374 (2017). <https://doi.org/10.1038/nrm.2017.16>
- 10 Ballweg, S. & Ernst, R. Control of membrane fluidity: the OLE pathway in focus. *Biol Chem* **398**, 215-228 (2017). <https://doi.org/10.1515/hsz-2016-0277>
- 11 Svensk, E. *et al.* Correction: Caenorhabditis elegans PAQR-2 and IGLR-2 Protect against Glucose Toxicity by Modulating Membrane Lipid Composition. *PLoS Genet* **12**, e1006112 (2016). <https://doi.org/10.1371/journal.pgen.1006112>
- 12 Ernst, R., Ballweg, S. & Levental, I. Corrigendum to "Cellular mechanisms of physicochemical membrane homeostasis" [Curr Opin Cell Biol (2018) 44-51]. *Curr Opin Cell Biol* **63**, 212 (2020). <https://doi.org/10.1016/j.ceb.2020.04.007>
- 13 Harayama, T. & Riezman, H. Author Correction: Understanding the diversity of membrane lipid composition. *Nat Rev Mol Cell Biol* **20**, 715 (2019). <https://doi.org/10.1038/s41580-019-0171-x>
- 14 Lande, M. B., Donovan, J. M. & Zeidel, M. L. The relationship between membrane fluidity and permeabilities to water, solutes, ammonia, and protons. *J Gen Physiol* **106**, 67-84 (1995). <https://doi.org/10.1085/jgp.106.1.67>
- 15 Albanesi, D., Mansilla, M. C. & de Mendoza, D. The membrane fluidity sensor DesK of Bacillus subtilis controls the signal decay of its cognate response regulator. *J Bacteriol* **186**, 2655-2663 (2004). <https://doi.org/10.1128/JB.186.9.2655-2663.2004>
- 16 Lee, S. C. *et al.* A method for detergent-free isolation of membrane proteins in their local lipid environment. *Nat Protoc* **11**, 1149-1162 (2016). <https://doi.org/10.1038/nprot.2016.070>

- 17 Cronan Jr, J. E. & Gelmann, E. P. Physical properties of membrane lipids: biological relevance and regulation. *Bacteriological reviews* **39**, 232-256 (1975).
- 18 Janmey, P. & Kinnunen, P. K. Biophysical properties of lipids and dynamic membranes. *Trends in cell biology* **16**, 538-546 (2006).
- 19 Watson, H. Biological membranes. *Essays Biochem* **59**, 43-69 (2015). <https://doi.org:10.1042/bse0590043>
- 20 Cevc, G. *Phospholipids handbook*. (CRC press, 2018).
- 21 van Meer, G., Voelker, D. R. & Feigenson, G. W. Membrane lipids: where they are and how they behave. *Nature Reviews Molecular Cell Biology* **9**, 112-124 (2008). <https://doi.org:10.1038/nrm2330>
- 22 Pelech, S. L. & Vance, D. E. Regulation of phosphatidylcholine biosynthesis. *Biochimica et Biophysica Acta (BBA)-Reviews on Biomembranes* **779**, 217-251 (1984).
- 23 Schnaar, R. L. Glycolipid-mediated cell-cell recognition in inflammation and nerve regeneration. *Arch Biochem Biophys* **426**, 163-172 (2004). <https://doi.org:10.1016/j.abb.2004.02.019>
- 24 Zhang, T., de Waard, A. A., Wuhrer, M. & Spaapen, R. M. The Role of Glycosphingolipids in Immune Cell Functions. *Front Immunol* **10**, 90 (2019). <https://doi.org:10.3389/fimmu.2019.00090>
- 25 Incardona, J. P. & Eaton, S. Cholesterol in signal transduction. *Current Opinion in Cell Biology* **12**, 193-203 (2000). [https://doi.org:https://doi.org/10.1016/S0955-0674\(99\)00076-9](https://doi.org:https://doi.org/10.1016/S0955-0674(99)00076-9)
- 26 Petersen, E. N., Chung, H. W., Nayebosadri, A. & Hansen, S. B. Kinetic disruption of lipid rafts is a mechanosensor for phospholipase D. *Nat Commun* **7**, 13873 (2016). <https://doi.org:10.1038/ncomms13873>
- 27 Demel, R. A. & De Kruyff, B. The function of sterols in membranes. *Biochim Biophys Acta* **457**, 109-132 (1976). [https://doi.org:10.1016/0304-4157\(76\)90008-3](https://doi.org:10.1016/0304-4157(76)90008-3)
- 28 Payne, A. H. & Hales, D. B. Overview of steroidogenic enzymes in the pathway from cholesterol to active steroid hormones. *Endocr Rev* **25**, 947-970 (2004). <https://doi.org:10.1210/er.2003-0030>
- 29 Hanukoglu, I. Steroidogenic enzymes: Structure, function, and role in regulation of steroid hormone biosynthesis. *The Journal of Steroid Biochemistry and Molecular Biology* **43**, 779-804 (1992). [https://doi.org:https://doi.org/10.1016/0960-0760\(92\)90307-5](https://doi.org:https://doi.org/10.1016/0960-0760(92)90307-5)
- 30 Lee, A. G. How lipids and proteins interact in a membrane: a molecular approach. *Molecular BioSystems* **1**, 203-212 (2005).
- 31 Hesketh, T. *et al.* Annular lipids determine the ATPase activity of a calcium transport protein complexed with dipalmitoyllecithin. *Biochemistry* **15**, 4145-4151 (1976).
- 32 Quinn, P. & Williams, W. The structural role of lipids in photosynthetic membranes. *Biochimica et Biophysica Acta (BBA)-Reviews on Biomembranes* **737**, 223-266 (1983).
- 33 Tanford, C. The hydrophobic effect and the organization of living matter. *Science* **200**, 1012-1018 (1978). <https://doi.org:10.1126/science.653353>
- 34 Israelachvili, J. N. *Intermolecular and surface forces*. (Academic press, 2011).
- 35 van den Brink-van der Laan, E., Killian, J. A. & de Kruijff, B. Nonbilayer lipids affect peripheral and integral membrane proteins via changes in the lateral pressure profile. *Biochim Biophys Acta* **1666**, 275-288 (2004). <https://doi.org:10.1016/j.bbamem.2004.06.010>

- 36 Strandberg, E., Tiltak, D., Ehni, S., Wadhvani, P. & Ulrich, A. S. Lipid shape is a key factor for membrane interactions of amphipathic helical peptides. *Biochim Biophys Acta* **1818**, 1764-1776 (2012).
<https://doi.org/10.1016/j.bbamem.2012.02.027>
- 37 Los, D. A. & Murata, N. Membrane fluidity and its roles in the perception of environmental signals. *Biochimica et Biophysica Acta (BBA) - Biomembranes* **1666**, 142-157 (2004).
<https://doi.org/https://doi.org/10.1016/j.bbamem.2004.08.002>
- 38 Chapman, D. Phase transitions and fluidity characteristics of lipids and cell membranes. *Quarterly reviews of biophysics* **8**, 185-235 (1975).
- 39 Kucerka, N., Nieh, M. P. & Katsaras, J. Fluid phase lipid areas and bilayer thicknesses of commonly used phosphatidylcholines as a function of temperature. *Biochim Biophys Acta* **1808**, 2761-2771 (2011).
<https://doi.org/10.1016/j.bbamem.2011.07.022>
- 40 Kucerka, N., Tristram-Nagle, S. & Nagle, J. F. Structure of fully hydrated fluid phase lipid bilayers with monounsaturated chains. *J Membr Biol* **208**, 193-202 (2005). <https://doi.org/10.1007/s00232-005-7006-8>
- 41 Lentz, B. R. Membrane "fluidity" as detected by diphenylhexatriene probes. *Chemistry and Physics of Lipids* **50**, 171-190 (1989).
- 42 Van Blitterswijk, W. J., Van der Meer, B. W. & Hilkmann, H. Quantitative contributions of cholesterol and the individual classes of phospholipids and their degree of fatty acyl (un) saturation to membrane fluidity measured by fluorescence polarization. *Biochemistry* **26**, 1746-1756 (1987).
- 43 Kates, M., Pugh, E. & Ferrante, G. in *Membrane fluidity* 379-395 (Springer, 1984).
- 44 Nagle, J. F. Theory of the main lipid bilayer phase transition. *Annual Review of Physical Chemistry* **31**, 157-196 (1980).
- 45 Murata, N. & Los, D. A. Membrane fluidity and temperature perception. *Plant Physiol* **115**, 875 (1997).
- 46 Marquardt, D., Geier, B. & Pabst, G. Asymmetric lipid membranes: towards more realistic model systems. *Membranes (Basel)* **5**, 180-196 (2015).
<https://doi.org/10.3390/membranes5020180>
- 47 Sprong, H., van der Sluijs, P. & van Meer, G. How proteins move lipids and lipids move proteins. *Nat Rev Mol Cell Biol* **2**, 504-513 (2001).
<https://doi.org/10.1038/35080071>
- 48 McMahan, H. T. & Boucrot, E. Membrane curvature at a glance. *Journal of cell science* **128**, 1065-1070 (2015).
- 49 Zimmerberg, J. & Kozlov, M. M. How proteins produce cellular membrane curvature. *Nature reviews Molecular cell biology* **7**, 9-19 (2006).
- 50 McMahan, H. T. & Gallop, J. L. Membrane curvature and mechanisms of dynamic cell membrane remodelling. *Nature* **438**, 590-596 (2005).
- 51 Cho, W. & Stahelin, R. V. Membrane-protein interactions in cell signaling and membrane trafficking. *Annu. Rev. Biophys. Biomol. Struct.* **34**, 119-151 (2005).
- 52 Tashiro, K. *et al.* Signal sequence trap: a cloning strategy for secreted proteins and type I membrane proteins. *Science* **261**, 600-603 (1993).
- 53 Nevo, Y. & Nelson, N. The NRAMP family of metal-ion transporters. *Biochimica et Biophysica Acta (BBA)-Molecular Cell Research* **1763**, 609-620 (2006).
- 54 Hettema, E. H. & Tabak, H. F. Transport of fatty acids and metabolites across the peroxisomal membrane. *Biochimica et Biophysica Acta (BBA)-Molecular and Cell Biology of Lipids* **1486**, 18-27 (2000).

- 55 Nozeret, K., Boucharlat, A., Agou, F. & Buddelmeijer, N. A sensitive fluorescence-based assay to monitor enzymatic activity of the essential integral membrane protein Apolipoprotein N-acyltransferase (Lnt). *Scientific reports* **9**, 1-10 (2019).
- 56 Almén, M. S., Nordström, K. J., Fredriksson, R. & Schiöth, H. B. Mapping the human membrane proteome: a majority of the human membrane proteins can be classified according to function and evolutionary origin. *BMC biology* **7**, 1-14 (2009).
- 57 Lodish, H., Berk, A. K. & CA, B. A. Ploegh, H., Amon, A. and Martin, KC 2016. *Molecular Cell Biology, 8th Edition, WH Freeman and Company, New York, USA*
- 58 Overington, J. P., Al-Lazikani, B. & Hopkins, A. L. How many drug targets are there? *Nature reviews Drug discovery* **5**, 993-996 (2006).
- 59 Broach, J. R. & Thorner, J. High-throughput screening for drug discovery. *Nature* **384**, 14-16 (1996). [https://doi.org:10.1038/384014a0](https://doi.org/10.1038/384014a0)
- 60 Gentile, F. *et al.* Deep docking: a deep learning platform for augmentation of structure based drug discovery. *ACS central science* **6**, 939-949 (2020).
- 61 Lounnas, V. *et al.* Current progress in structure-based rational drug design marks a new mindset in drug discovery. *Computational and structural biotechnology journal* **5**, e201302011 (2013).
- 62 Yin, H. & Flynn, A. D. Drugging Membrane Protein Interactions. *Annu Rev Biomed Eng* **18**, 51-76 (2016). [https://doi.org:10.1146/annurev-bioeng-092115-025322](https://doi.org/10.1146/annurev-bioeng-092115-025322)
- 63 Guidotti, G. Membrane proteins. *Annual review of biochemistry* **41**, 731-752 (1972).
- 64 Phillips, R., Ursell, T., Wiggins, P. & Sens, P. Emerging roles for lipids in shaping membrane-protein function. *Nature* **459**, 379-385 (2009).
- 65 Schulz, G. E. beta-Barrel membrane proteins. *Curr Opin Struct Biol* **10**, 443-447 (2000). [https://doi.org:10.1016/s0959-440x\(00\)00120-2](https://doi.org/10.1016/s0959-440x(00)00120-2)
- 66 Choy, B. C., Cater, R. J., Mancina, F. & Pryor, E. E., Jr. A 10-year meta-analysis of membrane protein structural biology: Detergents, membrane mimetics, and structure determination techniques. *Biochim Biophys Acta Biomembr* **1863**, 183533 (2021). [https://doi.org:10.1016/j.bbamem.2020.183533](https://doi.org/10.1016/j.bbamem.2020.183533)
- 67 Seddon, A. M., Curnow, P. & Booth, P. J. Membrane proteins, lipids and detergents: not just a soap opera. *Biochim Biophys Acta* **1666**, 105-117 (2004). [https://doi.org:10.1016/j.bbamem.2004.04.011](https://doi.org/10.1016/j.bbamem.2004.04.011)
- 68 Johansen, N. T., Tidemand, F. G., Pedersen, M. C. & Arleth, L. Travel light: Essential packing for membrane proteins with an active lifestyle. *Biochimie* (2022). [https://doi.org:https://doi.org/10.1016/j.biochi.2022.07.014](https://doi.org/https://doi.org/10.1016/j.biochi.2022.07.014)
- 69 Ratkeviciute, G., Cooper, B. F. & Knowles, T. J. Methods for the solubilisation of membrane proteins: the micelle-aneous world of membrane protein solubilisation. *Biochem Soc Trans* **49**, 1763-1777 (2021). [https://doi.org:10.1042/BST20210181](https://doi.org/10.1042/BST20210181)
- 70 Bogdanov, M., Mileykovskaya, E. & Dowhan, W. Lipids in the assembly of membrane proteins and organization of protein supercomplexes: implications for lipid-linked disorders. *Subcell Biochem* **49**, 197-239 (2008). [https://doi.org:10.1007/978-1-4020-8831-5_8](https://doi.org/10.1007/978-1-4020-8831-5_8)
- 71 Garavito, R. M. & Ferguson-Miller, S. Detergents as tools in membrane biochemistry. *J Biol Chem* **276**, 32403-32406 (2001). [https://doi.org:10.1074/jbc.R100031200](https://doi.org/10.1074/jbc.R100031200)

- 72 le Maire, M., Champeil, P. & Möller, J. V. Interaction of membrane proteins and lipids with solubilizing detergents. *Biochimica et Biophysica Acta (BBA)-Biomembranes* **1508**, 86-111 (2000).
- 73 Lichtenberg, D., Ahyayauch, H., Alonso, A. & Goni, F. M. Detergent solubilization of lipid bilayers: a balance of driving forces. *Trends Biochem Sci* **38**, 85-93 (2013). <https://doi.org/10.1016/j.tibs.2012.11.005>
- 74 Krueger-Koplin, R. D. *et al.* An evaluation of detergents for NMR structural studies of membrane proteins. *Journal of biomolecular NMR* **28**, 43-57 (2004).
- 75 Otzen, D. E. Protein unfolding in detergents: effect of micelle structure, ionic strength, pH, and temperature. *Biophysical journal* **83**, 2219-2230 (2002).
- 76 Chipot, C. *et al.* Perturbations of Native Membrane Protein Structure in Alkyl Phosphocholine Detergents: A Critical Assessment of NMR and Biophysical Studies. *Chem Rev* **118**, 3559-3607 (2018). <https://doi.org/10.1021/acs.chemrev.7b00570>
- 77 Durand, G., Abela, M., Ebel, C. & Breyton, C. New amphiphiles to handle membrane proteins: "Ménage à Trois" between chemistry, physical chemistry, and biochemistry. *Membrane proteins production for structural analysis*, 205-251 (2014).
- 78 Mahler, F., Meister, A., Vargas, C., Durand, G. & Keller, S. Self-Assembly of Protein-Containing Lipid-Bilayer Nanodiscs from Small-Molecule Amphiphiles. *Small* **17**, e2103603 (2021). <https://doi.org/10.1002/smll.202103603>
- 79 Fendler, J. H. Atomic and molecular clusters in membrane mimetic chemistry. *Chemical Reviews* **87**, 877-899 (1987).
- 80 Frisken, B., Asman, C. & Patty, P. Studies of vesicle extrusion. *Langmuir* **16**, 928-933 (2000).
- 81 Klingler, J., Vargas, C., Fiedler, S. & Keller, S. Preparation of ready-to-use small unilamellar phospholipid vesicles by ultrasonication with a beaker resonator. *Analytical biochemistry* **477**, 10-12 (2015).
- 82 Cross, T. A., Murray, D. T. & Watts, A. Helical membrane protein conformations and their environment. *European Biophysics Journal* **42**, 731-755 (2013).
- 83 Frick, M., Schwieger, C. & Schmidt, C. Liposomes as Carriers of Membrane-Associated Proteins and Peptides for Mass Spectrometric Analysis. *Angewandte Chemie International Edition* **60**, 11523-11530 (2021).
- 84 Glover, K. J. *et al.* Structural evaluation of phospholipid bicelles for solution-state studies of membrane-associated biomolecules. *Biophysical journal* **81**, 2163-2171 (2001).
- 85 Koppiseti, R. K., Fulcher, Y. G. & Van Doren, S. R. Fusion peptide of SARS-CoV-2 spike rearranges into a wedge inserted in bilayered micelles. *Journal of the American Chemical Society* **143**, 13205-13211 (2021).
- 86 Tribet, C., Audebert, R. & Popot, J. L. Amphipols: polymers that keep membrane proteins soluble in aqueous solutions. *Proceedings of the National Academy of Sciences of the United States of America* **93**, 15047-15050 (1996). <https://doi.org/10.1073/pnas.93.26.15047>
- 87 Popot, J. L. *et al.* Amphipols from A to Z. *Annu Rev Biophys* **40**, 379-408 (2011). <https://doi.org/10.1146/annurev-biophys-042910-155219>
- 88 FLÖTENMEYER, M., WEISS, H., TRIBET, C., POPOT, J.-L. & LEONARD, K. The use of amphipathic polymers for cryo electron microscopy of NADH:ubiquinone oxidoreductase (complex I). *Journal of Microscopy* **227**, 229-235 (2007). [https://doi.org:https://doi.org/10.1111/j.1365-2818.2007.01805.x](https://doi.org/https://doi.org/10.1111/j.1365-2818.2007.01805.x)

- 89 Bayburt, T. H., Grinkova, Y. V. & Sligar, S. G. Self-Assembly of Discoidal Phospholipid Bilayer Nanoparticles with Membrane Scaffold Proteins. *Nano Letters* **2**, 853-856 (2002). <https://doi.org/10.1021/nl025623k>
- 90 Padmanabha Das, K. M., Shih, W. M., Wagner, G. & Nasr, M. L. Large Nanodiscs: A Potential Game Changer in Structural Biology of Membrane Protein Complexes and Virus Entry. *Front Bioeng Biotechnol* **8**, 539 (2020). <https://doi.org/10.3389/fbioe.2020.00539>
- 91 Bayburt, T. H. & Sligar, S. G. Membrane protein assembly into Nanodiscs. *FEBS Lett* **584**, 1721-1727 (2010). <https://doi.org/10.1016/j.febslet.2009.10.024>
- 92 Inagaki, S., Ghirlando, R. & Grishammer, R. Biophysical characterization of membrane proteins in nanodiscs. *Methods* **59**, 287-300 (2013).
- 93 Knowles, T. J. *et al.* Membrane Proteins Solubilized Intact in Lipid Containing Nanoparticles Bounded by Styrene Maleic Acid Copolymer. *Journal of the American Chemical Society* **131**, 7484-7485 (2009). <https://doi.org/10.1021/ja810046q>
- 94 Dorr, J. M. *et al.* Detergent-free isolation, characterization, and functional reconstitution of a tetrameric K⁺ channel: the power of native nanodiscs. *Proc Natl Acad Sci U S A* **111**, 18607-18612 (2014). <https://doi.org/10.1073/pnas.1416205112>
- 95 Oluwole, A. O. *et al.* Formation of Lipid-Bilayer Nanodiscs by Diisobutylene/Maleic Acid (DIBMA) Copolymer. *Langmuir* **33**, 14378-14388 (2017). <https://doi.org/10.1021/acs.langmuir.7b03742>
- 96 Grethen, A., Oluwole, A. O., Danielczak, B., Vargas, C. & Keller, S. Thermodynamics of nanodisc formation mediated by styrene/maleic acid (2:1) copolymer. *Sci Rep* **7**, 11517 (2017). <https://doi.org/10.1038/s41598-017-11616-z>
- 97 Orwick Rydmark, M. *et al.* Styrene maleic acid copolymer induces pores in biomembranes. *Soft Matter* **15**, 7934-7944 (2019). <https://doi.org/10.1039/c9sm01407a>
- 98 Xue, M., Cheng, L., Faustino, I., Guo, W. & Marrink, S. J. Molecular Mechanism of Lipid Nanodisk Formation by Styrene-Maleic Acid Copolymers. *Biophys J* **115**, 494-502 (2018). <https://doi.org/10.1016/j.bpj.2018.06.018>
- 99 Vargas, C., Arenas, R. C., Frotscher, E. & Keller, S. Nanoparticle self-assembly in mixtures of phospholipids with styrene/maleic acid copolymers or fluorinated surfactants. *Nanoscale* **7**, 20685-20696 (2015). <https://doi.org/10.1039/c5nr06353a>
- 100 Dorr, J. M. *et al.* The styrene-maleic acid copolymer: a versatile tool in membrane research. *Eur Biophys J* **45**, 3-21 (2016). <https://doi.org/10.1007/s00249-015-1093-y>
- 101 Knowles, T. J. *et al.* Membrane proteins solubilized intact in lipid containing nanoparticles bounded by styrene maleic acid copolymer. *J Am Chem Soc* **131**, 7484-7485 (2009). <https://doi.org/10.1021/ja810046q>
- 102 Sun, C. & Gennis, R. B. Single-particle cryo-EM studies of transmembrane proteins in SMA copolymer nanodiscs. *Chem Phys Lipids* **221**, 114-119 (2019). <https://doi.org/10.1016/j.chemphyslip.2019.03.007>
- 103 Luna, V. M. *et al.* Generation of membrane proteins in polymer-based lipoparticles as flow cytometry antigens. *European Polymer Journal* **109**, 483-488 (2018). <https://doi.org/10.1016/j.eurpolymj.2018.10.017>
- 104 Gulati, S. *et al.* Detergent-free purification of ABC (ATP-binding-cassette) transporters. *Biochem J* **461**, 269-278 (2014). <https://doi.org/10.1042/BJ20131477>

- 105 Hardy, D., Bill, R. M., Rothnie, A. J. & Jawhari, A. Stabilization of Human Multidrug Resistance Protein 4 (MRP4/ABCC4) Using Novel Solubilization Agents. *SLAS Discov* **24**, 1009-1017 (2019). <https://doi.org/10.1177/2472555219867074>
- 106 Jamshad, M. *et al.* G-protein coupled receptor solubilization and purification for biophysical analysis and functional studies, in the total absence of detergent. *Biosci Rep* **35** (2015). <https://doi.org/10.1042/BSR20140171>
- 107 Swainsbury, D. J., Scheidelaar, S., van Grondelle, R., Killian, J. A. & Jones, M. R. Bacterial reaction centers purified with styrene maleic Acid copolymer retain native membrane functional properties and display enhanced stability. *Angew Chem Int Ed Engl* **53**, 11803-11807 (2014). <https://doi.org/10.1002/anie.201406412>
- 108 Reading, E. *et al.* Interrogating Membrane Protein Conformational Dynamics within Native Lipid Compositions. *Angew Chem Int Ed Engl* **56**, 15654-15657 (2017). <https://doi.org/10.1002/anie.201709657>
- 109 Barniol-Xicota, M. & Verhelst, S. H. L. Stable and Functional Rhomboid Proteases in Lipid Nanodiscs by Using Diisobutylene/Maleic Acid Copolymers. *J Am Chem Soc* **140**, 14557-14561 (2018). <https://doi.org/10.1021/jacs.8b08441>
- 110 Smirnova, I. A. *et al.* Isolation of yeast complex IV in native lipid nanodiscs. *Biochim Biophys Acta* **1858**, 2984-2992 (2016). <https://doi.org/10.1016/j.bbamem.2016.09.004>
- 111 Prabudiansyah, I., Kusters, I., Caforio, A. & Driessen, A. J. Characterization of the annular lipid shell of the Sec translocon. *Biochim Biophys Acta* **1848**, 2050-2056 (2015). <https://doi.org/10.1016/j.bbamem.2015.06.024>
- 112 Paulin, S. *et al.* Surfactant-free purification of membrane protein complexes from bacteria: application to the staphylococcal penicillin-binding protein complex PBP2/PBP2a. *Nanotechnology* **25**, 285101 (2014). <https://doi.org/10.1088/0957-4484/25/28/285101>
- 113 Smith, A. A. A. *et al.* Controlling Styrene Maleic Acid Lipid Particles through RAFT. *Biomacromolecules* **18**, 3706-3713 (2017). <https://doi.org/10.1021/acs.biomac.7b01136>
- 114 Laursen, T. *et al.* Characterization of a dynamic metabolon producing the defense compound dhurrin in sorghum. *Science* **354**, 890-893 (2016). <https://doi.org/10.1126/science.aag2347>
- 115 Lee, C. H. & MacKinnon, R. Activation mechanism of a human SK-calmodulin channel complex elucidated by cryo-EM structures. *Science* **360**, 508-513 (2018). <https://doi.org/10.1126/science.aas9466>
- 116 Pollock, N. L. *et al.* SMA-PAGE: A new method to examine complexes of membrane proteins using SMALP nano-encapsulation and native gel electrophoresis. *Biochim Biophys Acta Biomembr* **1861**, 1437-1445 (2019). <https://doi.org/10.1016/j.bbamem.2019.05.011>
- 117 Batool, M., Ahmad, B. & Choi, S. A Structure-Based Drug Discovery Paradigm. *Int J Mol Sci* **20** (2019). <https://doi.org/10.3390/ijms20112783>
- 118 Van Drie, J. H. & Tong, L. Cryo-EM as a powerful tool for drug discovery. *Bioorg Med Chem Lett* **30**, 127524 (2020). <https://doi.org/10.1016/j.bmcl.2020.127524>
- 119 Grethen, A., Glueck, D. & Keller, S. Role of Coulombic Repulsion in Collisional Lipid Transfer Among SMA(2:1)-Bounded Nanodiscs. *J Membr Biol* **251**, 443-451 (2018). <https://doi.org/10.1007/s00232-018-0024-0>

- 120 Danielczak, B. & Keller, S. Collisional lipid exchange among DIBMA-encapsulated nanodiscs (DIBMALPs). *European Polymer Journal* **109**, 206-213 (2018). <https://doi.org/10.1016/j.eurpolymj.2018.09.043>
- 121 Danielczak, B., Meister, A. & Keller, S. Influence of Mg(2+) and Ca(2+) on nanodisc formation by diisobutylene/maleic acid (DIBMA) copolymer. *Chem Phys Lipids* **221**, 30-38 (2019). <https://doi.org/10.1016/j.chemphyslip.2019.03.004>
- 122 Pollock, N. L., Lloyd, J., Montinaro, C., Rai, M. & Dafforn, T. R. Conformational trapping of an ABC transporter in polymer lipid nanoparticles. *Biochem J* **479**, 145-159 (2022). <https://doi.org/10.1042/BCJ20210312>
- 123 Scheidelaar, S. *et al.* Effect of Polymer Composition and pH on Membrane Solubilization by Styrene-Maleic Acid Copolymers. *Biophys J* **111**, 1974-1986 (2016). <https://doi.org/10.1016/j.bpj.2016.09.025>
- 124 Kostelic, M. M., Ryan, A. M., Reid, D. J., Noun, J. M. & Marty, M. T. Expanding the Types of Lipids Amenable to Native Mass Spectrometry of Lipoprotein Complexes. *J Am Soc Mass Spectrom* **30**, 1416-1425 (2019). <https://doi.org/10.1007/s13361-019-02174-x>
- 125 Tanaka, M. *et al.* Effects of charged lipids on the physicochemical and biological properties of lipid-styrene maleic acid copolymer discoidal particles. *Biochim Biophys Acta Biomembr* **1862**, 183209 (2020). <https://doi.org/10.1016/j.bbamem.2020.183209>
- 126 Fiori, M. C. *et al.* Extraction and reconstitution of membrane proteins into lipid nanodiscs encased by zwitterionic styrene-maleic amide copolymers. *Sci Rep* **10**, 9940 (2020). <https://doi.org/10.1038/s41598-020-66852-7>
- 127 Glueck, D. G., A.; Das., M.; Mmeka, O.M., Patallo, E.P.; Meister, A.; Rajender, R.; Kins, S.; Räsche, M.; Victor, J.; Etkorn, M.; Köck, Z.; Bernhard, F.; Babalola, J.O.; Vargas, C.; Keller, S. Electroneutral polymer nanodiscs enable interference-free probing of membrane proteins in a lipid-bilayer environment. *Small* (2022).
- 128 Kopf, A. H. *et al.* Synthesis and Evaluation of a Library of Alternating Amphiphatic Copolymers to Solubilize and Study Membrane Proteins. *Biomacromolecules* **23**, 743-759 (2022). <https://doi.org/10.1021/acs.biomac.1c01166>
- 129 Lindhoud, S., Carvalho, V., Pronk, J. W. & Aubin-Tam, M. E. SMA-SH: Modified Styrene-Maleic Acid Copolymer for Functionalization of Lipid Nanodiscs. *Biomacromolecules* **17**, 1516-1522 (2016). <https://doi.org/10.1021/acs.biomac.6b00140>
- 130 Hall, S. C. L. *et al.* An acid-compatible co-polymer for the solubilization of membranes and proteins into lipid bilayer-containing nanoparticles. *Nanoscale* **10**, 10609-10619 (2018). <https://doi.org/10.1039/c8nr01322e>
- 131 Glueck, D. *et al.* Electroneutral Polymer Nanodiscs Enable Interference-Free Probing of Membrane Proteins in a Lipid-Bilayer Environment. *Small*, e2202492 (2022). <https://doi.org/10.1002/sml.202202492>
- 132 Goldberg, W. I. Dynamic light scattering. *American Journal of Physics* **67**, 1152-1160 (1999).
- 133 Schätzel, K. Correlation techniques in dynamic light scattering. *Applied Physics B* **42**, 193-213 (1987).
- 134 Hassan, P. A., Rana, S. & Verma, G. Making sense of Brownian motion: colloid characterization by dynamic light scattering. *Langmuir* **31**, 3-12 (2015). <https://doi.org/10.1021/la501789z>

- 135 Bhattacharjee, S. DLS and zeta potential—what they are and what they are not? *Journal of controlled release* **235**, 337-351 (2016).
- 136 Edward, J. T. Molecular volumes and the Stokes-Einstein equation. *Journal of chemical education* **47**, 261 (1970).
- 137 Kaszuba, M., McKnight, D., Connah, M. T., McNeil-Watson, F. K. & Nobbmann, U. Measuring sub nanometre sizes using dynamic light scattering. *Journal of nanoparticle research* **10**, 823-829 (2008).
- 138 Bumiller, M. Particle sizing using ISO 13321. *American laboratory (Fairfield)* **29** (1997).
- 139 Koppel, D. E. Analysis of Macromolecular Polydispersity in Intensity Correlation Spectroscopy: The Method of Cumulants. *Journal of Chemical Physics* **57**, 4814-4820 (1972).
- 140 Provencher, S. W. CONTIN: A general purpose constrained regularization program for inverting noisy linear algebraic and integral equations. *Computer Physics Communications* **27**, 229-242 (1982).
[https://doi.org:https://doi.org/10.1016/0010-4655\(82\)90174-6](https://doi.org/https://doi.org/10.1016/0010-4655(82)90174-6)
- 141 Stetefeld, J., McKenna, S. A. & Patel, T. R. Dynamic light scattering: a practical guide and applications in biomedical sciences. *Biophysical reviews* **8**, 409-427 (2016).
- 142 Niskanen, I. *et al.* Determination of nanoparticle size using Rayleigh approximation and Mie theory. *Chemical Engineering Science* **201**, 222-229 (2019). <https://doi.org:https://doi.org/10.1016/j.ces.2019.02.020>
- 143 Dieckmann, Y., Cölfen, H., Hofmann, H. & Petri-Fink, A. Particle size distribution measurements of manganese-doped ZnS nanoparticles. *Analytical chemistry* **81**, 3889-3895 (2009).
- 144 Hayat, M. *Basic techniques for transmission electron microscopy*. (Elsevier, 2012).
- 145 De Graef, M. *Introduction to conventional transmission electron microscopy*. (Cambridge university press, 2003).
- 146 Williams, D. B. & Carter, C. B. in *Transmission electron microscopy* 3-17 (Springer, 1996).
- 147 Adrian, M., Dubochet, J., Lepault, J. & McDowell, A. W. Cryo-electron microscopy of viruses. *Nature* **308**, 32-36 (1984).
- 148 Dodonova, S. O. *et al.* 9A structure of the COPI coat reveals that the Arf1 GTPase occupies two contrasting molecular environments. *Elife* **6** (2017).
<https://doi.org:10.7554/eLife.26691>
- 149 Gan, L. & Jensen, G. J. Electron tomography of cells. *Q Rev Biophys* **45**, 27-56 (2012). <https://doi.org:10.1017/S0033583511000102>
- 150 Beck, M. *et al.* Nuclear pore complex structure and dynamics revealed by cryoelectron tomography. *Science* **306**, 1387-1390 (2004).
<https://doi.org:10.1126/science.1104808>
- 151 Ruprecht, J. J., Mielke, T., Vogel, R., Villa, C. & Schertler, G. F. Electron crystallography reveals the structure of metarhodopsin I. *EMBO J* **23**, 3609-3620 (2004). <https://doi.org:10.1038/sj.emboj.7600374>
- 152 Nannenga, B. L., Shi, D., Leslie, A. G. W. & Gonen, T. High-resolution structure determination by continuous-rotation data collection in MicroED. *Nat Methods* **11**, 927-930 (2014). <https://doi.org:10.1038/nmeth.3043>
- 153 Ruska, H., Borries, B. v. & Ruska, E. Die Bedeutung der Übermikroskopie für die Virusforschung. *Archiv für die gesamte Virusforschung* **1**, 155-169 (1939).
<https://doi.org:10.1007/BF01243399>

- 154 Porter, K. R., Claude, A. & Fullam, E. F. A Study of Tissue Culture Cells by Electron Microscopy : Methods and Preliminary Observations. *J Exp Med* **81**, 233-246 (1945). <https://doi.org:10.1084/jem.81.3.233>
- 155 Masters, B. R. History of the electron microscope in cell biology. *eLS* (2009).
- 156 Bennett, M. R. *History of the Synapse*. (CRC Press, 2001).
- 157 Amelinckx, S., Van Dyck, D., Van Landuyt, J. & van Tendeloo, G. *Electron microscopy: principles and fundamentals*. (John Wiley & Sons, 2008).
- 158 Zhu, C. *et al.* Development of analytical ultrafast transmission electron microscopy based on laser-driven Schottky field emission. *Ultramicroscopy* **209**, 112887 (2020).
- 159 Zworykin, V. K. *Electron Optics and their Electron Microscope*. (John Wiley & Sons, 1945).
- 160 Cowley, J. M. *Diffraction physics*. (Elsevier, 1995).
- 161 Brydson, R. *Aberration-corrected analytical transmission electron microscopy*. Vol. 280 (Wiley Online Library, 2011).
- 162 McMullan, G., Faruqi, A. R. & Henderson, R. Direct Electron Detectors. *Methods Enzymol* **579**, 1-17 (2016). <https://doi.org:10.1016/bs.mie.2016.05.056>
- 163 Reimer, L. *Transmission electron microscopy: physics of image formation and microanalysis*. Vol. 36 (Springer, 2013).
- 164 Nagayama, K. & Danev, R. Phase contrast electron microscopy: development of thin-film phase plates and biological applications. *Philos Trans R Soc Lond B Biol Sci* **363**, 2153-2162 (2008). <https://doi.org:10.1098/rstb.2008.2268>
- 165 Moody, M. F. *Structural biology using electrons and X-rays: an introduction for biologists*. (Academic Press, 2011).
- 166 Danev, R. & Nagayama, K. Transmission electron microscopy with Zernike phase plate. *Ultramicroscopy* **88**, 243-252 (2001).
- 167 Wade, R. A brief look at imaging and contrast transfer. *Ultramicroscopy* **46**, 145-156 (1992).
- 168 Zhu, J., Penczek, P. A., Schröder, R. & Frank, J. Three-dimensional reconstruction with contrast transfer function correction from energy-filtered cryoelectron micrographs: procedure and application to the 70S ribosome. *Journal of structural biology* **118**, 197-219 (1997).
- 169 Franken, L. E., Grünewald, K., Boekema, E. J. & Stuart, M. C. A Technical Introduction to Transmission Electron Microscopy for Soft-Matter: Imaging, Possibilities, Choices, and Technical Developments. *Small* **16**, 1906198 (2020).
- 170 Williams, R. C. & Wyckoff, R. W. Electron Shadow-Micrography of Virus Particles. *Proceedings of the society for experimental biology and medicine* **58**, 265-270 (1945).
- 171 Brenner, S. & Horne, R. A negative staining method for high resolution electron microscopy of viruses. *Biochimica et biophysica acta* **34**, 103-110 (1959).
- 172 Scott, J. E., Cummings, C., Brass, A. & Chen, Y. Secondary and tertiary structures of hyaluronan in aqueous solution, investigated by rotary shadowing-electron microscopy and computer simulation. Hyaluronan is a very efficient network-forming polymer. *Biochemical Journal* **274**, 699-705 (1991).
- 173 Hurbain, I. & Sachse, M. The future is cold: cryo-preparation methods for transmission electron microscopy of cells. *Biology of the Cell* **103**, 405-420 (2011).
- 174 Kuhlbrandt, W. Biochemistry. The resolution revolution. *Science* **343**, 1443-1444 (2014). <https://doi.org:10.1126/science.1251652>

- 175 Bai, X. C., McMullan, G. & Scheres, S. H. How cryo-EM is revolutionizing structural biology. *Trends Biochem Sci* **40**, 49-57 (2015). <https://doi.org:10.1016/j.tibs.2014.10.005>
- 176 Dubochet, J. On the Development of Electron Cryo-Microscopy (Nobel Lecture). *Angew Chem Int Ed Engl* **57**, 10842-10846 (2018). <https://doi.org:10.1002/anie.201804280>
- 177 Frank, J. Single-Particle Reconstruction of Biological Molecules-Story in a Sample (Nobel Lecture). *Angew Chem Int Ed Engl* **57**, 10826-10841 (2018). <https://doi.org:10.1002/anie.201802770>
- 178 Henderson, R. From Electron Crystallography to Single Particle CryoEM (Nobel Lecture). *Angew Chem Int Ed Engl* **57**, 10804-10825 (2018). <https://doi.org:10.1002/anie.201802731>
- 179 Kuhlbrandt, W. Cryo-EM enters a new era. *eLife* **3**, e03678 (2014). <https://doi.org:10.7554/eLife.03678>
- 180 Braunger, K. *et al.* Structural basis for coupling protein transport and N-glycosylation at the mammalian endoplasmic reticulum. *Science* **360**, 215-219 (2018). <https://doi.org:10.1126/science.aar7899>
- 181 Abbas, Y. M., Wu, D., Bueler, S. A., Robinson, C. V. & Rubinstein, J. L. Structure of V-ATPase from the mammalian brain. *Science* **367**, 1240-1246 (2020). <https://doi.org:10.1126/science.aaz2924>
- 182 Kyrilidis, F. L. *et al.* Integrative structure of a 10-megadalton eukaryotic pyruvate dehydrogenase complex from native cell extracts. *Cell Rep* **34**, 108727 (2021). <https://doi.org:10.1016/j.celrep.2021.108727>
- 183 Skalidis, I. *et al.* Cryo-EM and artificial intelligence visualize endogenous protein community members. *Structure* **30**, 575-589 e576 (2022). <https://doi.org:10.1016/j.str.2022.01.001>
- 184 Autzen, H. E. *et al.* Interactions of a Bacterial Cu(I)-ATPase with a Complex Lipid Environment. *Biochemistry* **57**, 4063-4073 (2018). <https://doi.org:10.1021/acs.biochem.8b00326>
- 185 Doyle, M. T. *et al.* Cryo-EM structures reveal multiple stages of bacterial outer membrane protein folding. *Cell* **185**, 1143-1156 e1113 (2022). <https://doi.org:10.1016/j.cell.2022.02.016>
- 186 Merk, A. *et al.* Breaking Cryo-EM Resolution Barriers to Facilitate Drug Discovery. *Cell* **165**, 1698-1707 (2016). <https://doi.org:10.1016/j.cell.2016.05.040>
- 187 Nygaard, R., Kim, J. & Mancina, F. Cryo-electron microscopy analysis of small membrane proteins. *Curr Opin Struct Biol* **64**, 26-33 (2020). <https://doi.org:10.1016/j.sbi.2020.05.009>
- 188 Lyumkis, D. Challenges and opportunities in cryo-EM single-particle analysis. *J Biol Chem* **294**, 5181-5197 (2019). <https://doi.org:10.1074/jbc.REV118.005602>
- 189 De Rosier, D. J. & Klug, A. Reconstruction of Three Dimensional Structures from Electron Micrographs. *Nature* **217**, 130-134 (1968). <https://doi.org:10.1038/217130a0>
- 190 van Heel, M. & Frank, J. Use of multivariate statistics in analysing the images of biological macromolecules. *Ultramicroscopy* **6**, 187-194 (1981). [https://doi.org:10.1016/0304-3991\(81\)90059-0](https://doi.org:10.1016/0304-3991(81)90059-0)
- 191 Sigworth, F. J. A maximum-likelihood approach to single-particle image refinement. *J Struct Biol* **122**, 328-339 (1998). <https://doi.org:10.1006/jsbi.1998.4014>
- 192 Scheres, S. H. *et al.* Maximum-likelihood multi-reference refinement for electron microscopy images. *J Mol Biol* **348**, 139-149 (2005).

- <https://doi.org/10.1016/j.jmb.2005.02.031>
- 193 Scheres, S. H. A Bayesian view on cryo-EM structure determination. *J Mol Biol* **415**, 406-418 (2012). <https://doi.org/10.1016/j.jmb.2011.11.010>
- 194 Scheres, S. H. RELION: implementation of a Bayesian approach to cryo-EM structure determination. *J Struct Biol* **180**, 519-530 (2012). <https://doi.org/10.1016/j.jsb.2012.09.006>
- 195 Lovestam, S. & Scheres, S. H. W. High-throughput cryo-EM structure determination of amyloids. *Faraday Discuss* **240**, 243-260 (2022). <https://doi.org/10.1039/d2fd00034b>
- 196 Li, X. *et al.* Electron counting and beam-induced motion correction enable near-atomic-resolution single-particle cryo-EM. *Nat Methods* **10**, 584-590 (2013). <https://doi.org/10.1038/nmeth.2472>
- 197 Zivanov, J., Nakane, T. & Scheres, S. H. W. A Bayesian approach to beam-induced motion correction in cryo-EM single-particle analysis. *IUCrJ* **6**, 5-17 (2019). <https://doi.org/10.1107/S205225251801463X>
- 198 Zhang, K. Gctf: Real-time CTF determination and correction. *J Struct Biol* **193**, 1-12 (2016). <https://doi.org/10.1016/j.jsb.2015.11.003>
- 199 Wagner, T. *et al.* SPHIRE-crYOLO is a fast and accurate fully automated particle picker for cryo-EM. *Communications Biology* **2**, 218 (2019). <https://doi.org/10.1038/s42003-019-0437-z>
- 200 Moriya, T. *et al.* Size matters: optimal mask diameter and box size for single-particle cryogenic electron microscopy. *bioRxiv* (2020).
- 201 Henderson, R. Avoiding the pitfalls of single particle cryo-electron microscopy: Einstein from noise. *Proceedings of the National Academy of Sciences* **110**, 18037-18041 (2013). <https://doi.org/doi:10.1073/pnas.1314449110>
- 202 Scheres, S. H. & Chen, S. Prevention of overfitting in cryo-EM structure determination. *Nature methods* **9**, 853-854 (2012).
- 203 Leonhartsberger, S., Korsa, I. & Bock, A. The molecular biology of formate metabolism in enterobacteria. *J Mol Microbiol Biotechnol* **4**, 269-276 (2002).
- 204 Mukherjee, M., Vajpai, M. & Sankararamakrishnan, R. Anion-selective Formate/nitrite transporters: taxonomic distribution, phylogenetic analysis and subfamily-specific conservation pattern in prokaryotes. *BMC Genomics* **18**, 560 (2017). <https://doi.org/10.1186/s12864-017-3947-4>
- 205 Waight, A. B., Love, J. & Wang, D. N. Structure and mechanism of a pentameric formate channel. *Nat Struct Mol Biol* **17**, 31-37 (2010). <https://doi.org/10.1038/nsmb.1740>
- 206 Wang, Y. *et al.* Structure of the formate transporter FocA reveals a pentameric aquaporin-like channel. *Nature* **462**, 467-472 (2009). <https://doi.org/10.1038/nature08610>
- 207 Wiechert, M. & Beitz, E. Mechanism of formate-nitrite transporters by dielectric shift of substrate acidity. *EMBO J* **36**, 949-958 (2017). <https://doi.org/10.15252/embj.201695776>
- 208 Lu, W. *et al.* pH-dependent gating in a FocA formate channel. *Science* **332**, 352-354 (2011). <https://doi.org/10.1126/science.1199098>
- 209 Kammel, M. & Sawers, R. G. The FocA channel functions to maintain intracellular formate homeostasis during *Escherichia coli* fermentation. *Microbiology (Reading)* **168** (2022). <https://doi.org/10.1099/mic.0.001168>
- 210 Majumder, A. L., Johnson, M. D. & Henry, S. A. 1L-myo-inositol-1-phosphate synthase. *Biochimica et Biophysica Acta (BBA)-Lipids and Lipid Metabolism* **1348**, 245-256 (1997).

- 211 Loewus, M., Loewus, F., Brillinger, G., Otsuka, H. & Floss, H. Stereochemistry of the myo-inositol-1-phosphate synthase reaction. *Journal of Biological Chemistry* **255**, 11710-11712 (1980).
- 212 Donahue, J. L. *et al.* The Arabidopsis thaliana Myo-inositol 1-phosphate synthase1 gene is required for Myo-inositol synthesis and suppression of cell death. *Plant Cell* **22**, 888-903 (2010). <https://doi.org/10.1105/tpc.109.071779>
- 213 Dean-Johnson, M. & Wang, X. Differentially expressed forms of 1L-myo-inositol-1-phosphate synthase in Phaseolus vulgaris. *J Biol Chem* **271**, 17215-17218 (1996).
- 214 Lackey, K. H., Pope, P. M. & Johnson, M. D. Expression of 1L-myo-inositol-1-phosphate synthase in organelles. *Plant Physiol* **132**, 2240-2247 (2003). <https://doi.org/10.1104/pp.103.020610>
- 215 Majumder, A. L., Chatterjee, A., Dastidar, K. G. & Majee, M. Diversification and evolution of L-myo-inositol 1-phosphate synthase. *Febs Letters* **553**, 3-10 (2003).
- 216 Wang, X. W. *et al.* Taxonomy, phylogeny and identification of Chaetomiaceae with emphasis on thermophilic species. *Stud Mycol* **101**, 121-243 (2022). <https://doi.org/10.3114/sim.2022.101.03>
- 217 Emsley, P. & Cowtan, K. Coot: model-building tools for molecular graphics. *Acta Crystallogr D Biol Crystallogr* **60**, 2126-2132 (2004). <https://doi.org/10.1107/s0907444904019158>
- 218 Schindelin, J. *et al.* Fiji: an open-source platform for biological-image analysis. *Nat Methods* **9**, 676-682 (2012). <https://doi.org/10.1038/nmeth.2019>
- 219 Cox, J. & Mann, M. MaxQuant enables high peptide identification rates, individualized p.p.b.-range mass accuracies and proteome-wide protein quantification. *Nat Biotechnol* **26**, 1367-1372 (2008). <https://doi.org/10.1038/nbt.1511>
- 220 Zheng, S. Q. *et al.* MotionCor2: anisotropic correction of beam-induced motion for improved cryo-electron microscopy. *Nat Methods* **14**, 331-332 (2017). <https://doi.org/10.1038/nmeth.4193>
- 221 Liebschner, D. *et al.* Macromolecular structure determination using X-rays, neutrons and electrons: recent developments in Phenix. *Acta Crystallogr D Struct Biol* **75**, 861-877 (2019). <https://doi.org/10.1107/S2059798319011471>
- 222 Guido Van Rossum, F. L. D. *Python 3 Reference Manual*. (CreateSpace, 2009).
- 223 McKinney, W. *Data Structures for Statistical Computing in Python*. 56–61 (2010).
- 224 Zivanov, J. *et al.* New tools for automated high-resolution cryo-EM structure determination in RELION-3. *Elife* **7** (2018). <https://doi.org/10.7554/eLife.42166>
- 225 Pettersen, E. F. *et al.* UCSF ChimeraX: Structure visualization for researchers, educators, and developers. *Protein Sci* **30**, 70-82 (2021). <https://doi.org/10.1002/pro.3943>
- 226 Wessel, D. & Flügge, U. A method for the quantitative recovery of protein in dilute solution in the presence of detergents and lipids. *Analytical biochemistry* **138**, 141-143 (1984).
- 227 Tihonov, A. N. Solution of incorrectly formulated problems and the regularization method. *Soviet Math.* **4**, 1035-1038 (1963).
- 228 Holzer, M., Barnert, S., Momm, J. & Schubert, R. Preparative size exclusion chromatography combined with detergent removal as a versatile tool to prepare unilamellar and spherical liposomes of highly uniform size distribution. *J Chromatogr A* **1216**, 5838-5848 (2009). <https://doi.org/10.1016/j.chroma.2009.06.023>

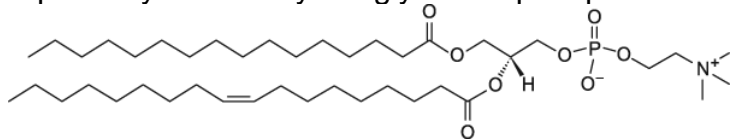
- 229 Punjani, A., Rubinstein, J. L., Fleet, D. J. & Brubaker, M. A. cryoSPARC: algorithms for rapid unsupervised cryo-EM structure determination. *Nat Methods* **14**, 290-296 (2017). <https://doi.org:10.1038/nmeth.4169>
- 230 Pravda, L. *et al.* MOLEonline: a web-based tool for analyzing channels, tunnels and pores (2018 update). *Nucleic Acids Res* **46**, W368-W373 (2018). <https://doi.org:10.1093/nar/gky309>
- 231 Pettersen, E. F. *et al.* UCSF Chimera—a visualization system for exploratory research and analysis. *Journal of computational chemistry* **25**, 1605-1612 (2004).
- 232 Adams, P. D. *et al.* PHENIX: a comprehensive Python-based system for macromolecular structure solution. *Acta Crystallographica Section D: Biological Crystallography* **66**, 213-221 (2010).
- 233 Aqvist, J., Luecke, H., Quiocho, F. A. & Warshel, A. Dipoles localized at helix termini of proteins stabilize charges. *Proc Natl Acad Sci U S A* **88**, 2026-2030 (1991). <https://doi.org:10.1073/pnas.88.5.2026>
- 234 Kammel, M., Hunger, D. & Sawers, R. G. The soluble cytoplasmic N-terminal domain of the FocA channel gates bidirectional formate translocation. *Mol Microbiol* **115**, 758-773 (2021). <https://doi.org:10.1111/mmi.14641>
- 235 Helmstetter, F., Arnold, P., Hoger, B., Petersen, L. M. & Beitz, E. Formate-nitrite transporters carrying nonprotonatable amide amino acids instead of a central histidine maintain pH-dependent transport. *J Biol Chem* **294**, 623-631 (2019). <https://doi.org:10.1074/jbc.RA118.006340>
- 236 Doberenz, C. *et al.* Pyruvate formate-lyase interacts directly with the formate channel FocA to regulate formate translocation. *J Mol Biol* **426**, 2827-2839 (2014). <https://doi.org:10.1016/j.jmb.2014.05.023>
- 237 Haneskog, L. *et al.* Monomeric human red cell glucose transporter (Glut1) in non-ionic detergent solution and a semi-elliptical torus model for detergent binding to membrane proteins. *Biochimica et Biophysica Acta (BBA)-Biomembranes* **1282**, 39-47 (1996).
- 238 Danielczak, B. *et al.* A bioinspired glycopolymer for capturing membrane proteins in native-like lipid-bilayer nanodiscs. *Nanoscale* **14**, 1855-1867 (2022). <https://doi.org:10.1039/d1nr03811g>
- 239 Kopf, A. H. *et al.* Factors influencing the solubilization of membrane proteins from Escherichia coli membranes by styrene-maleic acid copolymers. *Biochim Biophys Acta Biomembr* **1862**, 183125 (2020). <https://doi.org:10.1016/j.bbamem.2019.183125>
- 240 Scheidelaar, S. *et al.* Molecular model for the solubilization of membranes into nanodisks by styrene maleic Acid copolymers. *Biophys J* **108**, 279-290 (2015). <https://doi.org:10.1016/j.bpj.2014.11.3464>
- 241 Hoffmann, M. *et al.* Nanoscale Model System for the Human Myelin Sheath. *Biomacromolecules* **22**, 3901-3912 (2021). <https://doi.org:10.1021/acs.biomac.1c00714>
- 242 Lewis, R. N. A. H. & McElhaney, R. N. The physicochemical properties of cardiolipin bilayers and cardiolipin-containing lipid membranes. *Biochimica et Biophysica Acta (BBA) - Biomembranes* **1788**, 2069-2079 (2009). <https://doi.org:https://doi.org/10.1016/j.bbamem.2009.03.014>
- 243 Comte, J., Maïsterrena, B. & Gautheron, D. C. Lipid composition and protein profiles of outer and inner membranes from pig heart mitochondria. Comparison with microsomes. *Biochimica et Biophysica Acta (BBA) - Biomembranes* **419**, 271-284 (1976). [https://doi.org:https://doi.org/10.1016/0005-2736\(76\)90353-9](https://doi.org:https://doi.org/10.1016/0005-2736(76)90353-9)

- 244 Zinser, E. *et al.* Phospholipid synthesis and lipid composition of subcellular membranes in the unicellular eukaryote *Saccharomyces cerevisiae*. *J Bacteriol* **173**, 2026-2034 (1991). <https://doi.org/10.1128/jb.173.6.2026-2034.1991>
- 245 Ianutsevich, E. A., Danilova, O. A., Groza, N. V., Kotlova, E. R. & Tereshina, V. M. Heat shock response of thermophilic fungi: membrane lipids and soluble carbohydrates under elevated temperatures. *Microbiology (Reading)* **162**, 989-999 (2016). <https://doi.org/10.1099/mic.0.000279>
- 246 Harb, J. S., Comte, J. & Gautheron, D. C. Asymmetrical orientation of phospholipids and their interactions with marker enzymes in pig heart mitochondrial inner membrane. *Archives of Biochemistry and Biophysics* **208**, 305-318 (1981). [https://doi.org:https://doi.org/10.1016/0003-9861\(81\)90153-3](https://doi.org/https://doi.org/10.1016/0003-9861(81)90153-3)
- 247 Elmer-Dixon, M. M., Hoody, J., Steele, H. B. B., Becht, D. C. & Bowler, B. E. Cardiolipin Preferentially Partitions to the Inner Leaflet of Mixed Lipid Large Unilamellar Vesicles. *The Journal of Physical Chemistry B* **123**, 9111-9122 (2019). <https://doi.org/10.1021/acs.jpcc.9b07690>
- 248 Mahamid, J. *et al.* Liquid-crystalline phase transitions in lipid droplets are related to cellular states and specific organelle association. *Proc Natl Acad Sci U S A* **116**, 16866-16871 (2019). <https://doi.org/10.1073/pnas.1903642116>
- 249 Oluwole, A. O. *et al.* Solubilization of Membrane Proteins into Functional Lipid-Bilayer Nanodiscs Using a Diisobutylene/Maleic Acid Copolymer. *Angew Chem Int Edit* **56**, 1919-1924 (2017). <https://doi.org/10.1002/anie.201610778>
- 250 Cantor, R. S. Lipid Composition and the Lateral Pressure Profile in Bilayers. *Biophysical Journal* **76**, 2625-2639 (1999). [https://doi.org:https://doi.org/10.1016/S0006-3495\(99\)77415-1](https://doi.org:https://doi.org/10.1016/S0006-3495(99)77415-1)
- 251 Cuevas Arenas, R., Klingler, J., Vargas, C. & Keller, S. Influence of lipid bilayer properties on nanodisc formation mediated by styrene/maleic acid copolymers. *Nanoscale* **8**, 15016-15026 (2016). <https://doi.org/10.1039/C6NR02089E>
- 252 Ravula, T., Hardin, N. Z., Ramadugu, S. K., Cox, S. J. & Ramamoorthy, A. Formation of pH-Resistant Monodispersed Polymer-Lipid Nanodiscs. *Angew Chem Int Ed Engl* **57**, 1342-1345 (2018). <https://doi.org/10.1002/anie.201712017>
- 253 Postis, V. *et al.* The use of SMALPs as a novel membrane protein scaffold for structure study by negative stain electron microscopy. *Biochimica et Biophysica Acta (BBA) - Biomembranes* **1848**, 496-501 (2015). <https://doi.org:https://doi.org/10.1016/j.bbamem.2014.10.018>
- 254 Danielczak, B. & Keller, S. Lipid exchange among polymer-encapsulated nanodiscs by time-resolved Forster resonance energy transfer. *Methods* **180**, 27-34 (2020). <https://doi.org/10.1016/j.ymeth.2020.04.010>
- 255 Smith, A. A. A. *et al.* Lipid Nanodiscs via Ordered Copolymers. *Chem* **6**, 2782-2795 (2020). <https://doi.org:https://doi.org/10.1016/j.chempr.2020.08.004>
- 256 Ayee, M. A. & Levitan, I. Paradoxical impact of cholesterol on lipid packing and cell stiffness. *Front Biosci (Landmark Ed)* **21**, 1245-1259 (2016). <https://doi.org/10.2741/4454>
- 257 Veatch, S. L. & Keller, S. L. Miscibility Phase Diagrams of Giant Vesicles Containing Sphingomyelin. *Physical Review Letters* **94**, 148101 (2005). <https://doi.org/10.1103/PhysRevLett.94.148101>
- 258 Harris, J. R. *et al.* Application of the negative staining technique to both aqueous and organic solvent solutions of polymer particles. *Micron* **30**, 289-298 (1999). [https://doi.org:https://doi.org/10.1016/S0968-4328\(99\)00034-7](https://doi.org:https://doi.org/10.1016/S0968-4328(99)00034-7)

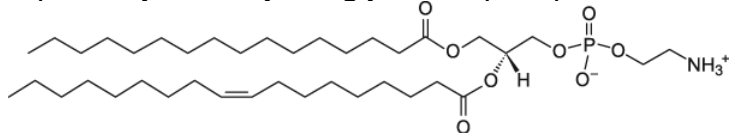
- 259 Cohen, M., Bretler, U. & Albeck, A. Peptidyl cyclopropanones: reversible inhibitors, irreversible inhibitors, or substrates of cysteine proteases? *Protein Sci* **22**, 788-799 (2013). <https://doi.org/10.1002/pro.2260>
- 260 Sun, C. *et al.* Structure of the alternative complex III in a supercomplex with cytochrome oxidase. *Nature* **557**, 123-126 (2018). <https://doi.org/10.1038/s41586-018-0061-y>
- 261 Murray, D., Ben-Tal, N., Honig, B. & McLaughlin, S. Electrostatic interaction of myristoylated proteins with membranes: simple physics, complicated biology. *Structure* **5**, 985-989 (1997).
- 262 Stelzl, U. *et al.* A human protein-protein interaction network: a resource for annotating the proteome. *Cell* **122**, 957-968 (2005).
- 263 Stein, A. J. & Geiger, J. H. The crystal structure and mechanism of 1-L-myoinositol-1-phosphate synthase. *Journal of Biological Chemistry* **277**, 9484-9491 (2002).
- 264 Nwanochie, E. & Uversky, V. N. Structure determination by single-particle cryo-electron microscopy: Only the sky (and intrinsic disorder) is the limit. *International Journal of Molecular Sciences* **20**, 4186 (2019).
- 265 Dunker, A. K., Cortese, M. S., Romero, P., Iakoucheva, L. M. & Uversky, V. N. Flexible nets: the roles of intrinsic disorder in protein interaction networks. *The FEBS journal* **272**, 5129-5148 (2005).
- 266 Kamagata, K. *et al.* Rational design using sequence information only produces a peptide that binds to the intrinsically disordered region of p53. *Scientific Reports* **9**, 8584 (2019). <https://doi.org/10.1038/s41598-019-44688-0>
- 267 Laube, E., Meier-Credo, J., Langer, J. D. & Kuhlbrandt, W. Conformational changes in mitochondrial complex I of the thermophilic eukaryote *Chaetomium thermophilum*. *Sci Adv* **8**, eadc9952 (2022). <https://doi.org/10.1126/sciadv.adc9952>
- 268 Kammel, M., Trebbin, O., Pinske, C. & Sawers, R. G. A single amino acid exchange converts FocA into a unidirectional efflux channel for formate. *Microbiology (Reading)* **168** (2022). <https://doi.org/10.1099/mic.0.001132>
- 269 Timcenko, M., Autzen, A. A. & Autzen, H. E. Characterization of divalent cation interactions with AASTY nanodiscs. *ACS Applied Polymer Materials* **4**, 1071-1083 (2022).
- 270 Kastritis, P. L. *et al.* Capturing protein communities by structural proteomics in a thermophilic eukaryote. *Mol Syst Biol* **13**, 936 (2017). <https://doi.org/10.15252/msb.20167412>

7 Appendix

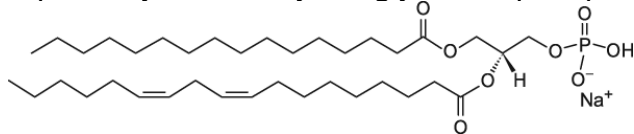
1-palmitoyl-2-linoleoyl-sn-glycero-3-phosphocholine (PC)



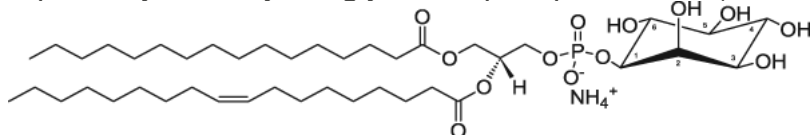
1-palmitoyl-2-oleoyl-sn-glycero-3-phosphoethanolamine (PE)



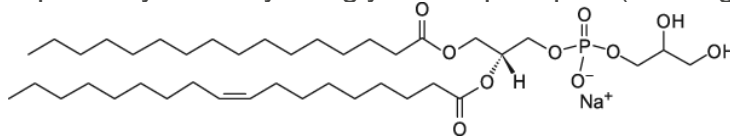
1-palmitoyl-2-linoleoyl-sn-glycero-3-phosphate (sodium salt) (PA)



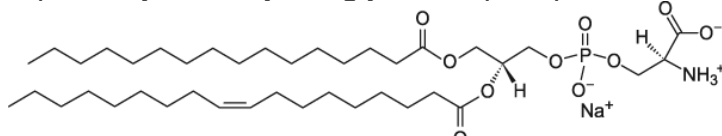
1-palmitoyl-2-oleoyl-sn-glycero-3-phosphoinositol (ammonium salt) (PI)



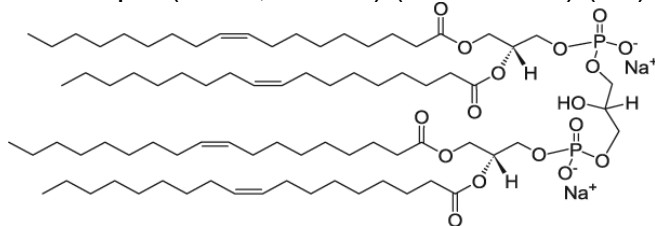
1-palmitoyl-2-oleoyl-sn-glycero-3-phospho-(1'-rac-glycerol) (sodium salt) (PG)



1-palmitoyl-2-oleoyl-sn-glycero-3-phospho-L-serine (sodium salt) (PS)



Cardiolipin (Heart, Bovine) (sodium salt) (CL)



Ergosterol (ERG)

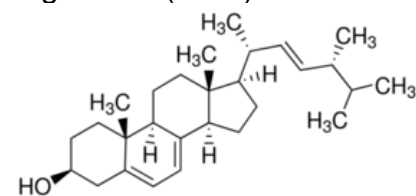
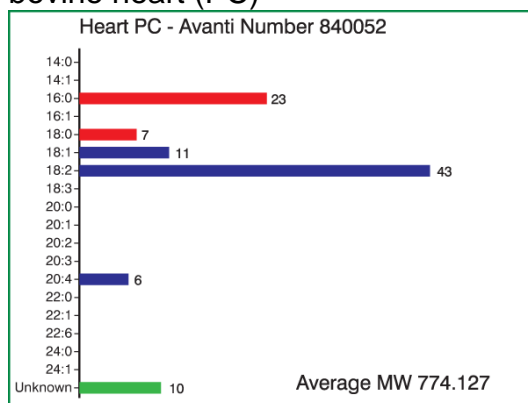
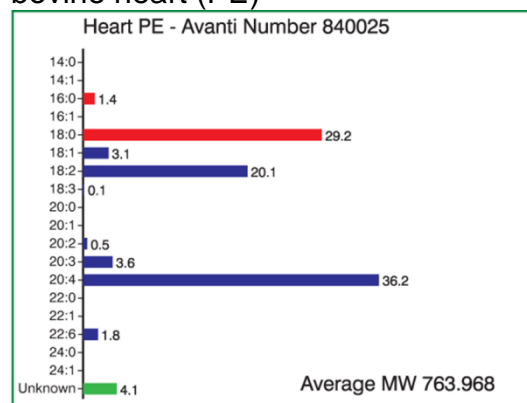


Figure S1: Chemical structure of all lipid components that were used to form the thermophilic fungus lipid mixture or the inner mitochondrial lipid mixtures.

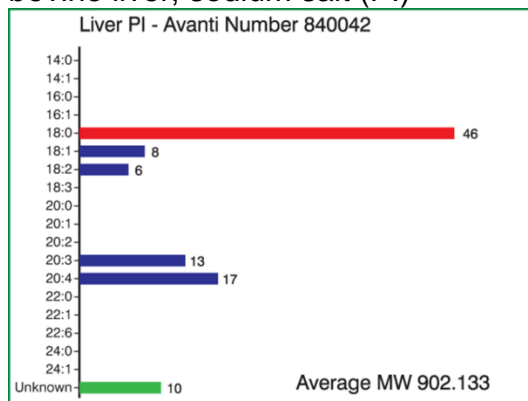
L- α -phosphatidylcholine,
bovine heart (PC)



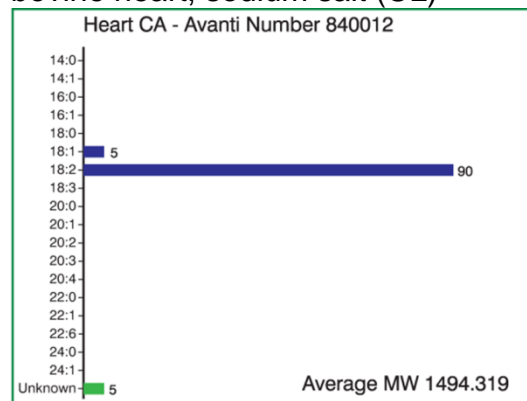
L- α -phosphatidylethanolamine,
bovine heart (PE)



L- α -phosphatidylinositol,
bovine liver, sodium salt (PI)



Cardiolipin,
bovine heart, sodium salt (CL)



L- α -phosphatidylglycerol,
soy, sodium salt (PG)

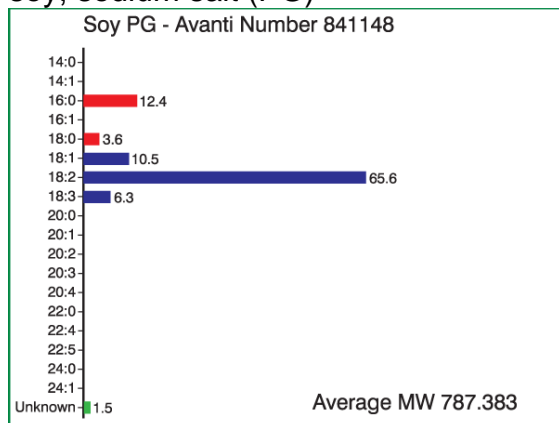


Figure S2: Fatty acid distribution of the lipid components of IMLM. Natural lipids are mixtures, and each of the structures shown is representative of one particular lipid present in the mixture.

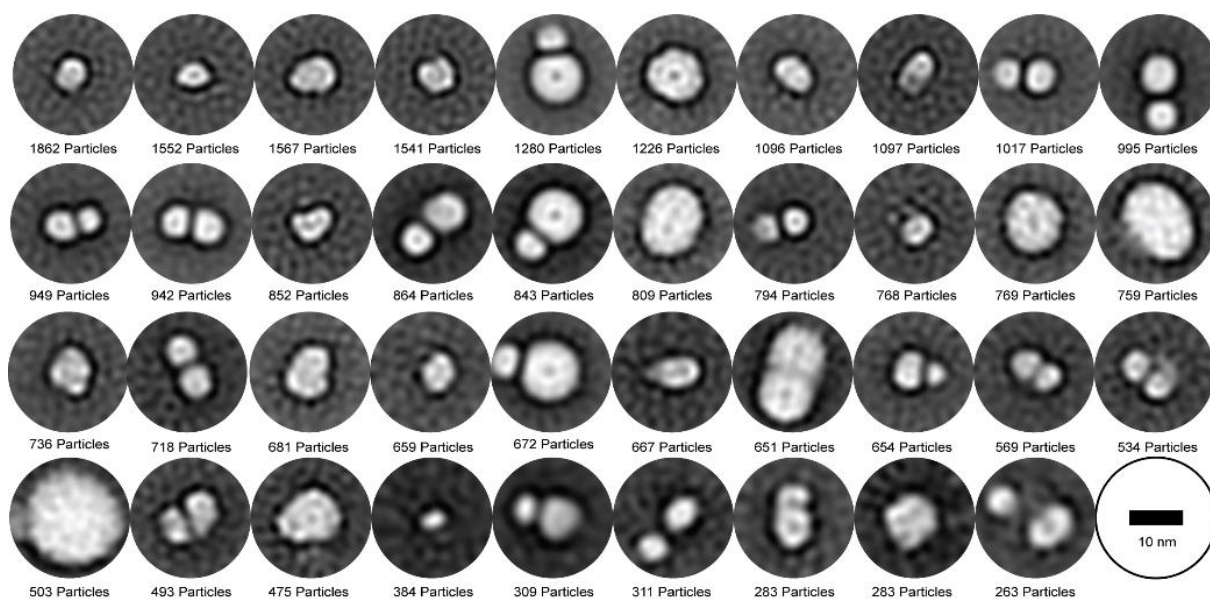


Figure S3: Analysis of EM micrographs of Sulfo-DIBMA nanodiscs from IMLM_{CL} vesicles ($m_P/m_L = 1$ at 200 mM NaCl). 39 2D class averages, with their particle numbers, that were used for further analysis. The last image shows a 10 nm scale bar.

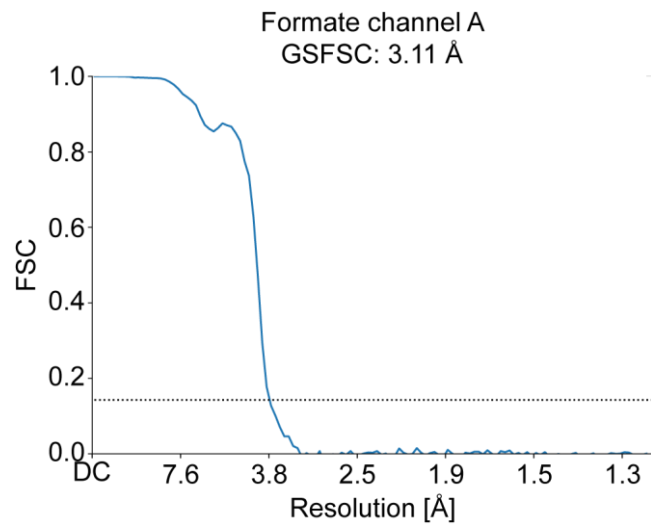


Figure S4: Fourier shell correlation ($FSC_{0.143}$) of the formate channel A in Figure 10.

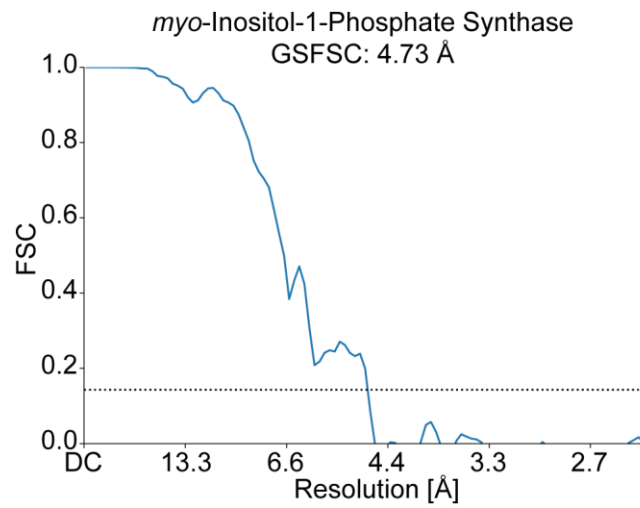


Figure S5: Fourier shell correlation ($FSC_{0.143}$) of the *myo*-inositol-1-phosphate synthase in Figure 33.

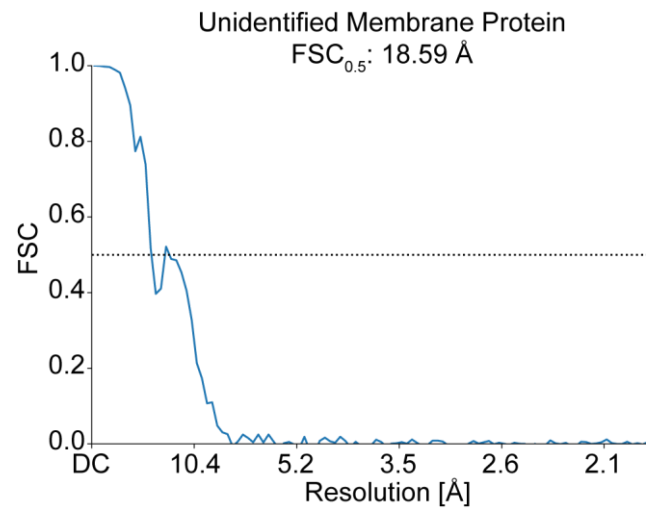


Figure S6: Fourier shell correlation ($FSC_{0.5}$) of the unidentified membrane protein in Figure 34.

Table S1: Fatty acid distribution of IMLM_{CL}. The natural inner mitochondrial fatty acid composition is given for comparison in italics.*

Lipid headgroup	PC		PE		CL		PI	
C14:0		<i>2.4</i>		<i>1.7</i>		<i>1.4</i>		<i>1.7</i>
C15:0		<i>5.6</i>		<i>1.8</i>		<i>0</i>		<i>3.2</i>
C16:0	23	<i>27.6</i>	1.4	<i>9.1</i>		<i>9</i>		<i>23.2</i>
C16:1		<i>1.6</i>		<i>3.8</i>		<i>2.4</i>		<i>2.2</i>
C17:0		<i>0.8</i>		<i>2.0</i>		<i>1.6</i>		<i>1.5</i>
C18:0	7	<i>9.4</i>	29.2	<i>19.7</i>		<i>6.3</i>	46	<i>32.3</i>
C18:1	11	<i>16.4</i>	3.1	<i>8.6</i>	5	<i>11.5</i>	8	<i>9.3</i>
C18:2	43	<i>29.0</i>	20.1	<i>22.1</i>	90	<i>65.2</i>	6	<i>13.0</i>
C18:3		<i>1.3</i>		<i>2.3</i>		<i>0</i>		<i>4.3</i>
C20:1		<i>0</i>		<i>2.1</i>		<i>0</i>		<i>2.2</i>
C20:2			0.5					
C20:3			3.6				13	
C20:4	6	<i>1.8</i>	36.2	<i>20.5</i>		<i>0</i>	17	<i>2.8</i>
C20:6			1.8					
unknown	10				5		10	

*all values are given in mol %

Table S2: List of the vitrification parameters that were used in the in the cryo-EM sample preparation.

Parameter	Formate channel A	Thin ice acquisition	Thick ice acquisition
Blotforce	0	-1	-1
Blot time (s)	6	12	9

Table S3: Acquisition and reconstruction parameters of the cryo-EM datasets. Listed are all acquisition parameters.

	Acquisition FocA Figure 12	Acquisition Thin-ice Figure 30	Acquisition MIPS Figure 33	Acquisition Nanodisc Figure 34
Data collection and processing				
Magnification	240000X	150000X	240000X	240000X
Voltage (kV)	200	200	200	200
Microscope model	TFS Glacios	TFS Glacios	TFS Glacios	TFS Glacios
Camera model	TFS Falcon III EC	TFS Falcon III EC	TFS Falcon III EC	TFS Falcon III EC
Number of frames	30	60	60	60
Electron exposure (e ⁻)	51.78	64.72	64.72	64.72
Defocus range (μm)	-0.8 to - 2.0	-0.8 to -2.0	-0.8 to -2.0	-0.8 to -2.0
Pixel size (Å)	0.59	0.96	0.59	0.59
Images acquired (no.)	3665	1206	5912	5912
Acquisition software	TFS EPU 2	TFS EPU 2	TFS EPU 2	TFS EPU 2
Symmetry imposed	C5		C1	D2
Initial particle images (no.)	1767285	1394990	1720004	1720004
Final particle images (no.)	192440	-	7253	38628
Map resolution (Å)	3.11	-	18.59	4.73
FSC threshold	0.143	-	0.5	0.143
Map B-factor	178.7	-	794.0	213.2
Fitted model (PDB code)	3KCU	-	-	1p1f
Refinement				
Initial model used (PDB code)	3KCU	-	-	-
Map sharpening B factor (Å ²)	0 (not modified)	-	-	-
Mode composition				

Non-hydrogen atoms	2178	-	-	-
Protein residues	275	-	-	-
R.m.s. deviations				
Bond lengths (Å)	0.002	-	-	-
Bond angles (°)	0.438	-	-	-
Validation				
MolProbity score	1.78	-	-	-
Clashscore	18.97	-	-	-
Poor rotamers (%)	0	-	-	-
Ramachandran plot				
Favored (%)	98.17	-	-	-
Allowed (%)	1.83	-	-	-
Outliers(%)	0	-	-	-
Mao-CC	0.83	-	-	-

8 Acknowledgment

Hereby, I would like to thank all the people who were involved in realizing this work. In particular I want to thank:

Jun.-Prof. Panagiotis Kastritis for giving me the opportunity to work in his laboratory, his guidance, outstanding supervision, fruitful discussions, his inspiring devotion to science, and being a great mentor;

PD. Dr. Annette Meister for giving me the opportunity to work on the amazing field of polymer nanodiscs, her outstanding supervision, guidance, fruitful discussions, and being a great mentor;

Prof. Dr. Arne Gericke for agreeing to act as third advisor for this thesis;

Prof. Dr. Sandro Keller for sparking my interest in biophysics, fruitful discussions, and his guidance throughout my undergraduate years and beyond;

Prof. Dr Gary Sawers and Michelle Kammel for their great collaboration with the FocA project;

Prof. Dr. Antoinette Kilian and Dr. Adrian Kopf for the supply of the polymer and their fruitful collaboration;

Prof. Dr. Carla Schmidt and Dr. Marie Alfes for her fruitful collaboration and help with the mass spectrometry measurements;

AGRIPOLY for funding parts of this thesis;

Dr. Fotis Kyrilis for his excellent comments on this thesis, vitrification training, countless hours in- and outside the laboratory, and his excellent friendship, being by now my older brother;

Dr. Florian Mahler for the excellent comments on this thesis, all the fruitful and not so fruitful discussion, and the friendship;

Dr. Christian Tüting for his help and support in coding, fruitful and not-so fruitful discussions, the beer sessions, and the friendship;

Dr. Farzad Hamdi for the introduction into handling the electron microscopy and all the day and night sessions we did;

Dr. Jaydeep Belapure for his patience for explaining me the basics of python;

Toni K. Träger a.k.a. Tonyyy for his excellent comments on this thesis, fruitful discussions, countless hours in- and outside the laboratory, and his friendship;

Ioannis Skalidis for all the helpful comments on image analysis, fruitful and not-so fruitful discussions, and in general my bench/office neighbor and friend throughout the PhD, I could not have wished for someone better;

David Glück for all the years of friendship, and fruitful discussions;

All other collaboration partners I worked with during my PhD student;

All current and former members of the Kastiris Laboratory: Dr. Dmitry Semchnok, Dr. Thommy Hofmann, Lisa Schmidt, Marija Sorokina, Noah Binay, Felix Wiebe, Johannes Müller, Wiebke Schultze, Paola Modicano;

Dominic Amos, Maximilian Vatter, Manuel Pietsch for their continuous support, be it online or in person;

My family and friends for their support.

9 Curriculum vitae

Kevin Janson

Date of Birth 26 May 1994
Nationality German
Email Kevin.Janson.94@gmx.de

Professional Experience

Since 2019 **PhD Thesis** at Institute for Biochemistry & Biotechnology, Martin-Luther-Universität Halle-Wittenberg
Topic: „Membrane-mimetic systems for the structural characterization of membrane proteins by cryo-electron microscopy”
Supervisor: PD. Dr. Annette Meister, Jun.-Prof Panagiotis Kastiris

2017 **Scientific Assistant** at Department for Medicinal Chemistry, Böhringer Ingelheim, Germany (3 Months)
Supervisor: Prof. Dr. Sandro Keller, Dr. Gisela Schnapp,

2015 **Student Supervision** of the Animal Physiology Course at TU Kaiserslautern, Germany (1 year)

Education

Since 2019 **PhD Thesis** at Martin-Luther-University Halle-Wittenberg, Germany
Topic: „Membrane-mimetic systems for the structural characterization of membrane proteins by cryo-electron microscopy”

2017–2019 **Master Thesis** at Technical University Kaiserslautern, Germany
Topic: „Interactions of Gasdermin-D with Lipid Membranes Probed by Time-Resolved Fluorescence Spectroscopy”

2014–2017 **Bachelor Thesis** at Technical University Kaiserslautern, Germany
Topic: „Unfolding of Mistic in Alkyl Maltoside Micelles Probed by Time-Resolved Fluorescence Spectroscopy”

Prizes and Awards

2021 1st Poster Prize at the EMBO workshop “Recent advances in structural biology of membrane proteins” with the poster “Cryo-EM Snapshots of Nanodisc-Embedded Native Eukaryotic Membrane Proteins”

Further Qualifications

2021–2022 PhD Student Speaker for the graduate school AGRIPOLY

- PhD student representative

2014–2018 Member of the Student Council of Lifescience at the TU Kaiserslautern

- Financial Management
- Organization and Execution of Social Activities
- Contact Person for New Students

2013/2014 Work and Travel in Australia

10 List of Publications

Pu. 1. Cryo-Electron Microscopy Snapshots of Eukaryotic Membrane Proteins in Native Lipid-Bilayer Nanodiscs.

Kevin Janson, Fotis L. Kyrilis, Christian Tüting, Marie Alfes, Manabendra Das, Toni Träger, Carla Schmidt, Farzad Hamdi, Carolyn Vargas, Sandro Keller, Annette Meister, and Panagiotis Kastritis – *Biomacromolecules* 2022, 23, 5084–5094

Pu. 2. Nanoscale Model System for the Human Myelin Sheath.

Matthias Hoffmann, David Haselberger, Tommy Hofmann, Lisa Müller, **Kevin Janson**, Annette Meister, Manabendra Das, Carolyn Vargas, Sandro Keller, Panagiotis L. Kastritis, Carla Schmidt, Dariush Hinderberger, *Biomacromolecules* 2021 22(9), 3901-3912

Pu. 3. Solubilization of Artificial Mitochondrial Membranes by Amphiphilic Copolymers of Different Charges.

Kevin Janson, Jennifer Zierath, Fotis L. Kyrilis, Dmitry A. Semchonok, Farzad Hamdi, Ioannis Skalidis, Adrian H. Kopf, Manabendra Das, Cenek Kolar, Marie Rasche, Carolyn Vargas, Sandro Keller, Panagiotis L. Kastritis, Annette Meister, *Biochimica et Biophysica Acta (BBA) – Biomembranes* 2021, Volume 1863, Issue 12, 183725

The majority of the data that is shown in this thesis is published in Pu. 1 and Pu. 3 and represent the main work that was done during the doctorate.

11 Oral presentations

1. K. Janson, A. Meister, P.L. Kastritis „Cryo-Electron Microscopy Snapshots of Eukaryotic Membrane Proteins in Native Lipid-Bilayer Nanodiscs”, 2023, In situ structural biology: from cryo-EM to multi-scale modelling, EMBL Heidelberg, Germany
2. K. Janson, A. Meister, P.L. Kastritis „Cryo-Electron Microscopy of Enzymatic Pathways in Polymer-Stabilised Lipid Bilayer Nanodiscs”, 2022, AGRIPOLY Joint Meeting, Wittenberg, Germany
3. K. Janson, A. Meister, P.L. Kastritis „Cryo-Electron Microscopy Snapshots of Eukaryotic Membrane Proteins in Native Lipid-Bilayer Nanodiscs”, 2021, HALOmem Meeting, Wittenberg, Germany
4. K. Janson, A. Meister, P.L. Kastritis „Cryo-Electron Microscopy of Enzymatic Pathways in Polymer-Stabilised Lipid Bilayer Nanodiscs”, 2020, HALOmem Supergroup Meeting, Halle, Germany

K. Janson, A. Meister, P.L. Kastritis

12 Poster presentations

1. 2nd HALOmem International Meeting, Halle, Germany, 2022, „Cryo-EM Snapshots of Eukaryotic Membrane Proteins in Native Lipid-Bilayer Nanodiscs”
2. Instruct Biennial Structural Biology Conference Changes in structural biology: Challenges in Studying Dynamics, Utrecht, Netherlands, 2022, „Cryo-EM Snapshots of Eukaryotic Membrane Proteins in Native Lipid-Bilayer Nanodiscs”
3. EMBO workshop „Recent Advances in Structural Biology of Membrane Proteins”, Online, Germany, 2021, „Cryo-EM Snapshots of Nanodisc-Embedded Native Eukaryotic Membrane Proteins”

13 Affidavit

I hereby declare that this thesis has been written independently and with no other sources and aids than quoted. Parts directly or indirectly obtained from foreign sources are indicated. In addition, material provided, or experiments performed by other persons are indicated. The submitted written version of the thesis corresponds to that on the electronic storage medium. Furthermore, I assure that this doctoral thesis has not been submitted as a thesis elsewhere. I have not submitted any other doctoral thesis before this thesis.

Halle (Saale), 14.02.2023

Kevin Janson

14 Eidesstattliche Erklärung

Hiermit versichere ich, dass ich die vorliegende Arbeit selbstständig und ohne fremde Hilfe angefertigt und keine anderen als die angegebenen Quellen und Hilfsmittel verwendet habe. Die aus fremden Quellen direkt oder indirekt übernommenen Stellen sind als solche kenntlich gemacht. Ebenfalls sind alle von anderen Personen bereitgestellten Materialien oder erbrachten Experimente als solche gekennzeichnet. Die eingereichte schriftliche Fassung der Arbeit entspricht der auf dem elektronischen Speichermedium. Weiterhin versichere ich, dass die vorliegende Promotionsarbeit noch nicht als Abschlussarbeit an anderer Stelle eingereicht wurde. Ich habe vor dieser Arbeit keine andere Promotionsarbeit eingereicht.

Halle (Saale), den 14.02.2023

Kevin Janson